A Textural Image Analysis Study of Mars-Analog Sediment: Comparisons of 2D and 3D Textural Analysis Methods, Image Resolution, and the Effects of Shadows

A Thesis Presented for the
Master of Science
Degree
The University of Tennessee, Knoxville

Mary Agnes Eibl
August 2016

ACKNOWLEDGEMENTS

This work was made possible by funding from the National Aeronautics and Space Administration (grant MFRP12-0049 awarded to Chris Fedo) and my advisor, Dr. Chris Fedo, who I sincerely thank for the encouragement, inspiration, and guidance he provided throughout the completion of this thesis. I would also like to thank my committee members, Dr. Harry McSween and Dr. Linda Kah, who offered valuable feedback in their review of this work. I greatly appreciate the faculty in the Department of Earth and Planetary Sciences for their insightful comments regarding this research. Access to field locations was made possible by the Bureau of Land Management and Mr. Kirk Jungers of First Line Seeds. I would like to express gratitude to my lab group for their help with editing and field work. A great thank you to my friends, my boyfriend, and my family who have always encouraged my ambition and supported me every step of the way.

ABSTRACT

Sediments from Mars-analog, basaltic, aeolian (Moses Lake dunes, WA) and fluvial (Death Valley region, CA) environments were analyzed for textural properties (grain size, roundness, sphericity) to understand how well image-based analyses compare with actual sediment characteristics. Three interrelated studies determined: (1) how well high-resolution, two-dimensional (2D) image analysis compares with three-dimensional (3D) sediment textures, (2) the extent to which decreasing image resolution affects textural analyses by comparison with high-resolution images, and (3) the extent to which shadows at different incident solar angles has on textural measurements. In both aeolian and fluvial environments, 2D grain-size distributions and statistics closely match 3D properties of sediment. A comparison of grain-size distributions determined from images with different resolutions shows, for both sediments, grain-size means, modes, and sorting can be accurately determined at all resolutions and distribution frequencies and skewness can be estimated to 40 μm/pixel for the aeolian sediment and 80 μm/pixel for the fluvial sediment. A comparison of 2D and 3D sphericity (fluvial sediment only) shows 2D image analysis overestimates 3D sphericity. Sphericity measured in 2D, however, is not affected by image resolutions to 50 μm/pixel for the aeolian sediment and 100 μm/pixel for the fluvial sediment. Roundness estimates made in 2D and 3D are compared and show broad similarities for both sediments. At different image resolutions, roundness estimates show the average, mode, and standard deviation can be determined at all resolutions. Although, resolutions higher than 20 μm/pixel for the aeolian sediment and 40 μm/pixel, for the fluvial sediment yield most accurate results. Textural analysis of

images taken at different times of day (aeolian sediment only) show shadow length has a negligible effect on the textural parameters measured in this study. The results determine the smallest grain size at any image resolution that can be studied, as well as the required the number of grains to define a population for sediment possessing the studied sorting characteristics.

TABLE OF CONTENTS

LIST OF TABLES

LIST OF FIGURES

LIST OF ATTACHMENTS

1. INTRODUCTION

Sedimentary textures, such as grain size, sphericity, and roundness, represent valuable tools for interpreting sediment history, from grain formation in the source to mechanisms of transport and deposition. First-cycle siliciclastic sediment deposited near the source are commonly immature and composed of angular rock and mineral fragments that are poorly sorted and diverse in shape. After extensive transport, textural maturity increases as sediments become rounded, sorted, and spherical (Cornwall et al., 2015; Kleinhans, 2005; McBride and Picard; 1987; Kuenen, 1960). For this reason, textures provide an opportunity to interpret the sedimentary record and shed light on the processes that have modified sediment over time.

In the early to mid-1900s many authors contributed to the development of textural analysis methods, which have since been refined into a set of standardized techniques (Powers, 1953; Krumbein, 1941; Riley, 1941, Krumbein, 1938; Wentworth, 1922). Methods of textural analysis exist for both unconsolidated sediment exhibiting three-dimensions (3D) and lithified sediment observable only in two-dimensional (2D) rock surfaces and thin sections. These methods are typically used on physical rock and sediment samples, but imaging of sediment by high-resolution cameras offers an alternative approach to traditional sampling and laboratory analyses. Two-dimensional methods can be used on sediment images to provide textural information in lieu of physical samples. Such an approach is particularly valuable in the study of sediment on other planets, like Mars, where direct sampling is either not possible or only poorly available.

Although martian sediment has not yet been returned to Earth for detailed study, its textures have been analyzed via images taken by rover cameras (Cabrol et al., 2013; Yingst et al., 2013; McGlynn et al., 2011). The Mars Exploration Rovers (MER) and Mars Science Laboratory (MSL) rover, Curiosity, are equipped with maneuverable cameras located on rover arms and stereoscopic cameras positioned at eye-level on rover masts (Edgett et al., 2012; Malin et al., 2010; Bell et al., 2003; Herkenhoff et al., 2003). The Microscopic Imager (MI) on the MER (maximum 30 μm/pixel resolution) and the Mars Hand Lens Imager (MAHLI) on the MSL rover (maximum 14 μm/pixel resolution) are arm-mounted cameras designed to image small-scale targets requiring close examination, such as fine-grained sediment (Edgett et al., 2012; Herkenhoff et al., 2003). By contrast, the PanCam on the MER (1 mm/pixel resolution) and MastCam on the MSL rover (150 and 450 μm/pixel resolution; Bell et al., 2003) are stereo-paired mast cameras best suited for analysis of coarse-grained deposits and geologic context supplementing higher resolution images.

The MER and MSL rovers have collected many thousands of sediment images that permit submillimeter-scale properties to be observed. Discoveries of soil formation mechanisms (McGlynn et al., 2011), compositional effects of sorting (Fedo et al., 2015), transport distances and provenances of sediment (Szabo et al., 2015; Cabrol et al., 2014), paleohydraulics of wind and water (Blake et al., 2013; Williams et al., 2013; Sullivan et al., 2008; Sullivan et al., 2005), geographical changes in sediment sources (Cabrol et al., 2008; Yingst et al., 2008), and interpretations of source rock lithologies (Yingst et al., 2013) have all been supported by measurements and analyses of textural properties from images. Rover images provide abundant opportunity to perform textural analyses and construct a comprehensive picture of the processes the shaped the surface.

Further study is required to understand how the use of 2D images as a medium for textural analysis compares to the direct measurement of 3D textures from actual sediment in Mars-relevant environments, where sediment is derived from dominantly basalt. For a homogenous sediment of equidimensional grains, textural observations made in 2D may not differ substantially from the same observations made in 3D. In natural sedimentary environments, including those on Mars, where grains are not equidimensional and textural properties between clasts are heterogeneous, 3D textures of sediment may be perceived inaccurately from 2D images. Grains may be positioned where their actual dimensions are not apparent (foreshortening), larger grains may be partially buried beneath the surface, and many grain margins may overlap. In addition to problems associated with two-dimensionality, the analysis of imaged sediment is further limited by camera capabilities that determine resolution and may also be subject to differences based on time of day illumination.

The purpose of this work is three fold: (1) to determine if 2D image analyses performed on high-resolution images can accurately describe 3D sediment textures, (2) to establish the effect of image resolution on textural image analysis, and (3) to determine the extent to which illumination angle (shadows) impacts the collection of textural data. This study uses images and sediment samples from basaltic fluvial and aeolian dune environments. Because these environments have been identified on Mars, the use of these sediments facilitates the comparison with martian sediment. Textural analyses include measurements of grain size, sphericity, and roundness. These textures are indispensable components for interpreting sedimentary processes and the results of this study are directly applicable to textural image analyses performed on martian sediments imaged by rover cameras (Grotzinger et al., 2012; Crisp et al., 2003).

2. MARS-ANALOG FIELD LOCATIONS

2.1 Selection of Analog Environments

Initial sediment textures, and the rates at which these textures mature, depends primarily on composition and igneous properties of the source rock. Sediment on Mars derives from a dominantly basaltic provenance and has initial textures influenced by mineralogy, vesicular, glassy, aphanitic, or porphyritic igneous textures. Because composition and associated igneous properties can play major roles in the development of sediment texture, this study utilizes terrestrial sediments composed of primarily basalt clasts. Mars has abundant modern and ancient sediments of aeolian and fluvial origin. Consequently, this study focuses on aeolian dune sediment near Moses Lake, WA, and active fluvial sediment near Death Valley, CA, which both derive from basaltic sources (Fig. 1).

2.2 Moses Lake Dunes, Washington

The Miocene Columbia River Flood Basalts cover over 200,000 km^2 (Barry et al., 2013), largely in central and eastern Washington. Between 15 and 13 ka the episodic breaching of an ice bridge by a large glacial lake on the northern Cordilleran Ice Sheet sent catastrophic flood waters across the basalts which scoured the rock and formed thousands of channels (Bandfield et al., 2001; Brentz 1923). The landscape is known today as the Channelized Scablands (Brentz, 1923). Basaltic sediment produced by catastrophic flooding and erosion of the Columbia River Basalts has since been reworked in a variety of sedimentary environments. In the Quincy basin of central Washington, sediment occurs as a broad aeolian dune field containing transverse, parabolic, and

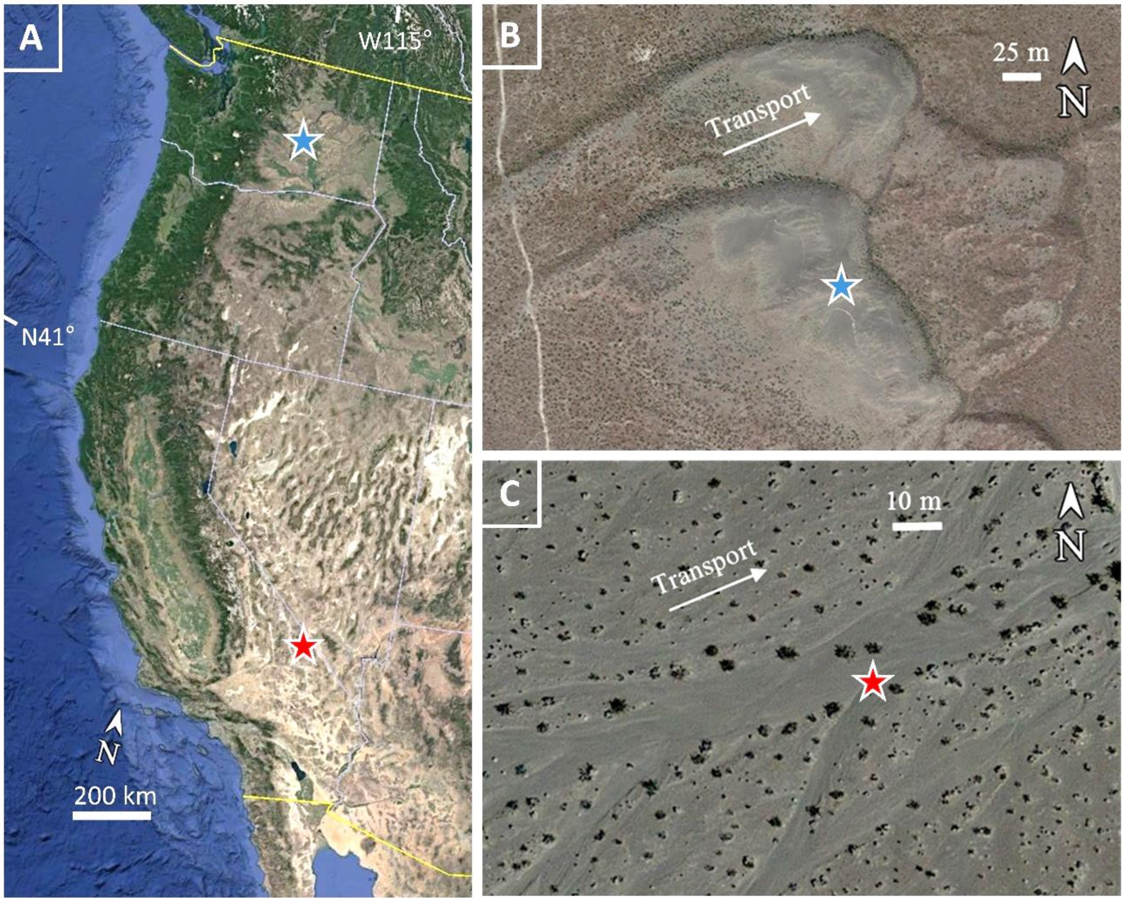

Figure 1: (A) Field work for aeolian sediment imaging and sampling was conducted in the Moses Lake Dunes, WA, denoted by the blue star in central Washington State. Field work for fluvial sediment imaging and sampling was performed in Mojave Desert, near Death Valley, CA, denoted by the red star in southern California. (B) Basaltic dunes of Moses Lake Dune Field, WA (N 47° 04.030', W 119° 14.337'). (C) Ephemeral fluvial channels near Death Valley Junction, CA (N 36° 15.505', W 116° 25.943').

barchan dunes (Fig. 1A, B; Fig. 2A-D; Edgett and Lancaster, 1993). Dune sediment is primarily composed of basalt (80%) produced from the scabland floods, with a smaller granodiorite component, likely derived from bedrock underlying the Columbia River Basalt flows, and minor clay, originating in the form of ash, from the 1980 eruption of Mount St. Helens (Sanders and Larson, 2011; Bandfield et al., 2001).

Aeolian sediment and images were collected on a secondary lee side of a parabolic dune located within the interior of the Moses Lake Dune field, WA (Figs. 1B, 2A). The imaged area was on a south east facing (S35°E), 25° dipping slope (strike S55°W). The imaged surface did not contain ripples or vegetation (Fig. 2B).

2.3 Death Valley Region, California

The present topography of the Death Valley region, eastern California, was formed by crustal extension that began approximately ~16 Ma (Miller and Wright, 2002). Crustal thinning resulting from extension was associated with significant igneous activity. Extrusive igneous rocks occur in the Black Mountains and Greenwater Range of the Central Death Valley Plutonic-Volcanic Field, which records nearly 11 million years of igneous processes (Thompson et al. 2014; Tibbetts, 2010; Miller and Wright, 2002). The Greenwater Range itself contains 24 volcanic centers, numerous exposed lava flows, scoria cones, and volcanic necks, with basaltic lavas comprising the most recent eruptions (~4 Ma; Tibbetts, 2010).

The rocks of the Greenwater Range shed basaltic sediment down an easterly draining braided fluvial system (Fig. 1C; Fig. 2E-H). The Death Valley region receives an average of 5 cm/yr of rain, however, desert environments are prone to irregularities in

Figure 2: (A) Aeolian sediment field site at Moses Lake Dunes, WA. Approximate field location shown in white box. Arrow points to ash layer from Mt. St. Helens eruption, May 1980. (B) Camera set-up for aeolian sediment imaging. Protractor and thin metal rods shown in image were used to measure solar angle in the field. Ruler in approximately 30 cm. (C) Aeolian sediment surface sampling “peel”. (D) Representative image of Moses Lake Dune aeolian sediment. (E) Fluvial sediment field site near Death Valley, CA. Approximate field location shown in white box. Basalts of the Greenwater Range in distance. (F) Camera set-up for fluvial sediment imaging. Ruler is approximately 30 cm. (G) Fluvial sediment surface sampling “peel”. (H) Representative image of Death Valley fluvial sediment.

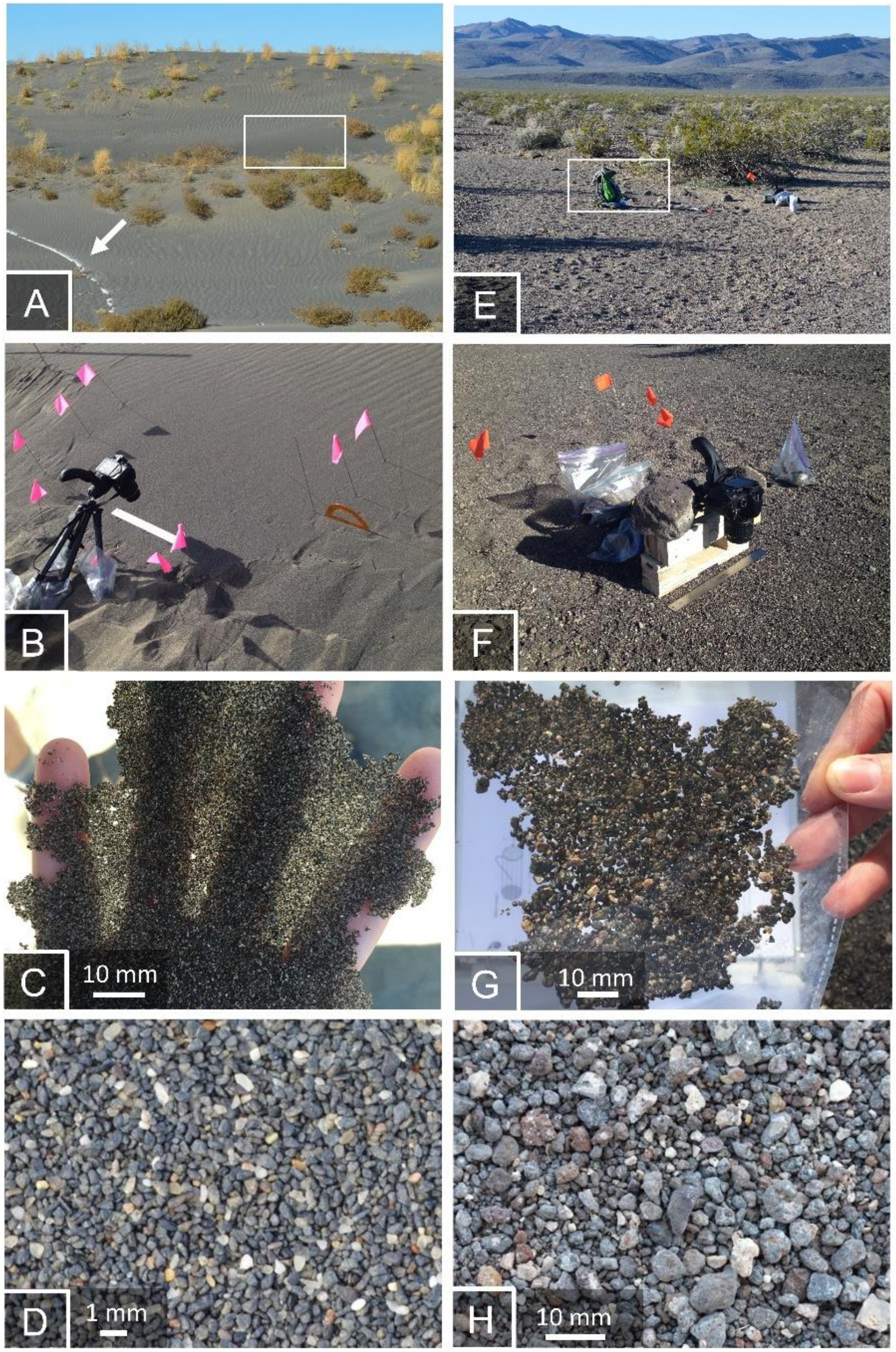

Figure 2: Continued.

rainfall amount and intensity (Roof and Callagan, 2003). Short-duration, high-intensity precipitation leads to energetic overland flows that have the capacity to form fluvial features. Sparse vegetation, low infiltration capacities of desert soils, and topographic relief, are ideal conditions for the formation of flash floods with high erosive potential and sediment competencies (Laity, 2008). Such events created the eastward-flowing ephemeral braided fluvial system that emanates from the Greenwater Range in Death Valley, CA.

Active channels of the braid plain where the fluvial sediment was collected incised an older surface to a shallow depth (Fig.2E, F). The channel contained pebbly sand, while the older surface was strewn with boulders. Image and sampling took place at a confluence of two fluvial channels < 5 km east of the Greenwater Range. The channel surface was flat and contained no vegetation.

3. METHODS

3.1 Field Images and Sample Collection

3.1.1 Sediment Images

A 24 megapixel Nikon® D3200 digital single-lens reflex camera was used to collect sediment images at the aeolian dune and fluvial sediment field sites (Fig. 2). During imaging the camera was fixed to a tripod and remained stationary for the duration of imaging. The camera was pointed perpendicular to the sediment surface and a high precision metal ruler was placed within the field of view so image resolution could be determined. To obtain images at the highest resolution, the camera was positioned as close to the sediment surface as possible without compromising focus and images were taken in the largest pixel size (6016 x 4000 pixels).

These conditions produced images roughly analogous to those taken by the MAHLI camera on the MSL rover. At a 2.1 cm working distance the 2 megapixel MAHLI camera can image up to 14 μm/pixel within a field of view of 2.2 x 1.7 cm (Edgett et al., 2012). The Nikon D3200 used in this work lacks focus at the closest working distances of MAHLI, but with 24 megapixels can obtain comparable image resolutions at farther distances. For the aeolian surface, the camera was placed approximately 13 cm from the surface, resulting in a 29 cm^2 (6.6 cm x 4.4 cm) field of view and an image resolution of 11 μm/pixel. Imaging of the fluvial surface required a slightly larger distance of 15 cm, resulting in a 62 cm^2 (9.6 cm x 6.4 cm) field of view and an image resolution of 19 μm/pixel.

To compare textures at different resolutions, the high-resolution images taken in the field were digitally resampled to progressively larger pixel sizes using Microsoft

Paint® software. Pixel dimensions of the high-resolution aeolian and fluvial images were successively decreased to approximately 20, 30, 40 and 50 μm/pixel for the aeolian sediment images (Fig. 3), and 40, 60, 80 and 100 μm/pixel for the fluvial sediment images (Fig. 4). To ensure resampled images are comparable to the same image taken directly by the camera at low resolution, the aeolian and fluvial sediments were natively imaged at both high (6016 x 4000 pixels) and a low (3008 x 2000 pixels) resolution. The high-resolution image was then resampled to the pixel dimensions of the low-resolution image. Visual comparison of these images confirm similarity and suggest that digital resampling of images to lower resolutions should have negligible effect on textural analysis (Fig. 5).

Images were collected at a range of times to produce differences in incident solar angle (Fig. 6). The incident angle from the sediment surface to the sun is the sum of the solar elevation from the horizon and the dip of the surface in the azimuth of the sun. As either of these two parameters increase, the angle from the surface to the sun is greater and shadows become shorter. Aeolian sediment imaging took place on a secondary lee side of a dune, which increased the maximum solar angle and the range of shadow lengths that could be imaged, yielding a maximum angle to the sun of approximately 60°. Incident solar angles were measured directly in the field, and images of the surface were taken during times of day when the incident solar angle to the surface was roughly 60°,

Figure 3: Images of aeolian sediment at the resolutions analyzed in this study. (A) Aeolian sediment at 11 μm/pixel image resolution. (B) Aeolian sediment at 20 μm/pixel image resolution. (C) Aeolian sediment at 30 μm/pixel image resolution. (D) Aeolian sediment at 40 μm/pixel image resolution. (E) Aeolian sediment at 50 μm/pixel image resolution.

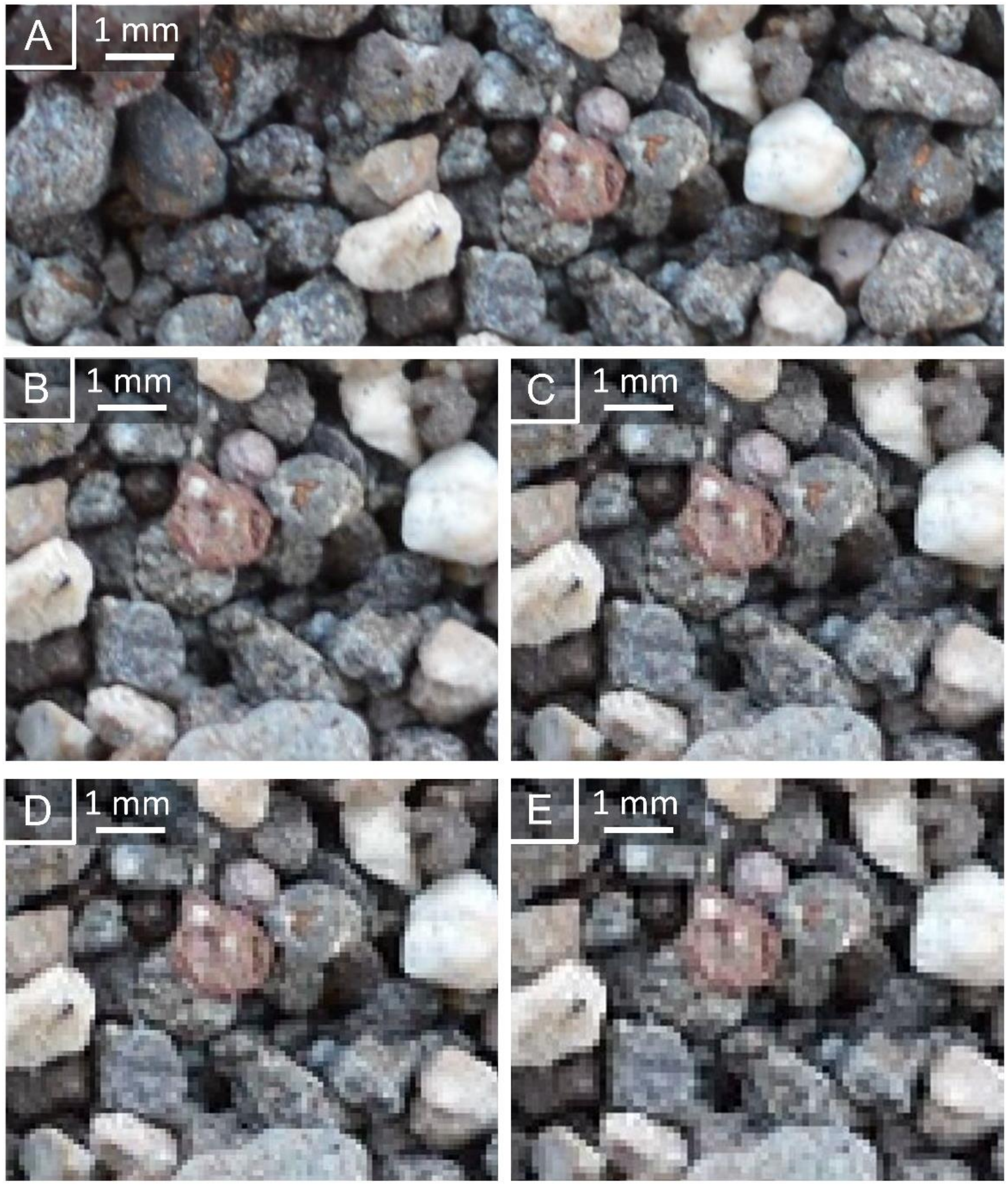

Figure 4: Images of fluvial sediment at the resolutions analyzed in this study. (A) Fluvial sediment at 19 µm/pixel image resolution. (B) Fluvial sediment at 40 µm/pixel image resolution. (C) Fluvial sediment at 60 µm/pixel image resolution. (D) Fluvial sediment at 80 µm/pixel image resolution. (E) Fluvial sediment at 100 µm/pixel image resolution.

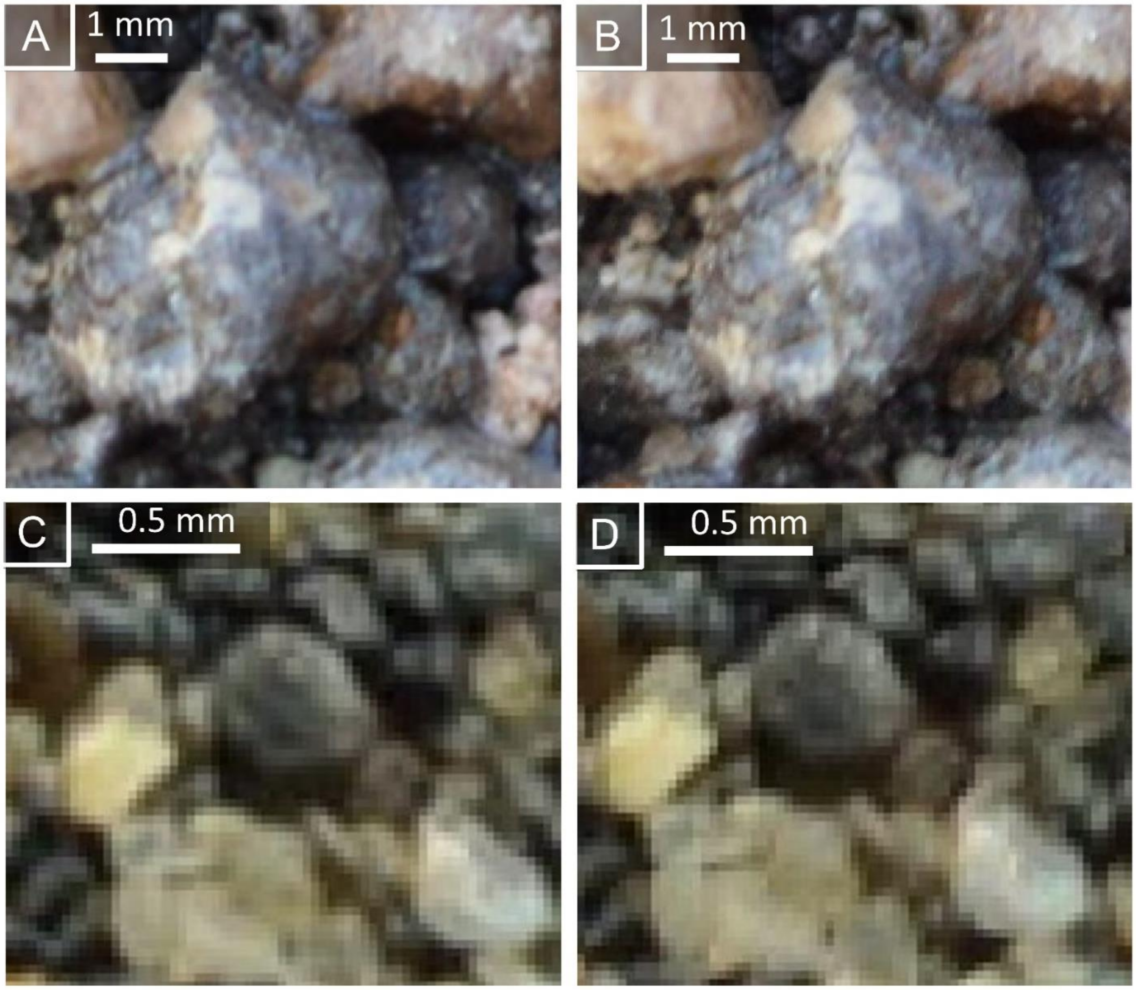

Figure 5: Comparison of native sediment images taken directly with the camera at a low resolution to images taken at high resolution and digitally resampled to low resolution. (A) Native low-resolution (3008 x 2000 pixels) image of fluvial sediment taken by the Nikon D3200 camera. (B) High-resolution (6016 x 4000 pixels) image of fluvial sediment digitally resampled to low resolution (3008 x 4000 pixels). (C) Native low-resolution (3008 x 2000 pixels) image of aeolian sediment taken by the Nikon D3200 camera. (D) High-resolution (6016 x 4000 pixels) image of aeolian sediment digitally resampled to low resolution (3008 x 4000 pixels).

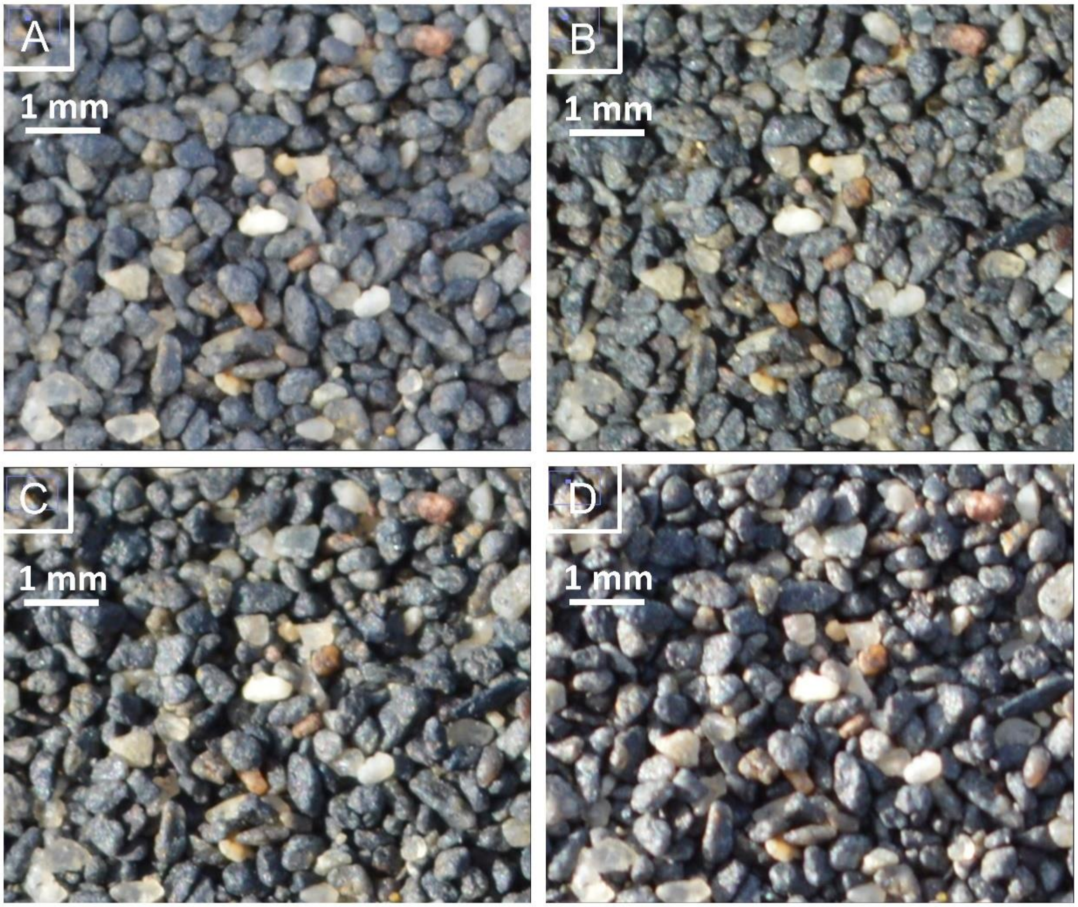

Figure 6: Representative images of aeolian sediment taken under different illumination conditions. (A) Aeolian sediment image taken under even illumination. (B) Aeolian sediment image taken at 60° incident solar angle. (C) Aeolian sediment image taken at 40° incident solar angle. (D) Aeolian sediment image taken at 20° incident solar angle.

50°, 40°, 30°, 20°, and 10°. An image under shaded (shadowless), bright solar illumination was also taken as a control image.

In the fluvial braid plain imaging took place on a horizontal surface as the topography was insufficient to provide a large range of solar incidence. The greatest solar angle to the surface was determined by the highest elevation reached by the sun at solar noon, which was about 30°. Images were taken at approximately 30°, 20°, and 10° solar angles, as well as under even illumination. Textural analyses of the fluvial images taken at different incident solar angles are not part of this study, but are presented in Bertram (2016). All images analyzed in this work are shown in Appendix A.

3.1.2 Sediment Sampling

After imaging, sediment from each site was collected using volumetric bulk sampling and areal surface sampling methods. In both locations, sampling of sediment from the small imaged area would not alone provide a sufficient volume of sediment for sieving. To obtain larger volumes of sediment, bulk and surface samples included sediment outside the imaged area where there was no change in surface texture. Bulk samples were collected from approximately 50 cm away from the imaged site and surface sediment samples included the sediment at the imaged site as well as surrounding sediment.

Bulk sampling is ideal because sieve distributions from volumetric samples are equivalent to grain-size distributions collected by the grid-by-number image analysis method used in this study (Kellerhals and Bray, 1971). Bulk sampling methods, however, are only valid representations of imaged sediment if the surface and subsurface are homogenous. Trenches dug into the sediment near each of the imaging sites revealed substantial textural variation with depth. It was clear, conventional bulk sampling would represent a sediment population different from the surface. To circumvent this problem, surface sediment was also collected by spraying with a clear enamel spray paint and allowing it to dry. The sprayed sediment was then “peeled” from the site sampling only the uppermost few grains of the surface (Fig. 2C, G). In the laboratory, sediment peels were washed with acetone to separate grains and remove the adhesive.

3.2 Two-Dimensional Textural Image Analysis Methods

3.2.1 Repeatability and Reproducibility of 2D Grain-Size Measurements

A single- and dual-user study was conducted to assess the repeatability and reproducibility of 2D grain-size measurements made using a Mars-analog impact-proxy sediment (Eibl et al., 2015; Fedo et al. 2015). Analog basaltic sediment was formed by comminution of a basalt sample from the Cima Volcanic Field in a jaw-crusher, and produced sediment with an average grain size of -0.68 Φ (very coarse sand). Sediment was poured onto a flat sheet of white paper, lightly flattened, and imaged under bright, even illumination perpendicular to the sediment surface (Friday et al., 2013). To evaluate reproducibility, two different users recorded short axis (D_i) and long axis (D_c) grain-size measurements for the same 50 grains in the image. To assess repeatability, one of the users performed the same analysis at a later date. Both users made grain-size measurements at 37 and 140 μm/pixel image resolutions.

Dual- and single-user measurements were then examined using the Concordance Correlation Coefficient (ρ_c) (Fig. 7). The ρ_c represents a statistical measure of the strength of agreement between quantitative measurements made by two different individuals or methods (Lin, 1989; Cox, 2006). The ρ_c equation calculates how far comparative data lie from the line of concordance (x=y) by considering both the accuracy and precision of measurement pairs. Ranging from -1 to 1, a ρ_c of -1 equals perfect negative agreement, 0 equals no agreement, and 1 equals perfect positive agreement among pairs. D_i and D_c measurement pairs at both image resolutions show $\rho_c > 0.98$ when measurements were repeated by the same user, and have $\rho_c > 0.93$ when reproduced by two different users. These coefficients indicate grain measurements performed at resolutions of 37 and 140 μm/pixel strongly agree when repeated by a single-user and when reproduced by a different user (Fig. 7).

3.2.2 Textural Data Collection

Textural data was collected from images superimposed by an alphanumeric grid. Grid nodes (intersections) were used as random sampling points to eliminate user bias in the selection of grains. Grains falling under a grid node were measured until the textures of 400 grains were collected. The following types of sampling points were omitted from the analysis and are not included into 400 grain total:

(1) A node that falls on a grain that is partially hidden by overlying grain(s),

(2) A node that falls in space between grains,

(3) A node that falls on the boundary of two touching grains,

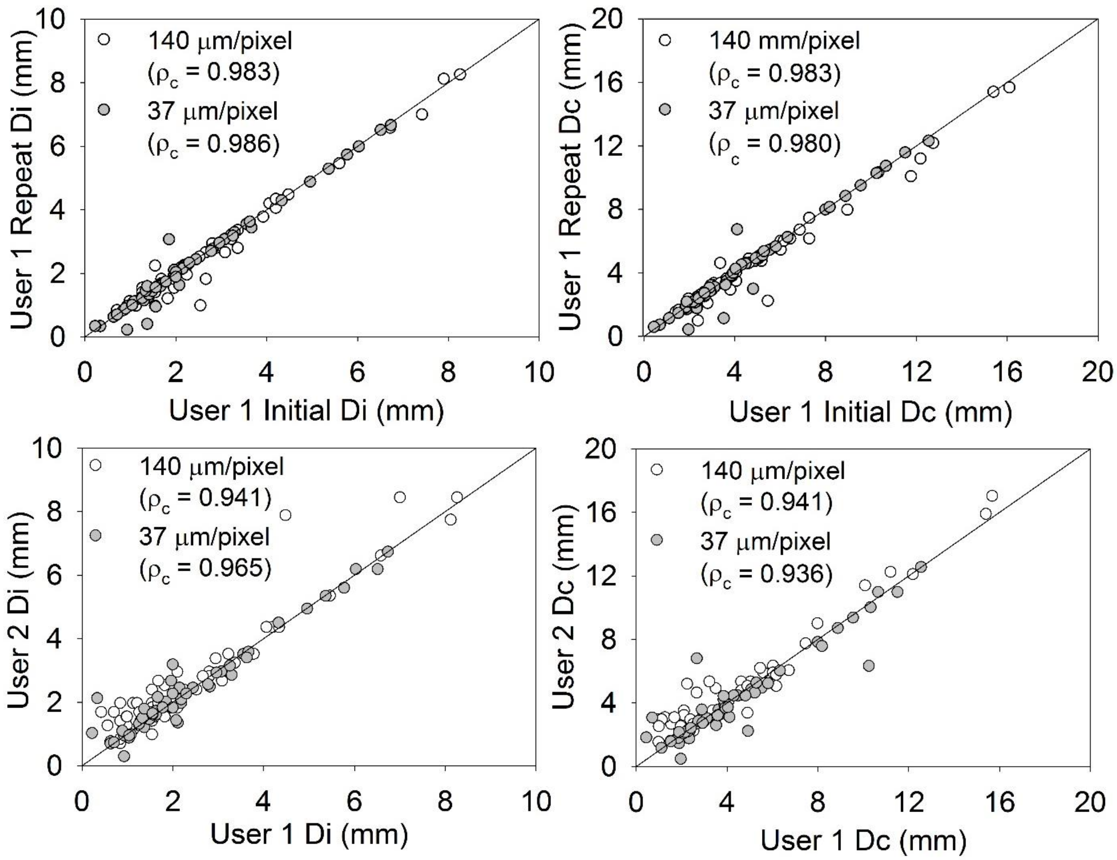

Figure 7: Plots showing agreement of single- and dual-user D_i and D_c grain measurements. Measurement agreement is shown for the image resolutions of 37 at 140 µm/pixel. Solid line is the line of concordance (x=y). Concordance Correlation Coefficients (ρ_c) are listed on plots. (A) Agreement of single-user D_i measurements. (B) Agreement of single-user D_c measurements. (C) Agreement of Dual-user D_i measurements. (E) Agreement of dual-user D_c measurements. Outlying measurement pairs, far from the line of concordance, resulted largely because some grain boundaries are difficult to interpret or because a grid line fell on a grid boundary and two different grains were measured. Examples of how user measurements with low agreement occur are shown in Appendix A.

(4) A node that falls on a grain whose boundary is hidden by a label or grid line,

(5) A node that falls on a grain not in focus (occurs along image perimeter).

3.2.3 Textural Measurements and Calculations

In 2D images, the longest grain dimension is equal to the diameter of the smallest circumscribing circle that can be fitted outside the grain boundary (D_c), and the smallest grain dimension is equal to the diameter of the largest inscribing circle that can be fitted inside the grain boundary (D_i). Grain size analyses of unconsolidated sediment images typically use the D_i axis which more likely to approximate grain size determined by sieving (Sime and Ferguson, 2003; McEwan et al., 2001). This is based on the assumption that short grain axes tend to be perpendicular to an image plane and intermediate and long grain axes parallel to an image plane. The validity of this assumption, however, depends on grain packing, shape, and degree of grain overlap (McEwen et al., 2003).

In this study, grain size is calculated by both D_i and D_c grain measurements to confirm the D_i measurement is most suitable for use in comparison with sieve grain-size distributions. Grain D_i and D_c measurements were converted to Phi (Φ) using Eq. (1),

$$\phi = -log_2(d) \qquad Eq. (1)$$

where d is either the D_i or D_c measurement, in mm. Grain sizes measured from each image were binned into 0.5 Φ intervals, which corresponds to sieve sizes used in this study. Grain-size histograms and cumulative frequency curves constructed using each the D_i and D_c grain measurements show the D_i measurement is a better approximation of the sieved grain-size distribution, which is consistent with assumed grain orientation (Fig. 8; Appendix C).

Although 2D grain-size distributions calculated using the D_i diameter are close approximations of 3D grain-size distributions determined by sieving (Fig. 8; Appendix C), differences in the collection and analysis of 2D (grid-by-number) and 3D (area-by-weight) grain-size data require conversion for equivalency. Conversion factors for grain-size distributions sampled and analyzed by different methods are given by Kellerhals and Bray (1971). These conversion factors were theoretically derived and can be applied to any sediment, sampling, or analysis method. The grain-size distributions from the evenly illuminated, high-resolution fluvial and aeolian images were converted using the appropriate Kellerhals and Bray (1971) factor for transforming a grid-by-number distribution to equal that of an area-by-weight distribution.

A comparison between the 2D, 2D converted, and sieve grain-size distributions shows only minor differences between the converted and original 2D data (Fig. 9). The conversion does not substantially alter grain-size frequencies and statistical parameters, for both the aeolian and fluvial sediments, remain largely the same (Fig. 9; Appendix C). Original grain-size distributions directly derived from image analysis are, therefore, considered valid comparisons to the actual sediment as efforts to improve the distribution proved futile. In the following results, grain size is calculated by Eq. 1 using the Di measurement, in mm, and no conversions are applied.

Common grain-size statistics (mode, average, sorting, and skewness) were calculated graphically from cumulative distributions using the Excel program

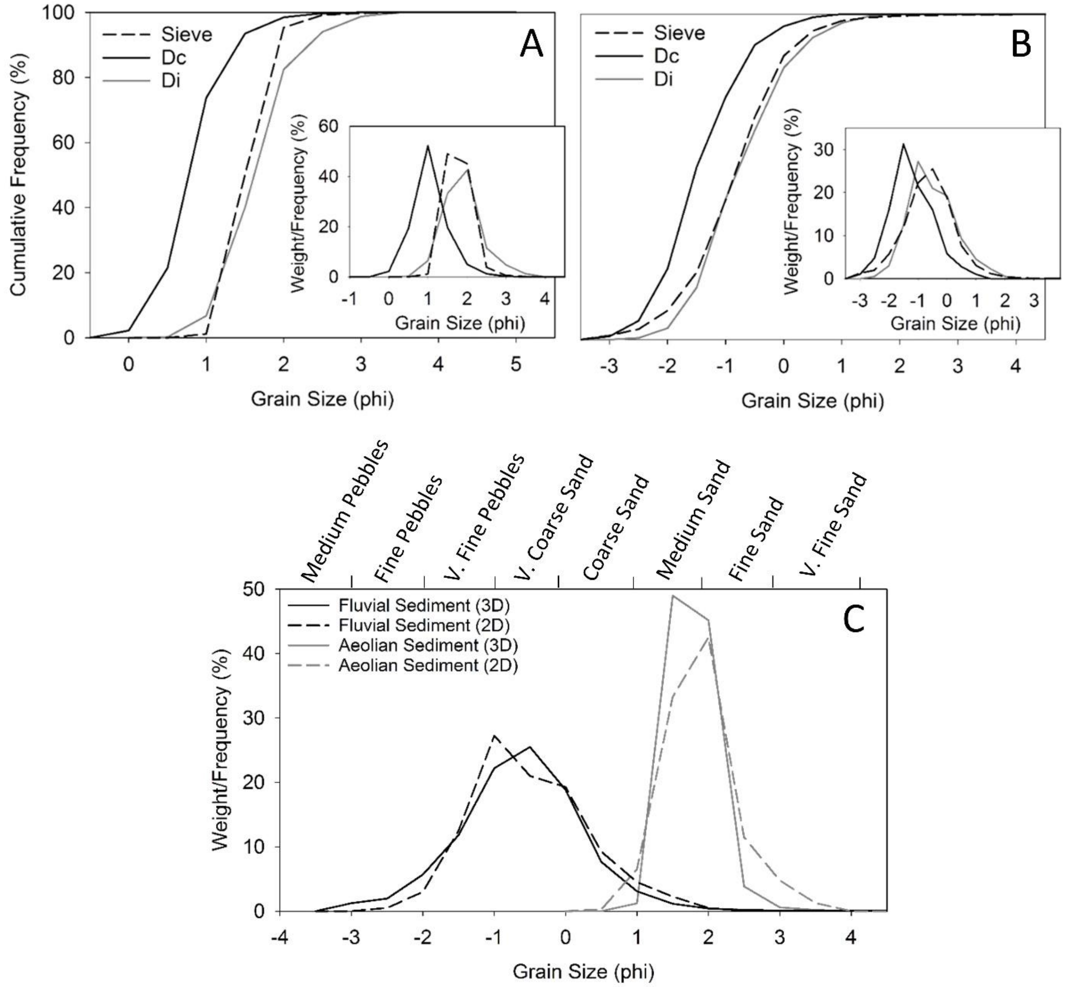

Figure 8: Comparisons of cumulative grain-size distributions derived from sieving and image analysis calculated using the D_c and D_i measurements. Frequency grain-size distributions are shown as insets. (A) Comparison of aeolian sediment D_i, D_c, and sieve distributions. (B) Comparison of fluvial sediment D_i, D_c, and sieve distributions. (C) Comparison of fluvial and aeolian grain-size distributions. Grain-size distributions from sieving (solid lines) and the image analysis, calculated using the D_i diameter (dashed lines), are shown.

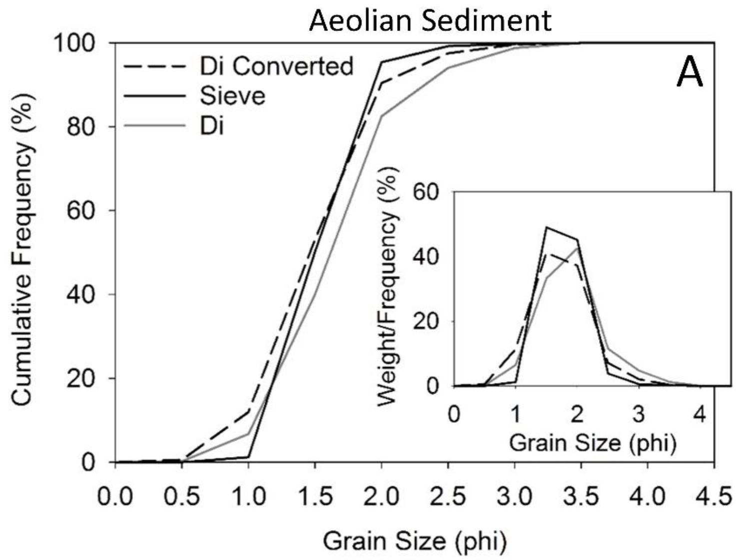

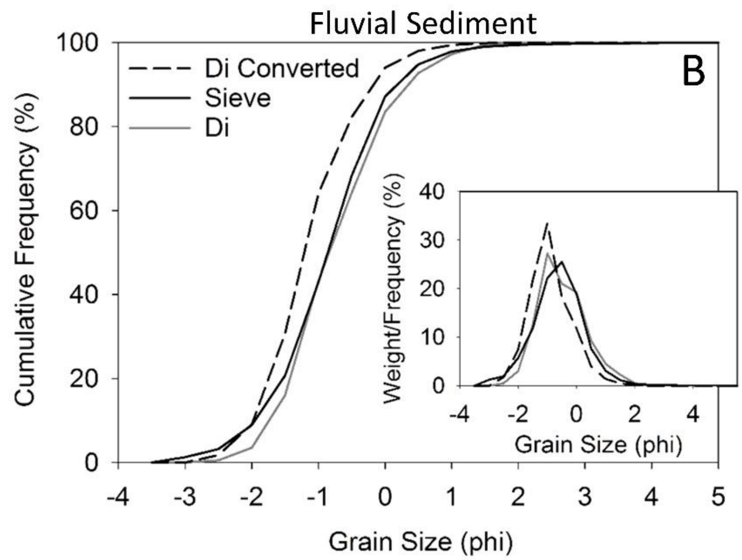

Figure 9: Comparisons of cumulative grain-size distributions from sieving, 2D image analysis, and 2D image analysis converted using the Kellerhalls and Bray (1971) conversion factor. (A) Aeolian sediment 2D original, 2D converted, and sieve distributions. (B) Fluvial sediment 2D original, 2D converted, and sieve distributions.

GRADISTAT (Blott and Pye, 2001, after Folk, 1957). The Udden-Wentworth grain-size chart and classifications for sorting, skewness, sphericity, and roundness are listed in Appendix E. Grain-size distributions are reported in Appendix Fand summary statistics are in Appendix G.

The mode (Mo) of the distribution is the most frequently occurring grain size and corresponds to the point of inflection on the cumulative curve. Other graphic statistics are calculated using grain diameters in Φ that correspond to specific percentiles on a cumulative distribution. This is denoted by a number preceded by "Φ" (e.g. Φ16), where the number is the percentile. Graphic mean grain size (M_Z) is calculated by Eq. 2.

$$M_Z = \frac{\phi16 + \phi50 + \phi84}{3} \qquad Eq. (2)$$

Sorting is a measure of uniformity in grain size and is calculated by the inclusive graphic standard deviation (σ_1) given by Eq. 3. Very well sorted sediment has a graphic standard deviation of <0.35 and extremely poorly sorted sediment >4.0.

$$\sigma_1 = \frac{\phi84 + \phi16}{4} + \frac{\phi95 + \phi5}{6.6} \qquad Eq. (3)$$

Skewness is a measure of distribution asymmetry, which is calculated by the inclusive graphic skewness (Sk_i) in Eq. 4. Skewness ranges from -1.0 to 1.0, where a fine skewed distribution has a positive skewness and a coarse skewed distribution a negative skewness.

$$Sk_i = \frac{\phi16 + \phi84 - 2(\phi50)}{2(\phi84 - \phi16)} + \frac{\phi5 + \phi95 - 2(\phi50)}{2(\phi95 - \phi5)} \qquad Eq. (4)$$

Grain sphericity is a measure of equality between grain axes and ranges from 0 to 1, where a value of 1 represents a perfectly spherical grain with equal axes. Because 2D image analysis can only measure two visible axes, sphericity is calculated in 2D using Riley sphericity (S_R) in Eq. 5. Two axes, the longest and shortest grain diameters, corresponding to the Dc and Di measurements, are used in S_R.

$$S_R = \sqrt{\frac{D_i}{D_c}} \qquad Eq. (5)$$

Grain roundness, which is independent of sphericity, is performed by a visual estimation of the sharpness of grain edges. Roundness is classified by comparison with a standard reference image depicting grains of increasing roundness corresponding to the Powers roundness scale (Powers, 1953), which ranges from 1 (very angular) to 6 (well rounded). While more detailed methods can provide quantitative roundness values (Heilbronner and Barrett, 2014; Janoo, 1998; Dobkins and Folk, 1970; Wentworth, 1919), the use of the Powers roundness reference image is a more efficient method of determining roundness in circumstances of high grain counts and manual image analysis methods. Histograms of roundness values are in Appendix H.

3.3 Three-Dimensional Textural Sediment Analysis Methods

3.3.1 Textural Data Collection

Aeolian dune and fluvial sediments were sieved into 0.5 Φ grain-size intervals using a Tyler Ro-Tap® Sieve Shaker. Each size fraction was weighed to obtain a grain-size distribution. A small number of grains were collected from each sieve size to determine single-grain sphericity and roundness. The number of grains measured in each sieve fraction was proportional to its frequency in the grain-size distribution. The number of grains analyzed in each size was calculated out of a 400 grain total. Because the image analysis grid method samples roundness and sphericity as a function of the grain-size distribution, this method eliminates the possibility of 2D and 3D sphericity and roundness differing as a result of sampling methods (Van der Plas and Tobi, 1965).

Measurement of grain axes for calculating sphericity was performed with a digital caliper. A microscope was used to assess grain roundness and to aid in sphericity measurements of small grains. Because of the difficulty in handling small grains, sphericity measurements could only be made for grains larger than 0.0 Φ (1 mm). Sphericity of the aeolian sediment could not be determined because all grain sizes were below 0.0 Φ.

3.3.2 Textural Measurements and Calculations

Like grain sizes determined in 2D, Equation 1 describes the logarithmic relationship of Φ to the mm grain size of sieved sediment, where the mm grain size (d) is the intermediate grain axis measured by sieving. Cumulative grain-size distributions determined from sieving were input into GRADISTAT (Blott and Pye, 2001, after Folk and Ward, 1957) to calculate the mode, mean, sorting, and skewness (Eq. 2 – 4). Grain sphericity measured from unconsolidated sediments expressing three dimensions, is defined by the maximum projection sphericity (ψ_P) in Equation 6,

$$\psi_P == \sqrt[3]{\frac{S^2}{LI}} \qquad Eq.(6)$$

where S, L, and I, are the short, long, and intermediate grain axes, respectively (Sneed and Folk, 1958). Grain roundness was visually estimated using the Powers Roundness Scale and reference image (Powers, 1953).

4. AEOLIAN DUNE SEDIMENT FROM MOSES LAKE, WA

4.1 Comparison of 2D and 3D Textures

4.1.1 Grain Size

<u>4.1.1.1 Description</u>

Aeolian sediment grain-size distributions and grain-size statistics determined in 3D and 2D are compared. Grain-size analysis of the high-resolution, evenly illuminated aeolian sediment image is compared to analyses of the 3D sediment to understand how well 2D image analysis determines 3D grain-size properties under ideal resolution and illumination conditions. The grain-size distribution determined from 2D image analysis ranges from 0.5 to 3.5 Φ (coarse to very fine sand) and the distribution determined from 3D sediment ranges from 0.5 to 4.0 Φ (coarse to very fine sand) by sieving (Fig. 10A, B). The 3D grain-size distribution shows 95% of grains fall into the 2.0 and 1.5 Φ bins (medium sand; Fig. 10A). Image analysis also found a high proportion (over 75%) of grains in this range (Fig. 10B). Grain-size distributions have similar means (M_z = 1.50 ±0.05 Φ) and modes (Mo = 1.50 ±0.25 Φ; Fig. 10C). Two sample K-S Test of the 2D and 3D distributions cannot reject the null hypothesis that the distributions come from the same population. Additionally, the imaged sediment is well sorted (σ_1 = 0.49 Φ) and the actual sediment is very well sorted (σ_1 = 0.33 Φ; Fig. 10D). Both 2D and 3D distributions are symmetrical with no clear skewness (Sk_i = 0.049 ±0.003; Fig. 10E).

<u>4.1.1.2 Interpretation</u>

The comparison of 2D and 3D data demonstrates the grain-size distribution determined from 2D image analysis is an excellent estimate of 3D sediment

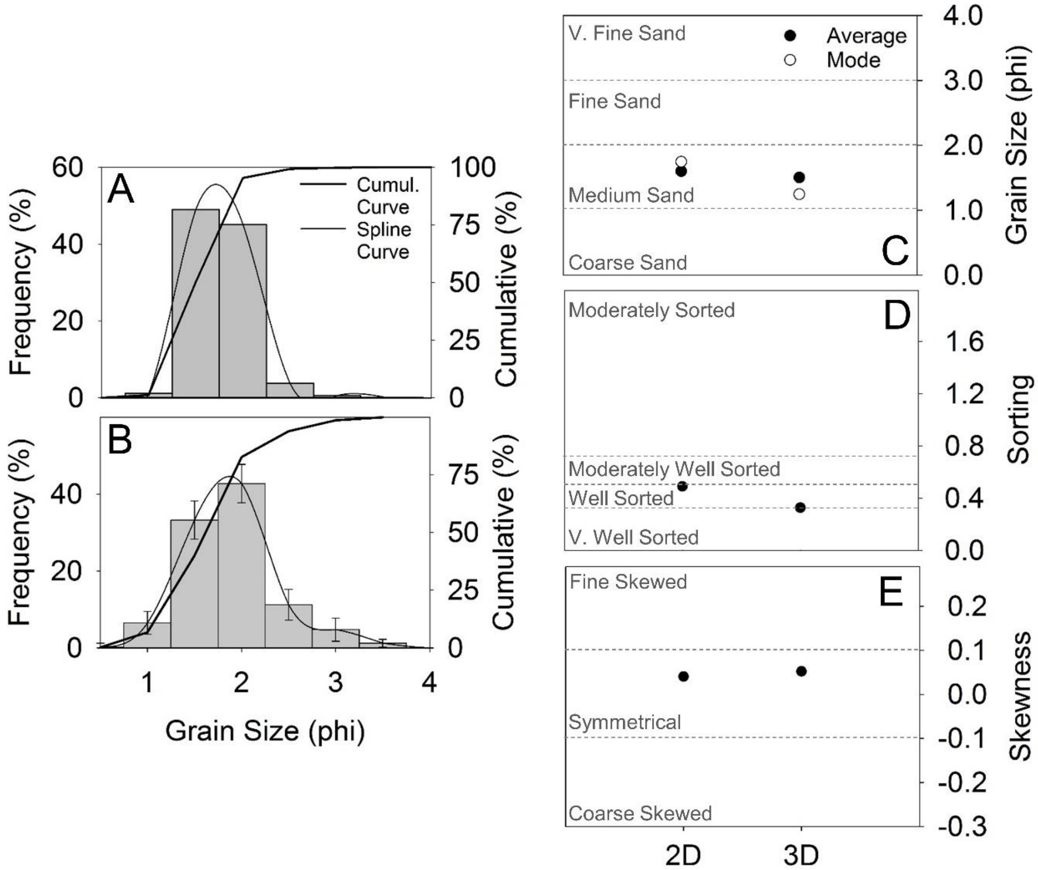

Figure 10: Comparison of textural parameters measured from the aeolian sediment using 2D and 3D methods of textural analysis. Histograms are fit with spline curves. Error bars show estimated error using the methods of Van der Plas and Tobi (1965). (A) Grain-size histograms and cumulative distributions determined by sieving of the 3D sediment (B) Grain-size histograms and cumulative distributions determined by image analysis. (C) Grain size averages and modes for 2D and 3D analyses. (D) Sorting for 2D and 3D analyses. (E) Skewness for 2D and 3D analyses.

characteristics (Fig. 10). Grain-size distributions from 2D and 3D measurements are concentrated within coarse to fine sand and the grain-size mean and mode are in medium sand (Fig. 10A-C). In 2D, the sediment is well sorted, and in 3D, sorting lies just below the border of well sorted into the very well sorted descriptive category. Similarity in grain size and sorting demonstrates critical sediment features (e.g. size and sorting as characteristics of dune sediment) of a coarse-to-fine sand can be accurately determined from a very high resolution 2D image (Fig. 10D, E).

4.1.2 Roundness

4.1.2.1 Description

Grain roundness determined from the 3D sediment and the 2D, high-resolution, evenly illuminated image are compared to determine how well roundness can be estimated from images. Assessed in 3D, roundness ranges from subangular to well rounded, and in 2D from angular to well rounded. Histograms of grain roundness determined in 2D and 3D show subrounded grains are most abundant in both data sets. Average roundness is 4.20 for the actual sediment and 4.25 for the image analysis (Fig. 11). Both populations show a small number of subangular grains followed by a large mode at subrounded, which makes up over 70% of the population in the actual sediment and over 50% in the sediment analyzed by image analysis. In both the 2D and 3D analyses, rounded grains compose 20-30% of the sediment, and well rounded grains <10%.

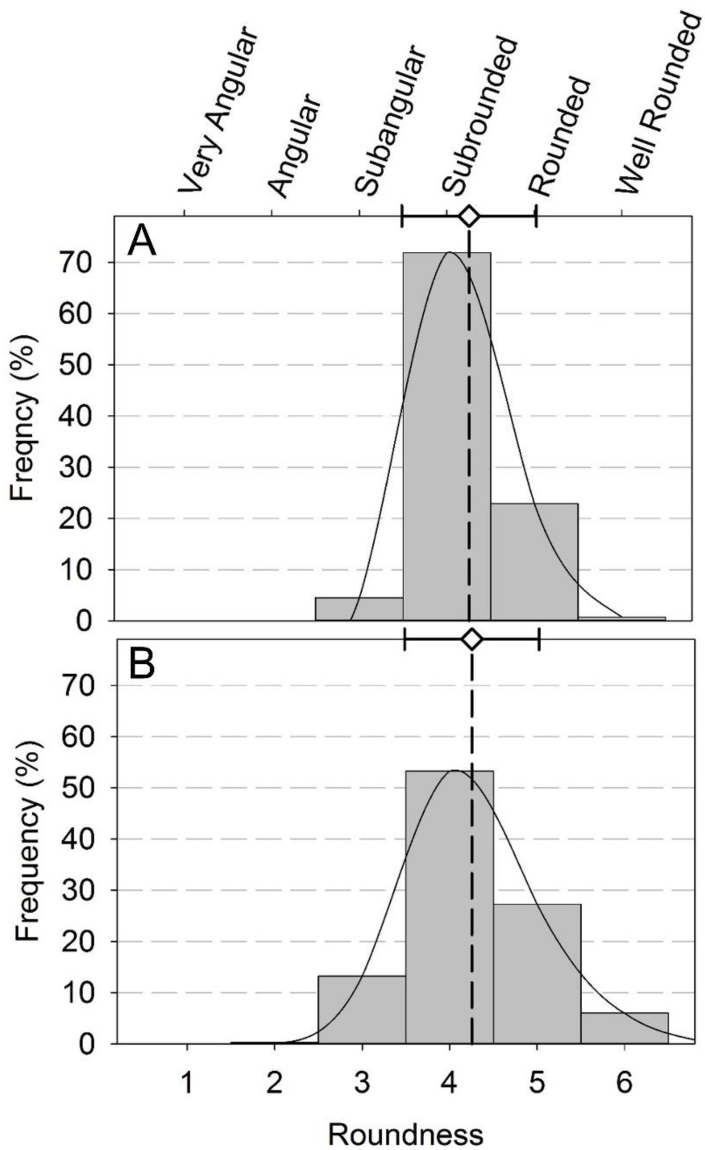

Figure 11: Histograms of 3D and 2D roundness values determined for the aeolian sediment. Histograms are smoothed with spline curve. Diamonds and dashed vertical lines show average roundness. Bars are one standard deviation. (A) Roundness determined from 3D microscope analysis of sediment. (B) Roundness determined from 2D image analysis.

4.1.2.2 Interpretation

Roundness estimated in 2D is statistically similar to actual sediment roundness determined in 3D. Averages calculated from the 2D and 3D data sets differ by 0.05, and are both subrounded. Additionally, histograms of grain roundness show subrounded grains were most frequently identified in both 2D and 3D analyses (Fig. 11). Relative to the mode, average roundness is slightly higher, which indicates a slight skew towards more rounded grains. An increase in rounded and well rounded grains is consistent with heavy abrasion by aeolian process and indicates characteristics relevant to interpreting the sediment's history can be identified through image analysis (Kuenen, 1960). These results suggest, the analysis of a high-resolution, near surface image of coarse to fine sand can resolve small-scale grain properties, such as angularity and surface texture, well enough to estimate roundness values similar to those determined from under a microscope.

4.2 Comparison of Different Image Resolutions

4.2.1 Grain Size and Sphericity

4.2.1.1 Description

To establish the effect of image resolution on grain-size analysis, the aeolian sediment grain-size distribution, grain-size statistics, and sphericity determined from the high-resolution (11 µm/pixel), evenly illuminated image are compared to distributions, statistics, and sphericities determined from the same image degraded to 20, 30, 40 and 50 µm/pixel images (Fig. 12). Grain-sizes measured from the 11 to 40 µm/pixel images range from 0.5 to 3.5 Φ (coarse to very fine sand) and at 50 µm/pixel from 0.5 to 3.0 Φ

Figure 12: Comparisons of textural parameters measured from the aeolian sediment at different resolutions. Histograms are fit with spline curves. Error bars show estimated error using the methods of Van der Plas and Tobi (1965). (A) 11 μm/pixel image grain-size distribution. (B) 20 μm/pixel image grain-size distribution. (C) 30 μm/pixel image grain-size distribution. (D) 40 μm/pixel grain-size distribution. (E) 50 μm/pixel image grain-size distribution. (F) Grain size average and mode at all image resolutions. (G) Sorting at all image resolutions. (H) Skewness at all image resolutions. (I) Distribution of grain sphericities from different resolution images showing the 90th, 75th, 50th, 25th, and 10th percentiles. Dashed lines mark categorical descriptions of sphericity (Appendix D).

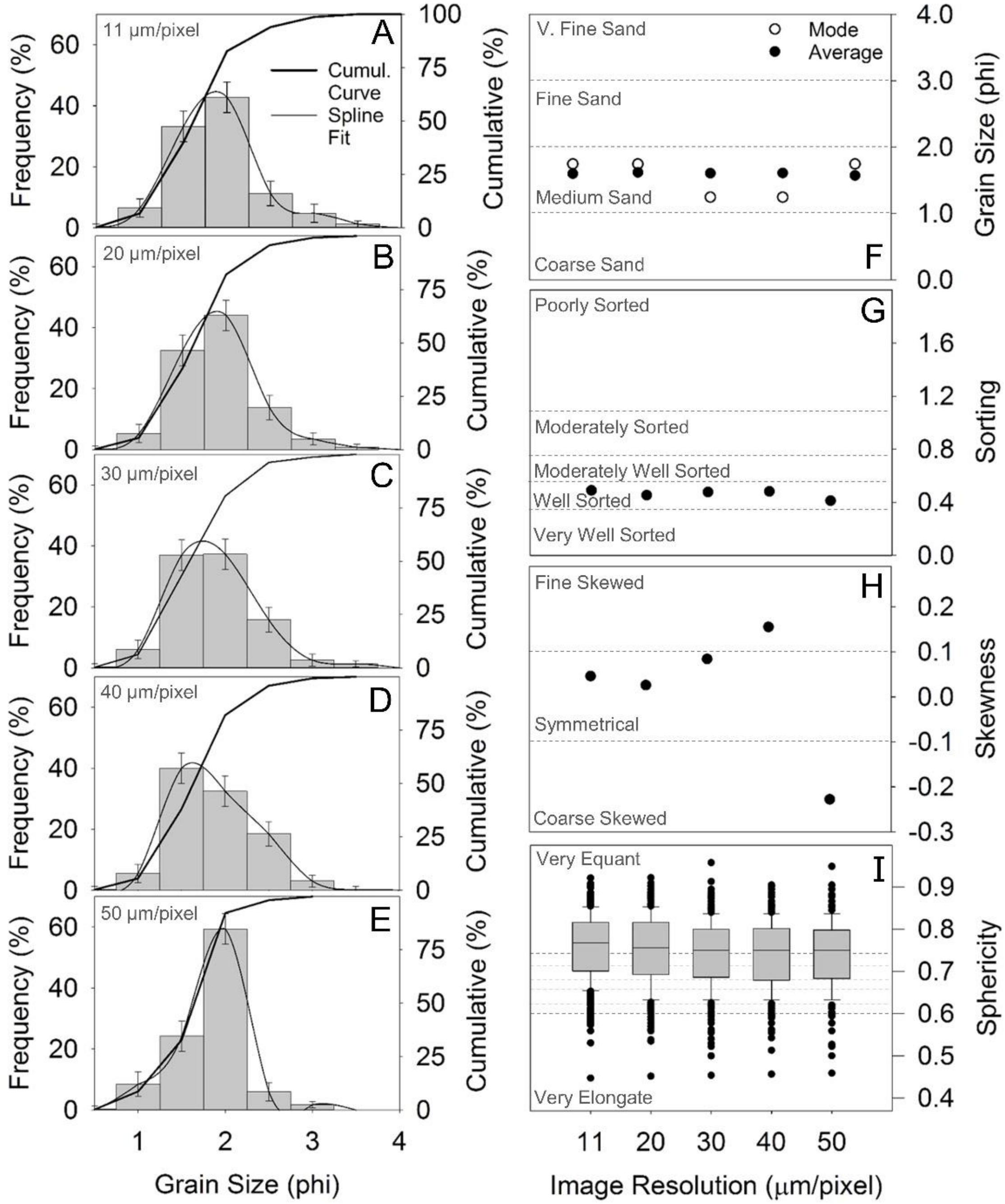

Figure 12: Continued.

(coarse to fine sand; Fig. 12A-E). The size distribution determined from the 20 μm/pixel image reproduced the distribution measured from the 11 μm/pixel image within 2.5% (Fig. 12A, B). At 30 μm/pixel, frequencies were replicated with slightly less precision, but remain within 10% of the 11 and 20 μm/pixel distributions (Fig. 12A-C). At all resolutions, the grain-size mean (M_z =1.59 ±0.02 Φ) and mode (Mo = 1.5 ±0.25 Φ) occur within medium sand and the sediment is classified as well sorted (σ_1 = 0.4 ±0.04 Φ; Fig. 12F). When resolution is decreased to 40 and 50 μm/pixel, grain size frequencies change enough to alter skewness (Fig. 12H). At 40 μm/pixel the distribution is fine skewed (Sk_i = 0.15) and at 50 μm/pixel coarse skewed (Sk_i = -0.23). Grain-size distributions from the 20 to 50 μm/pixel images compared to that of the 11 μm/pixel image cannot be rejected by a two-sample K-S Test. At all image resolutions, sphericity ranges from very equant (ψ_P = 0.67 ±0.01), to very elongate (ψ_P = 0.45 ±0.1), has a median within very equant (ψ_P = 0.76 ± 0.01), and an interquartile range between very equant and intermediate shape (Fig. 12I).

4.2.1.2 Interpretation

Grain-size analyses of the aeolian sediment at resolutions of 11-to-50 μm/pixel, show the grain-size mean, mode, and sorting can be determined regardless of image resolution. Grain-size means and modes are in medium sand and the sediment is classified as well sorted at all resolutions (Fig. 12 F, G). Furthermore, the exact same grain-size range was determined from images of 11-to-40 μm/pixel (0.5 – 3.5 Φ; coarse to very fine sand). At 20 μm/pixel, the grain-size distribution differs by less than 2.5% from the 11 μm/pixel distribution, and at 30 and 40 μm/pixel, by less than 10%.

Grain sizes in the 3.5 Φ bin (very fine sand) were not resolved at 50 μm/pixel and the grain-size range is 0.5 Φ shorter than the range determined from the 11 μm/pixel image (Fig. 12A-E). Neither the mean, mode, or sorting, however, are affected by this difference (Fig. 12F, G). Notable changes in skewness occur at 40 and 50 μm/pixel. The grain-size distribution at 40 μm/pixel is only slightly fine skewed but at 50 μm/pixel is transformed to a coarse skewed distribution (Fig. 12H). In the grain-size distribution of the 50 μm/pixel image, sizes ≥ 2.0 Φ comprise a larger fraction of the distribution because grains at 3.5 Φ were not resolved and fewer grains were observed ≤ 2.5 Φ. These changes resulted in the coarse skewness of the 50 μm/pixel grain-size distribution.

Many similarities are observed between the distributions of sphericity values measured from each image resolution. Sphericity measured at all resolutions has a range, interquartile range, and median in the same descriptive category. Even sphericity measurements at the most degraded image resolution, 50 μm/pixel, exhibit minimal difference from those measured at high resolution. Results of this work show, for a medium sand with a wide range of sphericity (0.4 to 1.0) and a median of approximately 0.75, image resolution has a negligible effect on the measurement of grain sphericity to 50 μm/pixel (Fig. 12I).

4.2.2 Roundness

4.2.2.1 Description

To establish the effect of image resolution on the estimation of roundness in 2D, roundness of the aeolian sediment determined from the evenly illuminated, 11 μm/pixel image is compared to roundness determined from the same image degraded to 20, 30, 40 and 50 μm/pixel (Fig. 13). Histograms of roundness values estimated from the 11-to-50 μm/pixel images show subrounded grains form the mode and most grains are subangular or subrounded (Fig. 13). Average roundness is near subrounded regardless of image resolution and standard deviations range from 0.77 to 0.95. Histograms for the 11 and 20 μm/pixel images are slightly skewed towards more rounded grains, shown by the shift of the average from the mode towards higher roundness values (Fig.13A, B). Corresponding with increases in angularity, the distribution of roundness values in the 30, 40, and 50 μm/pixel images become progressively more symmetrical, or slightly coarse skewed, and show a more even spread of values (Fig. 13C-E).

4.2.2.2 Interpretation

Histograms of grain roundness estimated from the 11-to-50 μm/pixel images are described by a similar mode, average, and standard deviation. At all resolutions, the mode and average are subrounded and differences in standard deviation are negligible. A wide range of roundness was also identified at each image resolution, with values ranging from very angular or angular to well rounded. Roundness estimates from all image resolutions share statistical properties, however, the strongest similarities in frequencies of the grain-size distributions are observed between the roundness estimates collected at 11 and 20 μm/pixel image resolution. This suggests roundness, at this grain size, can be determined extremely well between 11 and 20 μm/pixel, which includes the maximum resolution of MAHLI (Fig. 13A, B; Yingst et al., 2016).

At 30 μm/pixel analyses of roundness identified a larger proportion of angular grains and produced a more symmetrical distribution of roundness (Fig. 13C). The wider

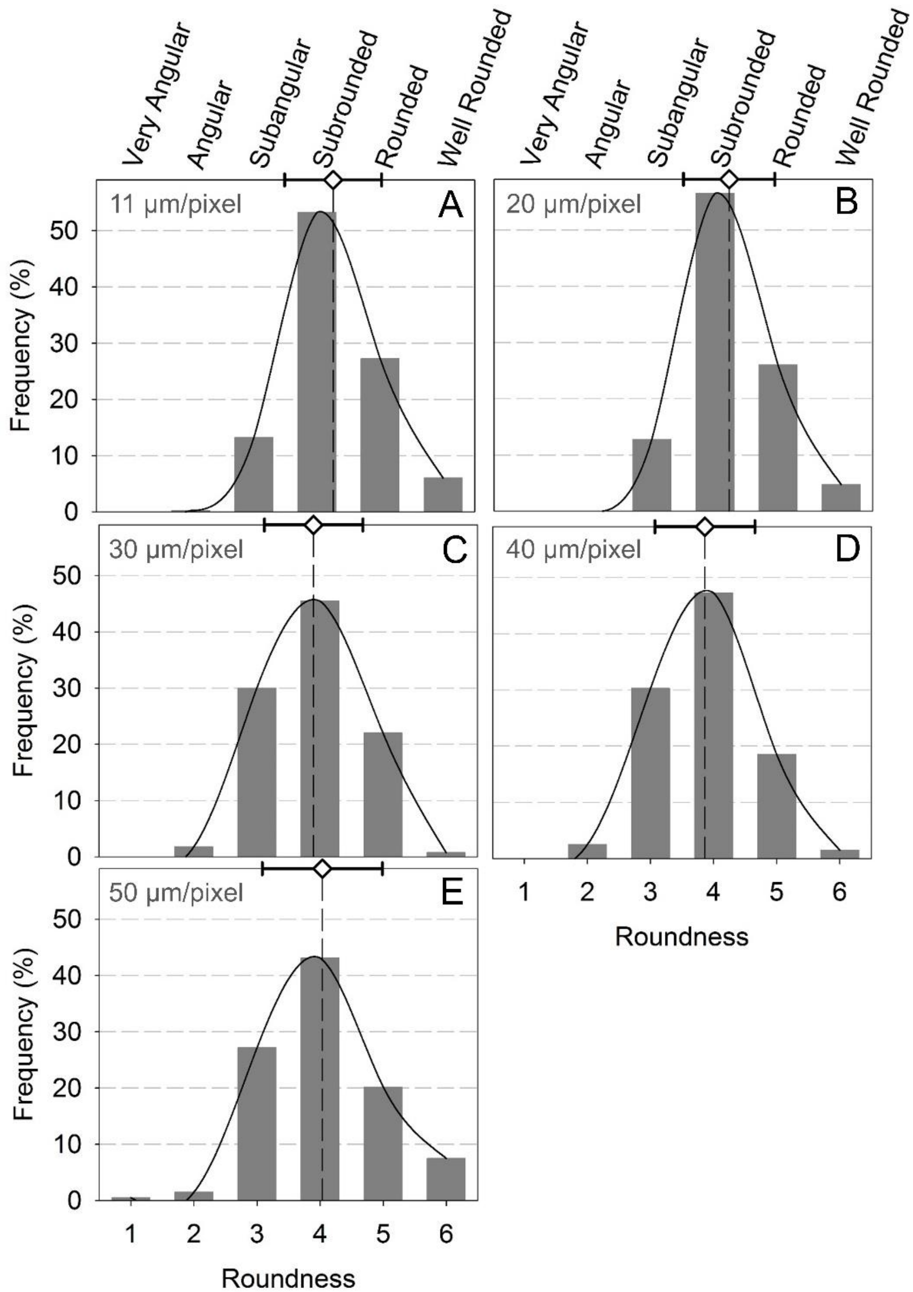

Figure 13: Aeolian sediment roundness histograms constructed from images of different resolutions. Histograms are fit with spline curves. Diamonds and dashed vertical lines show average roundness. Bars are one standard deviation. (A) 11 μm/pixel image roundness histogram. (B) 20 μm/pixel image roundness histogram. (C) 30 μm/pixel image roundness histogram. (D) 40 μm/pixel image roundness histogram. (E) 50 μm/pixel image roundness histogram.

spread of roundness values at this resolution may result from both pixilation of grain edges, which may exaggerate grain angularity, and the inability to resolve small-scale grain features that are below the limit of resolution. These results suggest the analysis of grain roundness from MI images (maximum 31 μm/pixel) containing coarse to fine sand may not be able to determine roundness as precisely as the same analyses performed at higher resolution (20 μm/pixel and above). Histogram frequencies between the 30, 40, and 50 μm/pixel image change very little indicating that decreasing the image resolution to 50 μm/pixel does not have any further effect on visual estimations of grain roundness (Fig. 13C-E).

4.3 Shadowed Grain Comparison

4.3.1 Grain Size and Sphericity

4.3.1.1 Description

The aeolian sediment grain-size distribution, statistics, and sphericity determined from the evenly illuminated, 11 μm/pixel image are compared to those determined from images that contain shadows of different lengths, corresponding to incident solar angles of 20°, 40°, and 60°, to establish whether image shadows affect grain-size analysis. All grain-size distributions range from coarse to very fine sand (Fig. 14A-D). In the evenly illuminated and 20° incident angle images grain size ranges from 0.5 to 3.5 Φ, in the 40° image 1.0 to 3.5 Φ, and in the 60° image 1.0 to 4.0 Φ (Fig. 14A-D). All of the distributions have a mean (M_z =1.61 ±0.04 Φ) and mode (Mo = 1.5 ±0.25 Φ) within medium sand (Fig. 14E). In the evenly illuminated, 20°, and 40° incident angle images, the sediment was determined to be well sorted (σ_1 = 0.47 ±0.03) and in the 60° incident

Figure 14: Comparisons of textural parameters measured from the aeolian sediment from images taken at different incident solar angles. Histograms are fit with spline curves. Error bars show estimated error using the methods of Van der Plas and Tobi (1965). (A) Even illumination image grain-size distribution. (B) 20° image grain-size distribution. (C) 40° image grain-size distribution. (D) 60° image grain-size distribution. (E) Grain size average and mode for all incident angle images. (F) Sorting for all incident angle images. (G) Skewness for all incident angle images. (H) Distribution of grain sphericities from all incident angle images showing the 90th, 75th, 50th, 25th, and 10th percentiles. Dashed lines mark categorical descriptions of sphericity (Appendix D).

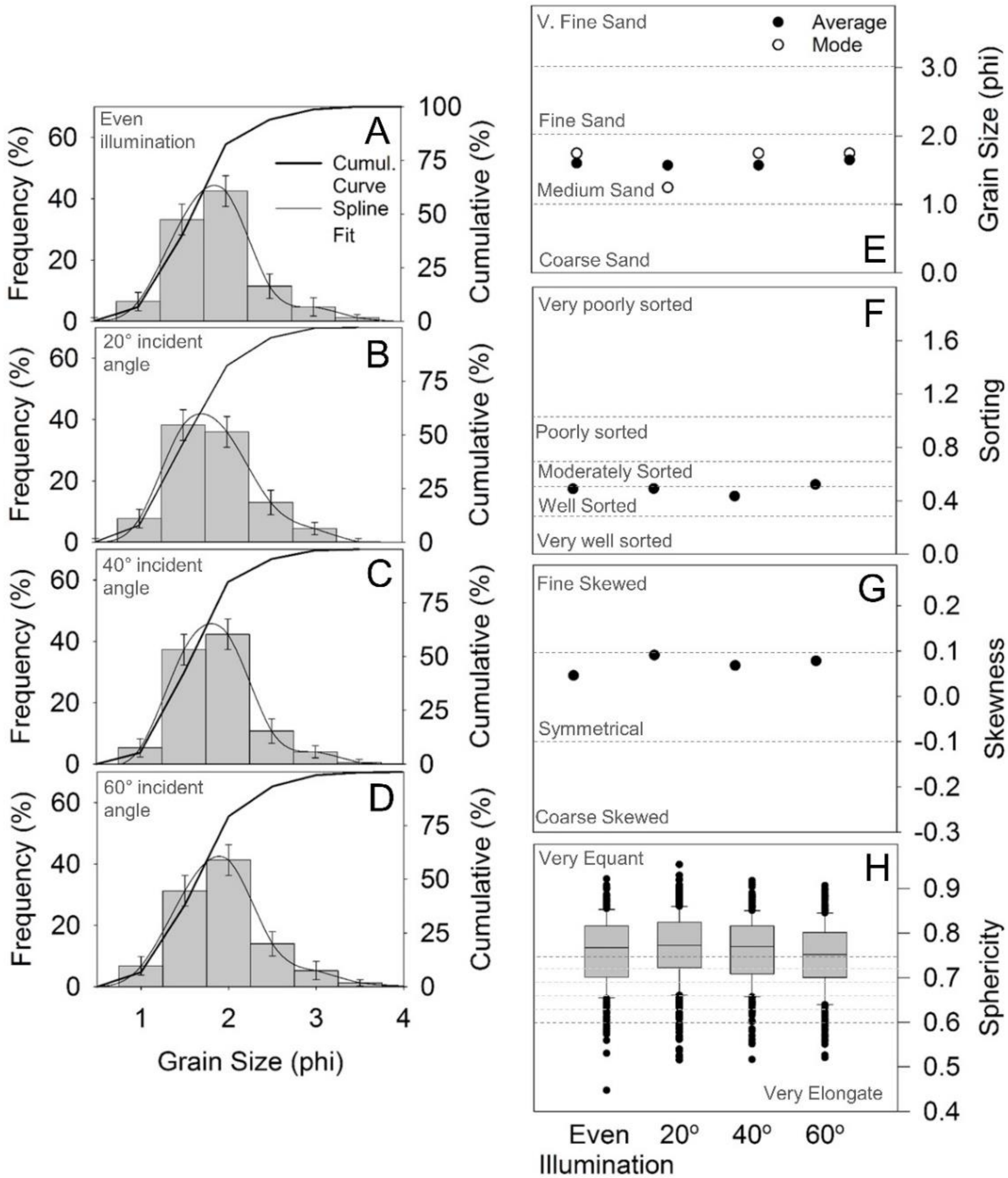

Figure 14: Continued

angle image moderately sorted (σ_1 = 0.52; Fig. 14F). All distributions are symmetrical (Sk_i = 0.07 ±0.03; Fig. 14G). Grain-size distributions from the 20°, 40°, and 60° incident angle images compared to evenly illuminated image grain-size distribution cannot be rejected by a two-sample K-S Test. Median sphericities measured from the even illumination image, 20°, and 40° incident angle images are 0.77 and from the 60° incident angle image 0.75. Each image has a similar interquartile range of 0.10 ±0.01 and total range of approximately 0.5 to 0.9 (Fig. 14H).

4.3.1.2 Interpretation

Shadows, particularly as they grow in length, have the potential to hide small grains or obscure parts of grains, which could affect grain-size measurements. Resultant effects may include a shortened grain-size range and shifts in frequencies that alter grain-size statistics. Grain-size measurements made on images with varying shadow lengths and an evenly illuminated image, however, are very similar (Fig. 14). Grain-size distributions, when measured from the images taken at different incident angles, have the same range, mean and mode in medium sand, sorting near the border of moderate and well sorted, and a symmetrical distribution (Fig. 14A-G). These results suggest increasing shadow length does not hide smaller grains nor obscure portions of grains as negligible changes in grain-size distributions, or statistics, were observed.

A similar conclusion is derived for sphericity measurements performed on the images taken at different incident angles. The median sphericity determined from the 60° incident angle image is slightly lower compared to the other images, but all medians lie within the very equant range, have a spread of values ranging from very equant to very elongate, and are mostly between subelongate and very equant. These results suggest shadows casted at incident solar angles of 20°, 40°, and 60°, in images of coarse to very fine sand, do not affect the 2D sphericity measurements.

4.3.2 Roundness

4.3.2.1 Description

To establish the effect of image shadows on the estimation of roundness in 2D, grain roundness determined from the aeolian sediment, evenly illuminated, 11 μm/pixel image is compared to roundness determined from images taken at 20°, 40°, and 60° incident angles. In all images, angular to well rounded grains were identified. Histograms of roundness values estimated from the evenly illuminated image and images at different incident angles show the mode ($\rho = 4$) and average roundness ($\rho = 4.1 \pm 0.12$) are subrounded (Fig. 15). For all images, standard deviations range from 0.77 to 0.93.

Roundness determined from the even illumination image is slightly skewed towards more rounded grains, shown by the shift of the average towards more higher values relative to the mode. Histograms of roundness in the images taken at different incident angles become slightly more symmetrical and equally distributed as incident solar angle increases (Fig. 15A-D). Analyses of roundness in images taken at 40° and 60° incident angles produced more angular grains than in the even-illumination and 20° incident angle images.

4.3.2.2 Interpretation

Histograms of grain roundness estimated from the evenly illuminated image and the images taken at different incident angles are described by a similar mode, average,

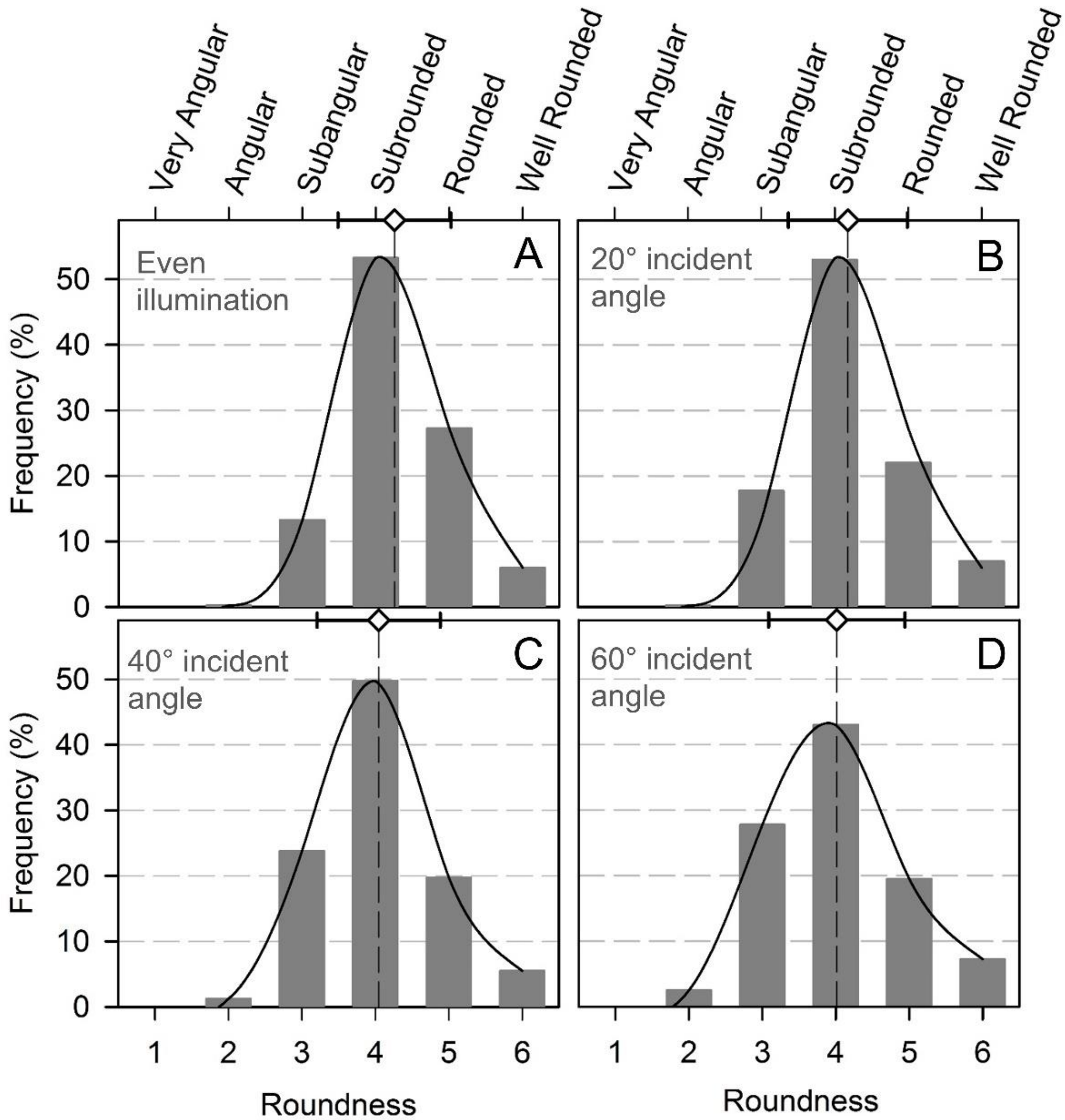

Figure 15: Aeolian sediment roundness histograms constructed from images taken at different incident solar angles. Histograms are fit with spline curves. Diamonds and dashed vertical lines show average roundness. Bars are one standard deviation. (A) Even illumination image roundness histogram. (B) 20° incident angle image roundness histogram. (C) 40° incident angle image roundness histogram. (D) 60° incident angle image roundness histogram.

and standard deviation. Regardless of illumination condition, histograms of roundness show the mode and average roundness are subrounded and differences between standard deviations are negligible (Fig. 15). A wide range of roundness was also identified in each image, with values similarly ranging from angular to well rounded. Roundness estimates from all images share statistical properties, however, the strongest similarities in roundness frequencies are observed between the evenly illuminated and the 20° incident angle images. In the 40° and 60° incident angle images histograms of roundness become more symmetrical, and the amount of subangular grains slightly increases (Fig. 15).

When the solar angle is high, sunlight travels through less atmosphere than when the solar angle is low and produce shadows that are darker and sharper than shadows at low solar angles that are softer (Gabler, 2008; Lillesand, 2007). Long soft shadows may more closely mimic the low contrast conditions of even illumination, while darker, shaper shadows at high solar angles have the capacity to obscure portions of grains and cause them to appear more irregular and angular. The strength or sharpness of the shadows, as opposed to shadow length, may have a greater influence on determining roundness in image analysis than shadow length. On Mars, shadow sharpness, or strength, could also be related to solar angle as atmospheric dust has the capacity to both absorb and block incident sunlight (Kok, 2010; Leovy 2001).

4.4 Summary: Textural Analysis of Aeolian Dune Sediment

Aeolian sediment collected from the Moses Lake Dune field was studied in three ways. First, grain-size measurements and estimations of roundness from the 3D sediment and the evenly illuminated, high-resolution image were compared. Results show the grain-size range, average, mode, sorting, and skewness measured in 2D accurately describes these properties of the 3D sediment. Analyses of roundness showed the range, average, and standard deviation of roundness values estimated form the aeolian sediment can also be accurately determined from 2D images.

With strong accuracy obtained from the textural analysis of the high-resolution image, a second analysis comparing grain-size, sphericity, and roundness measured from the high-resolution (11 μm/pixel) image and the same analyses at 20, 30, 40 and 50 μm/pixel was performed. The grain-size mean, mode, and sorting were successfully characterized to image resolutions of 30 μm/pixel and distribution frequencies remained within 10% of the high resolution image grain-size distribution to a resolution of 40 μm/pixel. Distribution frequencies and skewness, however, were observed to change in analyses performed at resolutions of 50 μm/pixel. Estimates of grain roundness determined the range, average, mode, and standard deviation were similar across all image resolutions. A resolution of 20 μm/pixel, however, yielded results most similar to those of the 11 μm/pixel image. Sphericity measurements in 2D show negligible change when analyzed from 11 to 50 μm/pixel.

The third analysis compared 2D grain-size, sphericity, and roundness from the high-resolution, evenly illuminated, aeolian sediment image to images taken at 20°, 40°, and 60° incident solar angles. Analyses of grain-size distributions, grain-size statistics, and measurements of sphericity found only minor differences between the images indicating these parameters are not affected by shadows of different lengths. Additionally, roundness ranges, averages, and standard deviations were similar regardless of illumination. Slight increases in the angularity of roundness values were observed at

40° and 60° incident angles which likely results from darker, sharper shadows casted at high solar angles obscuring portions of grains and causing them to appear more angular.

No strong relationships were identified between textural parameters analyzed from the 2D and 3D aeolian sediment (Appendix I), with statistics are summarized in Appendix J. All raw data collected from the 2D and 3D aeolian sediment in the above three analyses can be located in the attached Excel file.

5. FLUVIAL SEDIMENT FROM DEATH VALLEY, CA

5.1 Comparison of 2D and 3D Textures

5.1.1 Grain Size and Sphericity

5.1.1.1 Description

Fluvial sediment grain-size distributions and grain-size statistics determined in 3D and 2D are compared. Grain-size analyses of the high-resolution, evenly illuminated fluvial sediment image are compared to analyses of the 3D sediment to understand how well 2D image analysis determines 3D grain-size properties under ideal resolution and illumination conditions. The 3D sediment has a grain-size range of -3.0 to 5.0 Φ (fine pebble to coarse silt), while the range determined from 2D image analysis is -2.5 to 2.0 Φ (very fine pebble to medium sand; Fig. 16A, B). Grain-size means for the 2D and 3D distributions are -0.76 and -0.88 Φ, respectively, both within very coarse sand (Fig. 16C). The mode of the 3D grain-size distribution, at -0.74 Φ, is within very coarse sand, while the mode of the 2D distribution, at -1.24 Φ, is within very fine pebbles (Fig. 16C). The 2D and 3D distributions are both moderately sorted (σ_1 = 0.82 ±0.02 Φ; Fig. 16D). Actual sediment grain sizes are distributed symmetrically with a skewness of -0.04, while the 2D distribution has a skewness of 0.16 and is classified as fine skewed (Fig. 16E). Grain-size distributions determined in 2D and 3D cannot be rejected by a two-sample K-S Test.

Sphericity measurements collected by image analysis are shown in two ways: all sphericities measured in 2D and only those measured from grain sizes <0.0 Φ ($2D_{<0\Phi}$; Fig. 16F). The purpose of the <0.0 Φ data set is to show 2D sphericities sampled in the same way as the 3D sediment, which does not include grains <0.0 Φ because they are too

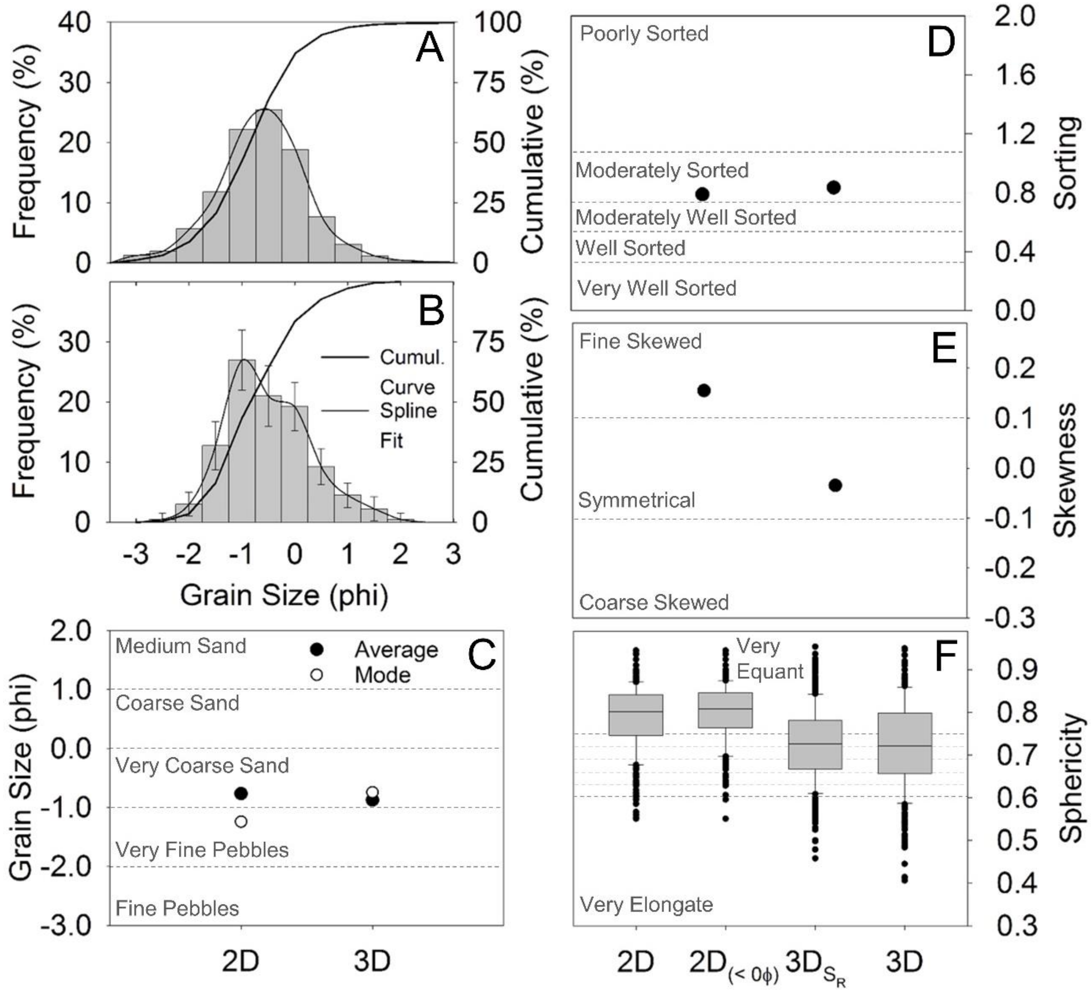

Figure 16: Comparison of textural parameters measured from the fluvial sediment using 2D and 3D methods of textural analysis. Histograms are fit with spline curves. Error bars show estimated error using the methods of Van der Plas and Tobi (1965). (A) Grain-size histograms and cumulative distributions determined by sieving of the 3D sediment. (B) Grain-size histograms and cumulative distributions determined by image analysis. (C) Grain size averages and modes for 2D and 3D analyses. (D) Sorting for 2D and 3D analysis. (E) Skewness for 2D and 3D analyses. (F) Distribution of grain sphericities showing the 90th, 75th, 50th, 25th, and 10th percentiles. $2D_{(< 0.0\Phi)}$ includes sphericity values for only grains with phi sizes less than 0.0 Φ and $3D_{S_R}$ is Riley Sphericity calculated using actual sediment long and intermediate axes. Dashed lines mark categorical descriptions of sphericity (Appendix D).

small to measure. However, truncating the data set appears to have no significant impact on the results. Both 2D populations have sphericity averages of 0.80 and sphericity ranges of approximately 0.52 to 0.94 (Fig. 16F).

Actual 3D grain diameters are used to calculate sphericity by two different methods: the 3D equation (ψ_p, Eq. 6) and the 2D equation (S_R, Eq. 5) using long and short grain axes ($3D_{S_R}$ in Fig. 16F). The purpose of calculating 2D S_R with actual grain dimensions is to test whether an equation accounting for only two grain axes can determine 3D sphericity when actual grain measurements are used. The 3D and $3D_{S_R}$ sphericities both have medians of 0.72, which is 0.08 lower than the medians of both 2D data sets, and a larger range, by about 0.1, than the 2D measured sphericities (Fig. 16F).

5.1.1.2 Interpretation

This present study shows for sediment with a grain-size range from medium pebbles to coarse silt, 2D textural image analysis can determine a range of grain sizes in frequencies that closely approximate those of the actual sediment (Fig. 16A, B). Image analysis also determined similar grain-size means within medium sand and moderate sorting. Slightly different modes and skewness, however, were calculated in 2D and 3D (Fig. 16C-E). The 0.5 phi shift in the mode of the 2D distribution is the likely cause of the change in skewness from 3D to 2D.

Discrepancies between the 2D and 3D data sets are relatively minor, which is further substantiated when error in 2D grain-size frequencies are considered. The 3D sediment distribution lies within, or just outside by 0.05%, of the statistical error based on the sample size of grains measured in the image (Van der Plas and Tobi, 1965). This indicates the 3D mode and skewness are within error of what can be determined by image analysis. It is important to consider error in frequency when comparing grain-size distributions and statistics, particularly where only a sample of the population is analyzed.

Sphericity of the fluvial sediment analyzed by image analysis is also observed to estimate actual grain properties reasonably well, but with slightly higher averages and a smaller spread of values concentrated more closely around the median (Fig. 16F). This is easily explained by grain orientation in an image, which is unlikely to permit measurement, or even identification, of actual axes because grains overlap, are buried, and foreshortened. Apparent long and short grain axes are measured smaller than actual, 3D grain axes, and are likely more proportional to each other, which causes 2D sphericity to be higher than in reality (Fig. 17). A check, however, can be performed to ensure that using a 2D equation for a 3D property is not causing the increase in 2D sphericity measurements.

Short and long 3D grain axes are used in the S_R equation ($3D_{S_R}$) to ensure the difference between the 2D and 3D data sets cannot be attributed to using a 2D equation for a 3D property. Results show 3D and $3D_{S_R}$ sphericities have the same median, 0.72, and similar ranges and spread of values, which demonstrates 2D calculations, using long and short grain dimensions, determine actual sediment sphericities very well (Fig. 16F). This suggests the limiting factor is not the use of only two dimensions, but the inability to

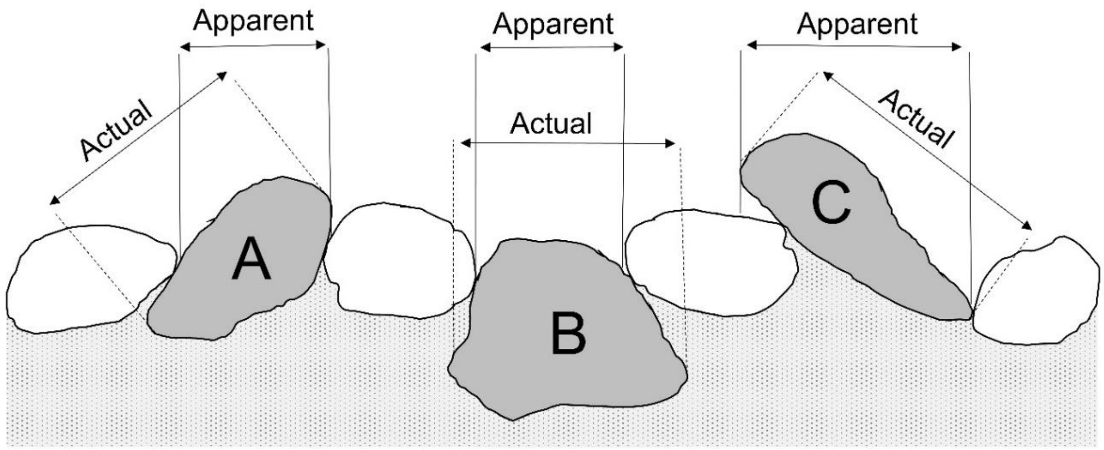

Figure 17: Examples of how actual axes of grains can be observed inaccurately when viewed in a 2D image taken perpendicular to the sediment surface. The apparent axes will appear shorter in length than actual grain dimensions. (A) Overlapping grains (B) Buried grain. (C) Foreshortened grain.

measure the appropriate axes (actual long and short axes) for accurate calculation of sphericity in 2D.

An empirical study by Bagheri et al. (2014) shows when D_i and D_c measurements are used to calculate sphericity by S_R, actual grain values will be overestimated by 0.1. This is consistent with the results of this study where the difference between 2D and 3D median sphericities is 0.08 (Fig. 16F). Because grain orientation is the determining factor of how a grain is measured in 2D, it is important to recognize that image analysis will have an improved accuracy (smaller overestimation) when grains are highly spherical relative to grains with very low sphericities as orientation does not change D_i and D_c measurements of grains with equal axes (Bagheri et al., 2014). Although, grain overlap, burial, and foreshortening has an effect on sphericity measurements, it does not affect grain size, which is observed to have similar properties to the 3D sediment.

5.1.2 Roundness

5.1.2.1 Description

Grain roundness determined from the 3D sediment and the 2D, high-resolution, evenly illuminated image are compared to determine how well roundness of a coarse sand fluvial sediment can be estimated from images. Grain roundness assessed from each the 2D and 3D data sets span similar ranges, from very angular to well rounded in 2D and angular to well rounded in 3D (Fig. 18). Both distributions have a mode at subrounded that accounts for the roundness of nearly half the sediment, approximately 53% of the grains analyzed in 2D and 45% of those in 3D. Subangular grains identified in the image are about 20% fewer in imaged sediment than in the 3D sediment, but this does not

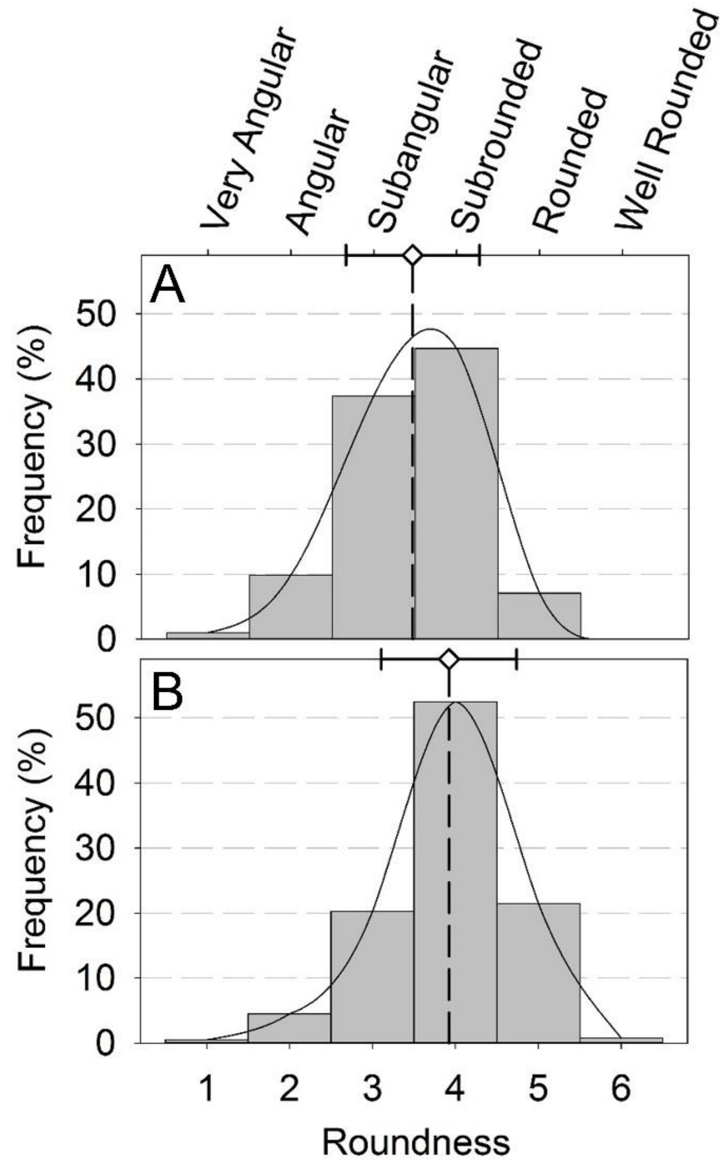

Figure 18: Fluvial sediment roundness histograms constructed from 2D and 3D analyses. Histograms are fit with spline curves. Diamond with vertical dashed line represents average roundness and bars equal one standard deviation. (A) Roundness histogram determined from microscope analysis of actual sediment. (B) Roundness histogram determined from image analysis.

heavily influence the average, which is 3.92 for the image analysis and 3.50 for the actual sediment. Roundness values of the actual sediment are skewed toward angular grains, which is also reflected in the data collected from the image.

5.1.2.2 Interpretation

The 2D and 3D roundness histograms have similar averages, standard deviations, and ranges, suggesting data collected by 2D and 3D methods can determine statistically similar results (Fig. 18). Because of these similarities, and the high proportions of subangular grains measured in both 2D and 3D, image analysis is determined to produce appropriate results for interpreting the abrasion history of a coarse sand fluvial sediment. Paralleling what was found for the aeolian sediment, high resolution images, comparable to the maximum resolution of MAHLI, are able to define general roundness characteristics for sandy fluvial sediment.

5.2 Comparison of Different Image Resolution

5.2.1 Grain Size and Sphericity

5.2.1.1 Description

To establish the effect of image resolution on grain-size analysis, the fluvial sediment grain-size distribution, grain-size statistics, and sphericity determined from the high-resolution (19 μm/pixel), evenly illuminated image are compared to analyses of the same image degraded to 40, 60, 80 and 100 μm/pixel (Fig. 19). At all image resolutions, grain-size distributions start at -2.5 Φ and end at 1.5 ± 0.5 Φ (very fine pebbles to fine sand; Fig. 19A-E). Average grain size is found to be within very coarse sand, regardless of image resolution (Fig. 19F). Each distribution has a mode in very fine pebbles

Figure 19: Comparisons of textural parameters measured from the fluvial sediment at different resolutions. Histograms are fit with spline curves. Modes of bimodal distributions are labelled. Error bars show estimated error using the methods of Van der Plas and Tobi (1965). (A) 19 μm/pixel image grain-size distribution. (B) 40 μm/pixel image grain-size distribution. (C) 60 μm/pixel image grain-size distribution. (D) 80 μm/pixel grain-size distribution. (E) 100 μm/pixel image grain-size distribution. (F) Grain size average and mode at all image resolutions. (G) Sorting at all image resolutions. (H) Skewness at all image resolutions. (I) Distribution of grain sphericities from different resolution images showing the 90th, 75th, 50th, 25th, and 10th percentiles. Dashed lines mark categorical descriptions of sphericity (Appendix E).

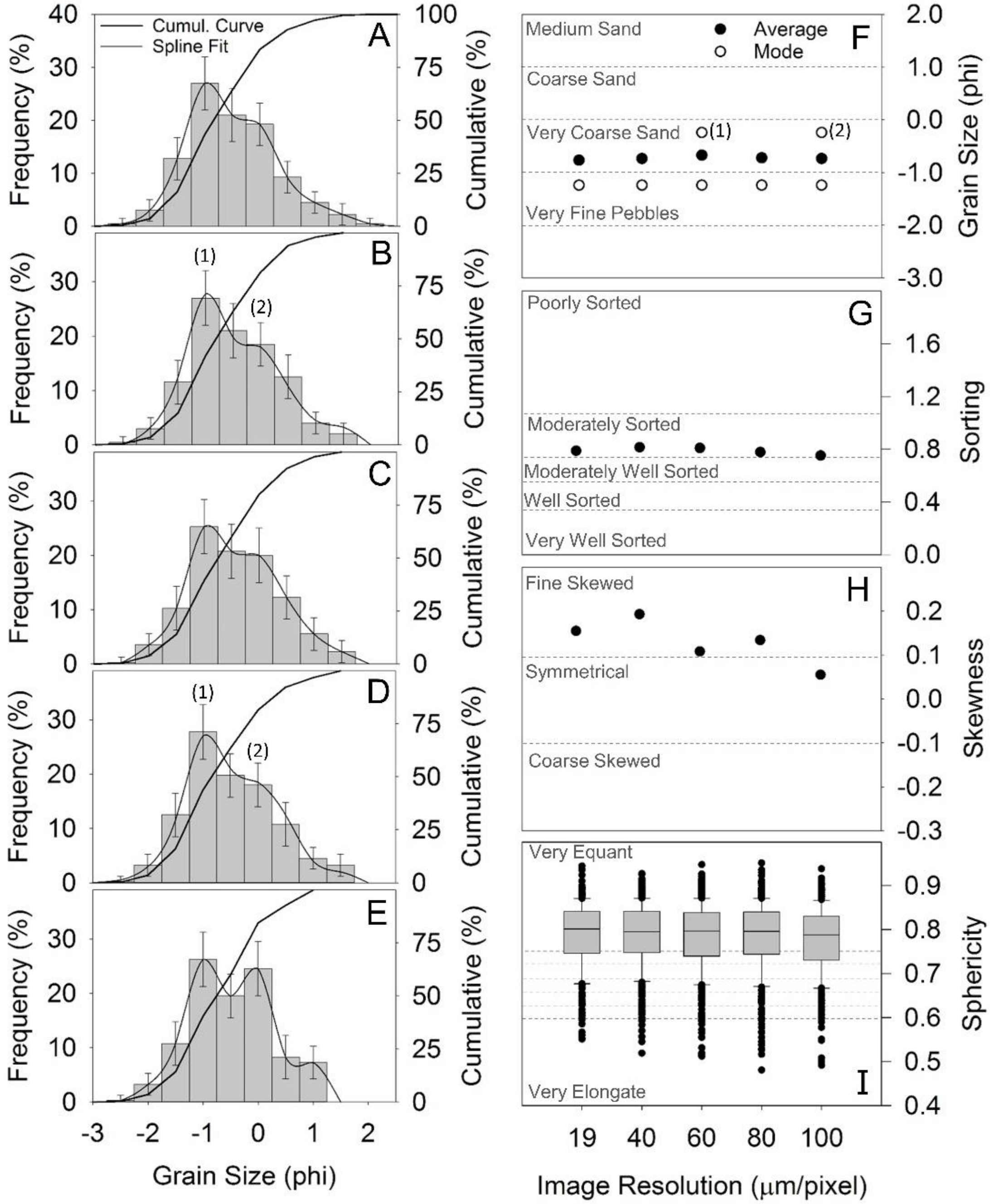

Figure 19: Continued.

(Mo = 1.24 Φ) and a shoulder at 0.0 Φ, which is large enough at some resolutions, 60 and 100 µm/pixel, to be classified as a second mode in very coarse sand (Fig. 19A-E). This mode in the 60 µm/pixel image has a frequency of 20%, while the 19, 20, 40, and 80 µm/pixel images have frequencies only 2% lower at 0.0 Φ and are unimodal (Fig. 19F). Contrasting the second mode determined from the 60 µm/pixel image, the very coarse sand mode identified at 100 µm/pixel is approximately 5% higher than in the 19 to 80 µm/pixel images (Fig. 19A-E). Sorting, however, is moderate in all images analyzed (σ_1 = 0.78 ±0.03; Fig. 19F).

Though the 100 µm/pixel image distribution is classified as fine skewed, calculated skewness values from all images lie near the boundary of fine skewed and symmetrical (Fig. 19H). The 5% increase at the 0.0 Φ mode in the 100 µm/pixel image is small, but significant enough to influence the skewness of the distribution making it symmetrical (Sk_i = 0.06), rather than fine-skewed similar to the higher-resolution images (Sk_i = 0.15 ±0.05; Fig. 17H). Sphericity measured at each image resolution was reproduced almost identically (Fig. 19I). Similar medians of 0.80 ± 0.01, and interquartile ranges of 0.09 ±0.01 were also determined from each image (Fig. 19I). The total range of values also strongly overlap between approximately 0.50 and 0.95 (Fig. 19I).

5.2.1.2 Interpretation

Grain-size analysis of the fluvial sediment images at different resolutions shows, for a medium pebble to coarse silt sediment, image analyses performed at 40, 60, and 80 µm/pixel can reproduce the grain-size distributions measured from the high-resolution, 19 µm/pixel image very well (Fig. 19A-D). In addition to the excellent reproduction of grain-size frequencies, the grain size range differs by only 0.5 Φ from 19-to-80 µm/pixel

(Fig. 19A-D). Strong similarities between the grain-size distributions measured from images of different resolution have resulted in grain-size averages that, regardless of image resolution, are in very coarse sand. Furthermore, from 19-to-100 μm/pixel the sediment was determined to be moderately sorted.

There is a difference in modality between the 60 μm/pixel image (bimodal) and the 19, 40, and 80 μm/pixel images (unimodal; Fig. 15A-E). However, the difference in frequencies between the 19 and 80 μm/pixel images at the 0.0 Φ bins, where this mode lies, is less than 2%. These results suggest the grain-size distributions determined from the 19-to-80 μm/pixel images all have frequencies at 0.0 Φ that are near, or just above, the threshold for qualifying as a second mode. Thus, the bimodality of the 60 μm/pixel image should not be considered a product of decreased image resolution, but an artifact of a small fluctuation in the frequency of grains that happened to satisfy bimodal criteria. Bimodality observed in the 100 μm/pixel image, however, is more exaggerated than in the 19-to-80 μm/pixel images, and may be a product of low resolution. For a medium pebble to coarse silt sediment, resolutions higher than 80 μm/pixel have the greatest capacity to determine grain-size distributions and statistics, while at 100 μm/pixel the distribution may be less reliable, but descriptive statistics can still be reasonably calculated.

Many similarities are observed between the sphericity values measured at each image resolution. Sphericity measured at all resolutions has a range, interquartile range, and median in the same descriptive category. Even sphericity measurements made at 100 μm/pixel exhibit minimal differences from those measured at high resolution. For a sediment with a wide range of sphericity (~0.4 to 1.0) and a median of approximately 0.8, image resolution has a negligible effect on the measurement of grain sphericity to 100 µm/pixel (Fig. 19I).

5.2.2 Roundness

5.2.2.1 Description

To establish the effect of image resolution on the estimation of roundness in 2D, roundness of the fluvial sediment determined from the evenly illuminated, 19 µm/pixel image is compared to roundness determined from the same image degraded to 40, 60, 80 and 100 µm/pixel. Histograms of roundness values, estimated from all image resolutions, have modes and averages (ρ = 3.77 ±0.23) at subrounded and range from very angular or angular to well rounded. Standard deviations range from 0.70 to 0.96. Frequencies of subrounded grains in the 19 to 60 µm/pixel images are between 50 to 60% (Fig. 20). When resolution is decreased to 80 µm/pixel, roundness values are distributed more evenly and a decrease of about ~20% at the mode results in a small increase in each of the other roundness categories (Fig. 20D). The frequency of subangular grains rises from to 18% at 60 µm/pixel to 26.2% at 80 µm/pixel, and continues to increase at 100 µm/pixel to 36.75% (Fig. 20C-E). At the lowest resolution subangular and subrounded grains are in near equal proportions, 36.75% and 42.75%, which contrasts findings at high resolution, where there are about ~30% more subrounded than subangular grains (Fig. 20).

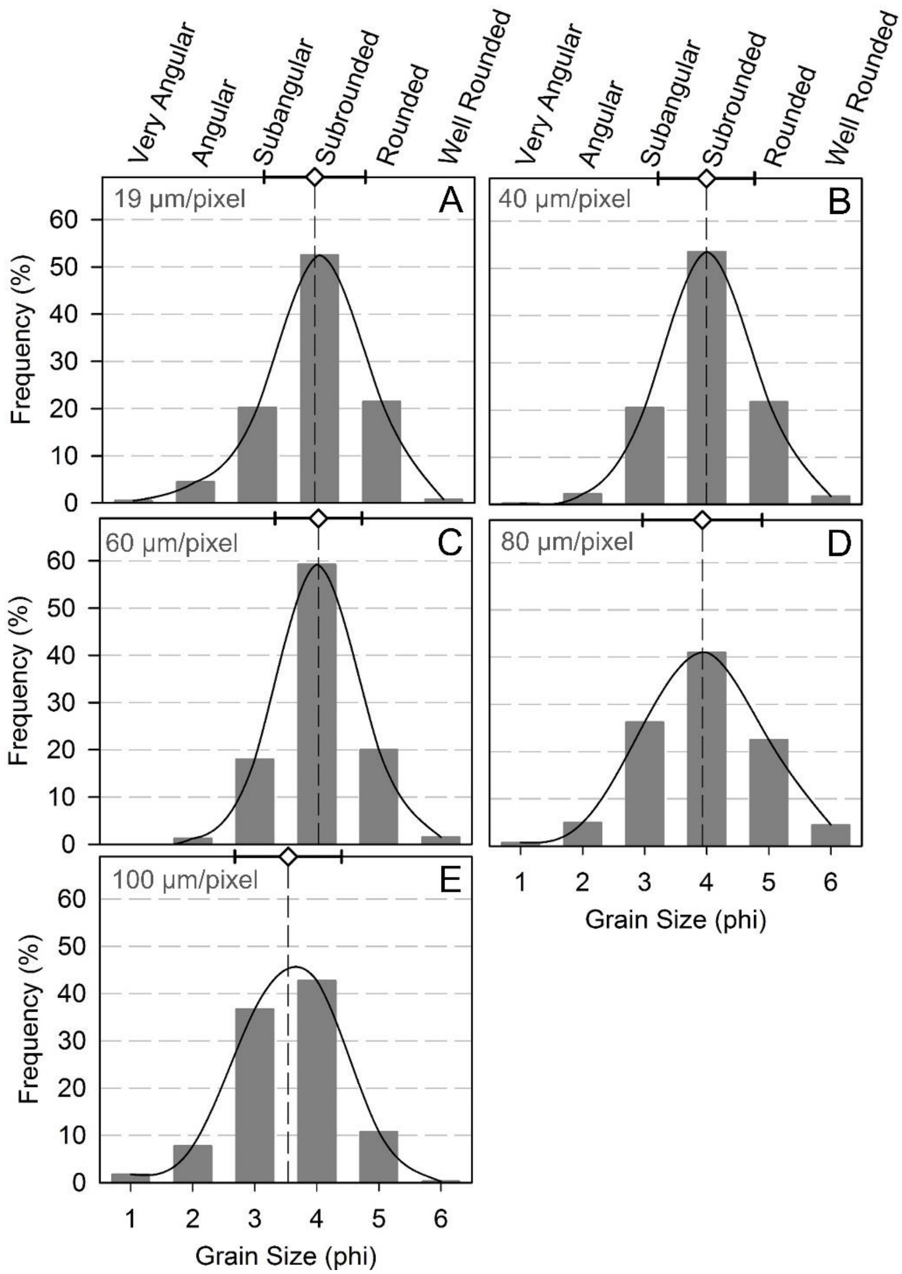

Figure 20: Fluvial sediment roundness histograms constructed from images of different resolutions. Histograms are fit with spline curves. Diamonds and dashed vertical lines show average roundness. Bars are one standard deviation. (A) 19 µm/pixel image roundness histogram. (B) 40 µm/pixel image roundness histogram. (C) 60 µm/pixel image roundness histogram. (D) 80 µm/pixel image roundness histogram. (E) 100 µm/pixel image roundness histogram.

5.2.2.2 Interpretation

For the fluvial sediment in this study, similar ranges, averages, and standard deviations were identified at all image resolutions. Histograms of roundness values estimated from the 19 to 60 μm/pixel images are highly similar in frequency, differing by less than 7%. At 80 and 100 μm/pixel, however, histograms of roundness are more symmetrical with higher proportions of subangular grains (Fig. 20D, E). This is consistent with what was observed in the aeolian sediment and likely arises for the same reason. At low resolutions, grains appear more angular as their edges are pixelated. Roundness estimates are most affected at 80 μm/pixel, though similar ranges, modes, averages and standard deviations suggest that 2D estimates of roundness, even to 100 μm/pixel can determine roundness characteristics of sediment.

5.3 Summary: Textural Analysis of Fluvial Sediment

Fluvial sediment collected near Death Valley was studied in two ways. First, grain-size measurements and estimations of roundness from the 3D sediment and the evenly illuminated, high-resolution image were compared. Results show the grain-size range, average, and sorting measured in 2D accurately describe these properties of the 3D sediment. The mode of the 2D distribution, however, is shifted slightly coarser causing the 2D distribution to be fine skewed while the 3D sediment distribution is symmetrical. Analyses of roundness showed the range, average, and standard deviation of roundness estimated from the fluvial sediment can also be accurately determined from 2D images. Sphericity measured in 2D was observed to overestimate 3D sediment sphericity by approximately 0.1, which likely results from grain overlap, burial, or foreshortening.

With strong accuracy obtained from the textural analysis of the high-resolution image, a second analysis comparing grain-size, sphericity, and roundness from the high-resolution image (19 μm/pixel) and the same analyses at 40, 60, 80, and 100 μm/pixel was performed. The grain-size range, mean, and sorting were accurately determined at all image resolutions and strong similarities, including a shoulder in the distribution at 0.0 Φ, exist between the grain-size distributions determined form the 19 to 80 μm/pixel. At 100 μm/pixel, the shoulder at 0.0 Φ is more exaggerated which alters the skewness of the distribution. Estimates of grain roundness determined the range, average, mode, and standard deviation were similar across all image resolutions. Roundness analysis at 80 and 100 μm/pixel, however, identified a broader range of roundness than in the 11 to 60 μm/pixel images. Sphericity measurements in 2D show negligible change when analyzed from 19 to 100 μm/pixel.

No Strong relationships were identified between textural parameters analyzed from the 2D and 3D fluvial sediment (Appendix I), with statistics summarized in Appendix K. All raw data collected from the 2D and 3D aeolian sediment in the above two analyses can be located in the attached Excel file.

6. APPLICATIONS

6.1 Relationship between Resolution and Minimum Grain Size

To fully characterize the grain size-range of sediment, image resolution must resolve the smallest sediment component. By knowing both the minimum number of pixels needed to define a grain and the resolution at which sediment is imaged, the diameter of the smallest resolvable grain can be calculated. For the present study, at least 3 pixels were required to define a grain (Fig. 21A). This is shown in the grain-size analysis of the aeolian sediment, where a minimum grain size of 3 pixels is consistently recognized as resolution is decreased to 30, 40, and 50 μm/pixel (Fig. 21A). These results suggest the finest grain measurement made at each of these image resolutions was a function of insufficient resolution rather than the smallest grain available for measurement within the actual sediment. Thus, for the aeolian sediment, image resolutions of 30, 40, and 50 μm/pixel are insufficient to resolve grains smaller than 2.73 Φ, 3.06 Φ, and 3.47 Φ, respectively (Fig. 21A).

Analyses of the 20 and 11 μm/pixel aeolian sediment images, however, did not include measurements of grains defined by 3 pixels. Grain-size analysis determined a minimum of 5 pixels at 20 μm/pixel and 9 pixels at 11 μm/pixel (Fig. 21A). At both image resolutions, 3.3 Φ (very fine sand) was the minimum grain size measured. The actual aeolian sediment contains grains as small as 4.0 Φ (very fine sand) and because this work shows grains can be defined by as few as 3 pixels, it is theoretically possible for image analyses to measure 4.0 Φ at 20 μm/pixel (very fine sand) and 4.9 Φ at 11 μm/pixel (very coarse silt). Grains not measured below 3.3 Φ in the 11 and 20 μm/pixel,

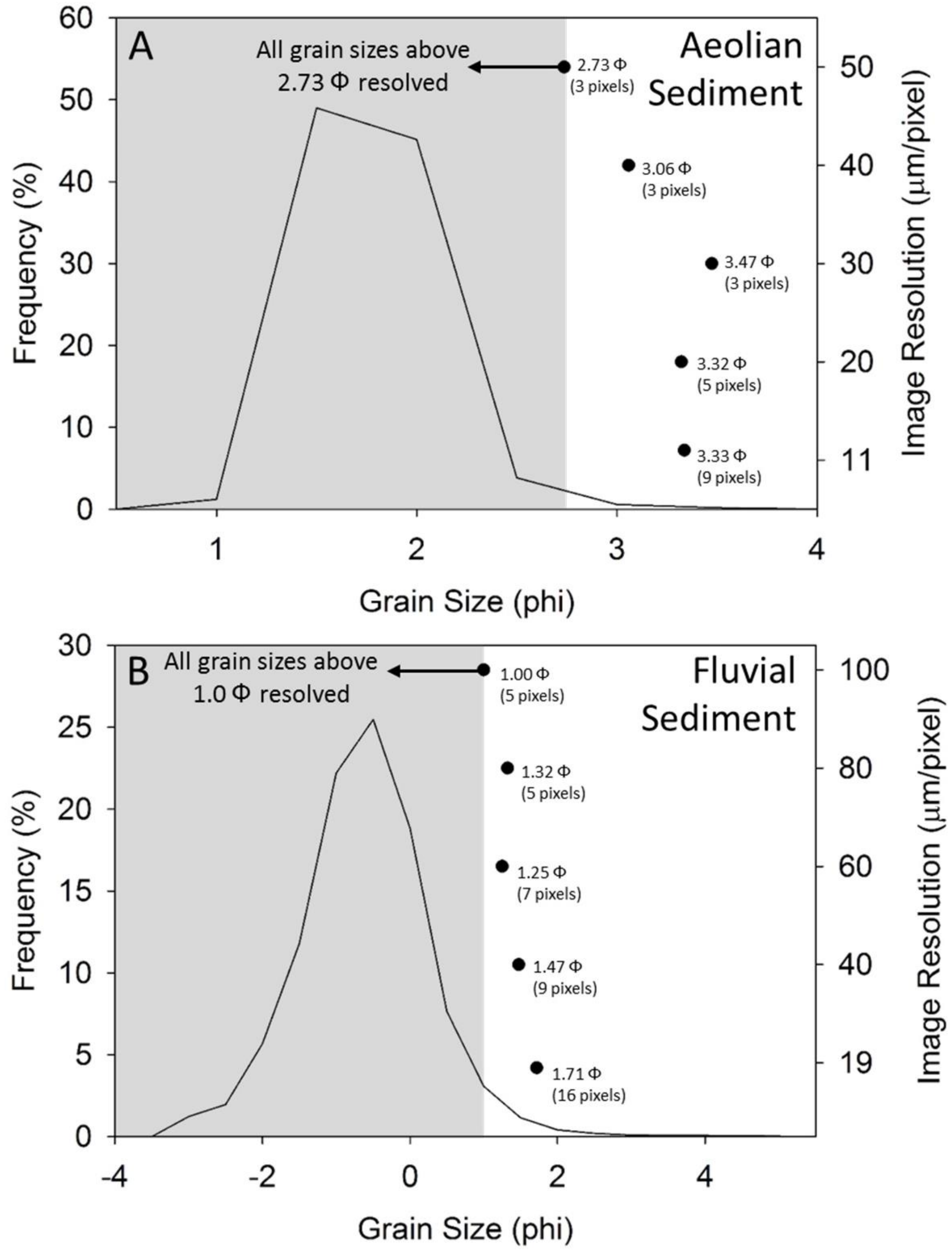

Figure 21: Relationship between the minimum measured grain size and image resolution for the aeolian and fluvial sediments. Grain-size distribution is shown as solid line. Points are minimum grain size measured at each image resolution analyzed. Grey box shades grain sizes that were resolved at all resolutions (A) Relationship between the minimum measured grain size and image resolution for the aeolian sediment. (B) Relationship between the minimum measured grain size and image resolution for the fluvial sediment.

suggests these grain sizes are in frequencies too low to sample by the grid method used in this work. Therefore, two factors have contributed to the minimum grain size that is measured in an image: resolution and frequencies of grain sizes. In the fluvial sediment, image resolution does not appear to have impacted the minimum grain size that was measured, as grains were described by at least 5 pixels (Fig. 21B). Low frequencies below 2 Φ are likely the limiting factor to the minimum grain size that was measured.

6.2 Number of Grains Needed to Define a Grain-Size Distribution

According to Van der Plas and Tobi (1965), a point count of 400 grains will yield a grain-size distribution that is within 5% of the actual grain-size distribution of the seidment. To ensure grain-size distributions were described as accurately as possible, 400 grains were measured in each image analyzed in this work. The necessity of this large sample size to characterize grain-size distribution of moderate to well sorted sediment is unclear. When a grain size is frequent, the probability of that size being included in a sample is high. Thus, better sorted sediments should require lower point counts than poorly sorted sediment to fully describe their distributions. To determine if sample sizes lower than 400 grains can characterize grain-size distributions of aeolian and fluvial sediments studied here, cumulative grain-size distributions were constructed from sample sizes of 100, 150, 200, 250, 300, 350, and 400 randomly collected grains and compared (Fig. 22).

In the fluvial sediment images, samples sizes of 150 and 100 produce slight changes in frequency at -1.5 Φ and 0.0 Φ (Fig. 22A). At all sample sizes the sediment is

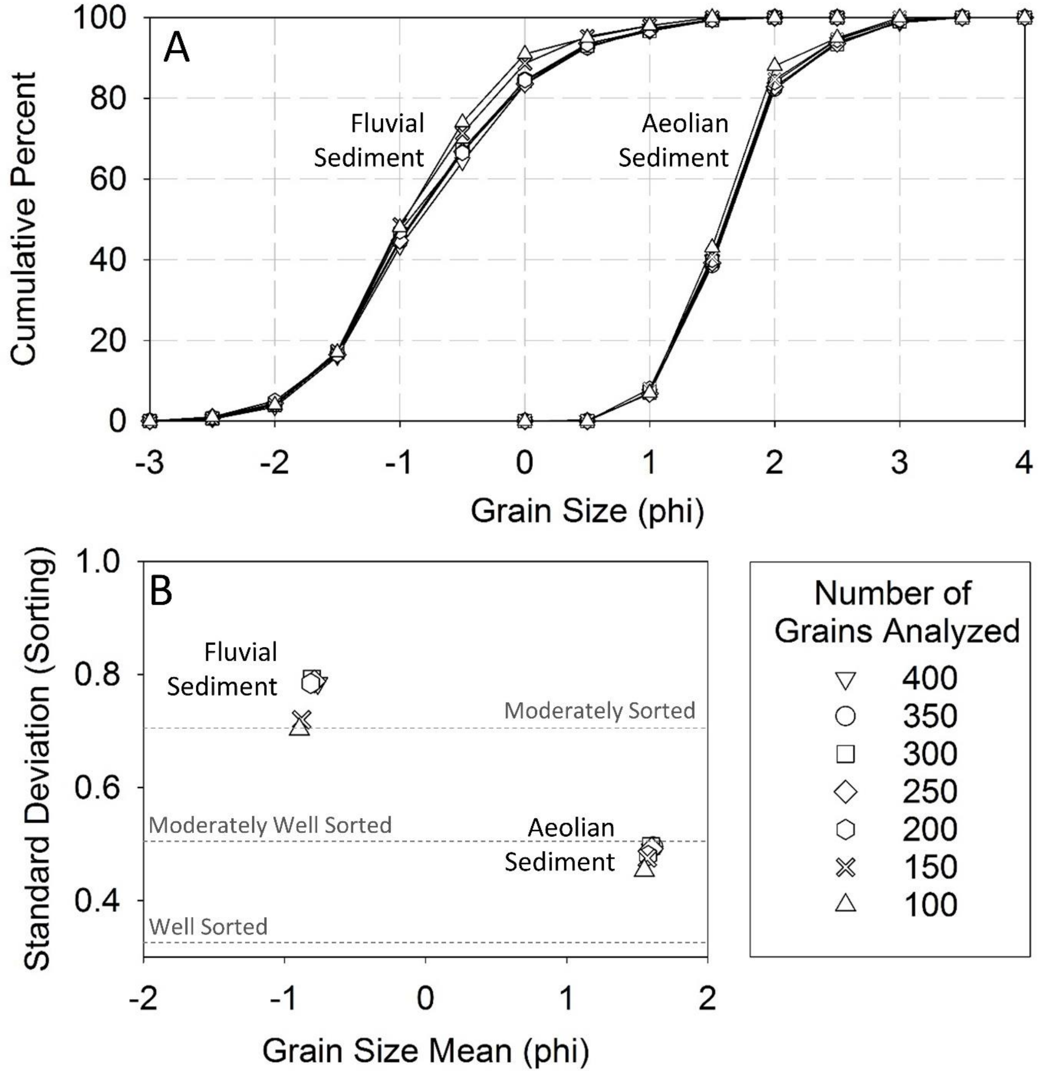

Figure 22: Results from study to determine if grain sample sizes less than 400 could be used to describe the aeolian and fluvial grain size distributions. (A) Aeolian and fluvial sediment cumulative grain-size distributions constructed using the different sample sizes. (B) Plot showing the grain-size mean and sorting of the aeolian and fluvial sediments calculated from cumulative distributions of different sample sizes.

moderately sorted with a mean in very coarse sand, although, the mean and standard deviation show a divergence from the values obtained at higher grain counts (Fig. 22B). As a better sorted sediment, changes in the grain-size distribution, mean, and standard deviation, are less apparent (Fig. 22). At all sample sizes, the aeolian sediment is well sorted and has a mean within medium sand. These results suggest grain-size distributions of moderately to well sorted sediment can be similarly described by as few as 100 grains or as many as 400 grains. Larger scatter of the mean and standard deviation in the fluvial sediment and changes in distribution frequencies, however, suggests poorer sorting will require the number of grains sampled to increase.

6.2 Applications to Terrestrial Image Analyses

As a Mars-analog study, this work has focused on understanding textural image analysis using sediments of dominantly basaltic composition. The use of basaltic sediments ensures results are relevant to image analyses of martian sediments and their application to Mars studies is not affected by differences in composition. It is conceivable, however, that the results of this study could also apply to terrestrial image analyses of dominantly granitic sediments. Although basaltic in composition, the textures of the aeolian and fluvial sediments used in this study are comparable to textures of other sediments types from like environments.

Dune fields, including those on different continents, have been shown to have similar grain size properties, typically within the range of coarse to fine sand, and are moderate to very well sorted and generally rounded (Lancaster, 1992; Khalah, 1989; Folk, 1971). These properties correspond with the very well sorted, medium sand from the Moses Lake Dunes analyzed in this work. Fluvial systems typically have more complex sediment textures and can transport sediment with a range of grain sizes. Roundness and sphericity are also likely to vary between fluvial systems of different types and are also dependent on sediment input and transport distance (McBride, 1987; Folk, 1957). The coarse sand, moderately sorted, fluvial sediment used in this study is within the range of textures that are typically found in fluvial systems. Because these sediments possess textural properties that are characteristic of the environments from which they were sampled, applications of this work to terrestrial sediments is not likely to be greatly affected by differences in composition.

7. SUMMARY AND CONCLUSIONS

Determining sedimentary textures of basaltic sediments from Mars-analog environments in 2D images and 3D, actual sediments has provided insight into the accuracy at which grain-size, sphericity, and roundness can be described from images. Investigations into the role of image resolution and shadows has demonstrated textural analyses can be performed at a range of conditions. This work has also clarified methods related to the collection of textural data from images and the comparison of 2D and 3D data sets.

Single- and dual-user 2D grain size measurements made on images of basaltic impact-proxy sediment show D_i and D_c measurements can be repeated and reproduced with high levels of agreement. Comparisons of images that have been digitally resampled from high to low resolutions with those taken natively at low resolutions by the camera show a strong similarity making it highly unlikely that grain measurements would differ between the two images. An analysis of aeolian and fluvial sediment grain-size distributions constructed using the D_i and D_c dimensions confirmed the D_i measurement produced a grain-size distribution that more closely approximates the sieve distributions than the D_c measurements. A conversion was applied to the 2D distribution in an attempt to further improve its estimate of the sieve distribution, but the conversion had little effect on the distributions and did not improve the 2D approximation of the 3D data.

Aeolian sediment 2D and 3D analyses show similar grain-size ranges, sorting, skewness, averages, and modes. Grain-size analysis performed at lower-resolution suggests 20 μm/pixel resolution or better will yield most accurate results, but at 50 μm/pixel statistics can be reasonably determined. Image resolution has little effect on sphericity measurements. Shadows had minimal effect on the analysis of grain size and sphericity, and a minor effect on the estimation of roundness at high incident solar angles. Average roundness determined in 2D is nearly identical to the average determined in 3D. Distribution of roundness values becomes more evenly distributed at 30 μm/pixel image resolution, but similar average and standard deviations can be determined to 50 μm/pixel.

Comparison of the fluvial sediment grain-size distributions from 2D and 3D show similar grain-size ranges, sorting, skewness, averages, and modes. Resolution begins to influence the grain-size distribution, modality, and skewness, at 100 μm/pixel, indicating resolutions higher than 80 μm/pixel are most useful for determining actual sediment characteristics. Sphericity is not affected by image resolution, but measurements performed in 2D were found to have slightly higher averages than those in 3D. Roundness values estimated from images correctly described the sediment's actual roundness and can be precisely determined to 40 μm/pixel. However, at 60, 80, and 100 μm/pixel similar roundness modes, averages, and ranges were still obtained.

Overall, the results of this study show images are useful mediums from which sediment textures can be collected and interpreted. This work shows high-resolution images are not necessary for reasonable assessments of sediment properties and shadows have a negligible result on the image analysis of sediment. Results imply analyses of sediments on Mars can be performed under a variety of resolution and illumination conditions while providing accurate information for the interpretation of martian surface processes.

LIST OF REFERENCES

Bagheri, G. H., Bonadonna, C., Manzella I., and Vonlanthen, P. (2015), On the characterization of size and shape of irregular particles, *Powder Technol.*, *270*, 141-153, doi: 10.1016/j.powtec.2014.10.015.

Bandfield, J. L., Edgett, K. S., and Christensen, P. R. (2002), Spectroscopic study of the Moses Lake dune field, Washinton: Determination of compositional distributions and source lithologies, *J. Geophys. Res*., *107*(E11), 5092, doi: 10.1029/2000JE00146.

Barry, T. L., Kelley, S. P., Reidel, S. P., Camp, V. E., Self, S., Jarboe, N. A., Duncan, R. A., and Renne, P. R. (2013), Eruption chronology of the Columbia River Basalt Group, in Reidel, S. P., Camp, V. E., Ross, M. E., Wolff, J. A., Martin, B. S., Tolan, T. L., and Wells, R. E., eds., The Columbia River Flood Basalt Province: Geological Society of America Special Paper 497, p. 45–66, doi:10.1130/2013.2497(02)

Bell, J. F. et al, (2003), Mars Exploration Rover Athena Panoramic Camera (PanCam) investigation, *J. Geophys. Res.*, *108*(E12), 8063, doi:10.1029/2003JE002070.

Bertram, A., (2016), The effects of shadow presence in image analysis pertaining to textural sedimentary research on Mars, B.S. Thesis, Dept. of Earth and Planet. Sci., Univ. of Tenn., Knoxville, Tennessee.

Blake, D. F. (2013), Curiosity at Gale Crater, Mars: Characterization and analysis of the Rocknest Sand Shadow, *Science*, *341*, doi: 10.1126/science.1239505.

Blott, S. J., and Pye, K. P. (2001), GRADISTAT: A grain-size distribution and statistics package for the analysis of unconsolidated sediments, *Earth Surf. Process. Landforms*, *26*, 1237-1248, doi: 10.1002/esp.261.

Boggs, S. (2006), Principles of Sedimentology and Stratigraphy, 4th ed., 662 pp., Pearson Prentice Hall, University of California.

Bretz, J. H. (1923), The Channelized Scablands of the Columbia Plateau, *J. Geol.*, *31*, 617-649.

Buscombe, D. (2008), Estimation of grain-size distributions and associated parameters from digital images of sediment, *Sediment. Geol.*, *210*, 1-10.

Butler, J. B., Lane, S. N., and Chandler, J. H. (2001), Automated extraction of grain-size data from gravel surfaces using digital image processing, *J. Hydrol. Res.*, *39*, 519-529, doi: 10.1080/00221686.2001.9628276.

Cabrol, N. A., et al. (2008), Sedimentology at Gusev Crater from Columbia Memorial Station to Winter Haven, J. Geophys. Res., 113, E06S05, doi: 10.1029/2007JE002953.

Carbol, N. A., et al. (2014), Sands at Gusev Crater, *J. Geophys. Res., 119*, 941-967, doi: 10.1002/2013JE00453.

Cornwall. C., Bandfield, J. L., Titus, T. N., Schreiber, B. C., and Montgomery, D. R. (2015), Physical abrasion of mafic minerals and basalt grains: Application to martian aeolian deposits, *Icarus*, *256*, 13-21, doi: 10.1016/j.icarus.2015.04.020.

Cox, N. J., (2006), Assessing agreement of measurements and predictions in geomorphology, *Geomorph*., *76*, 332-346, doi: 10.1016/j.geomorph.2005.12.001.

Crisp J. A. et al. (2003), Mars Exploration Rover mission, *J. Geophys. Res*., *108*(E12), 8016, doi: 10.1029/2002JE002038.

Dobkins, J. E., and Folk. R. L., (1970), Shape development on Tahiti-Nui, *J. Sediment. Petrol., 40*, 116-1203

Edgett, K. S., and Lancaster, N. (1993), Volcaniclastic aeolian dunes: terrestrial examples and applications to martian sands, *J. Arid Env.*, *25*, 271-297, doi:10.1006/jare.1993.106.

Edgett, K. S. et al. (2012), Curiosity's Mars Hand Lens Imager (MAHLI) investigation, *Space Sci. Rev., 170*, 259-317, doi: 10.1007/s11214-012-9910-4.

Eibl, M. A., Fedo, C. M., Friday, M. E., and McSween, H. Y. (2015), The accuracy of 2D rover imagery for representing 3D sedimentary textures of basaltic Mars-analog sediment, presented at The Lunar and Planetary Science Conference, The Woodlands, TX.

Fedo, C. M., McGlynn, I. O., and McSween, H. Y. (2015), Grain size and hydrodynamic sorting controls on the composition of basaltic sediments: Implications for interpreting martian soils, *Earth Planet. Sci. Lett., 423*, 67-77, doi: 10.1016/j.epsl.2015.03.052.

Fedo, C. M., Eibl, M. A., McGlynn, I. O., and McSween, H. Y. (2016), Textural and compositional analysis of terrestrial sediments: Toward a better understanding of martian sediments and sedimentary rocks, pending presentation at the Geological Society of America Conference, Denver, CO.

Folk, R. L. (1951), Stages of textural maturity in sedimentary rocks, *J. Sediment. Petrol., 21*, 127-130.

Folk, R. L., and Ward, W. C. (1957), Brazos River Bar: A study in the significance of grain-size parameters, *J. Sed. Pet., 27,* 3-26.

Folk, R. L. (1971), Longitudinal Dunes of the northwestern edge of the Simpson Desert, Northern Territory, Australia, 1. Geomorphology and Grain Size Relationships, *Sediment., 16*, 5-54

Folk, R. L. (1980), *Petrology of Sedimentary Rocks*, 2nd ed., 182 pp., Hemphill, Austin, Tex.

Gabler, R. E., Petersen, J. F., Trapasso, and Stack, D. (2008), Physical Geography, Cengage Learning, 672 pp.

Grotzinger, J. P. et al., (2012) Mars Science Laboratory mission and science investigation, *Space Sci. Rev*., *170,* 5-56, doi: 10.1007/s11214-012-9892-2.

Heilbronner, R. and Barrett, S. (2014), Image analysis in Earth sciences, 520 pp., Springer Berlin Heidelberg.

Herkenhoff, K. E., et al. (2003), Athena Microscopic Imager investigation, *J. Geophys. Res.*, *108*(E12), 8065, doi:10.1029/2003JE002076.

Howard, J. L. (1993), The statistics of counting clasts in rudites: A review, with examples from the upper palaeogene of Southern California, *Sediment.*, *40*, 157-174.

Janoo, V. C., (1998), Qantification of shape, angularity, and surface texture of base course materials, U.S. Army Corps of Engineers, Cold Regions Research and Envine Laboratory, *Special Report 98-1*.

Jerlmack, D. J., Mohrig, D., Grotzinger, J. P., Fike, D. A., and Watters, W. A. (2006), Spatial grain size sorting in eolian ripples and estimation of wind conditions on planetary surfaces: Application to Meridiani Planum, Mars, *J. Geophys. Res.*, *11*(E12S02), doi: 10.1029/2005JE00254.

Kellerhals, R., and Bray, D. (1971), Sampling procedures for coarse fluvial sediments, *Proc. of the Am. Soc, of Civil Eng., 97,* 1165-1180.

Khalaf, F. (1989), Textural characteristics and genesis of the aeolian sediments in the Kuwaiti Desert, *Sediment., 36*, 253-271.

Kleinhans, M. G. (2005), Grain-size sorting in grainflows at the lee side of deltas, *Sediment.*, *52*, 291-311, doi: 10.1111/j.1365-3091.2005.00698.x.

Knauth, L. P., Burt, D. M, and Wohletz, K. H. (2005), Impact origin of sediments at the Opportunity landing site on Mars, *Nature*, *438,* doi: 10.1038/nature04383.

Kok, J. F. (2010), Difference in the wind speeds required for initiation versus continuation of sand transport on Mars: Implications for dunes and dust storms, *Phys. Rev. Lett., 104*.

Krumbein, W. C. (1938), Size frequency distribution of sediments and the normal phi curve, *J. Sediment. Petrol.*, *8*, 84-90.

Krumbein, W.C. (1941), Measurement and geological significance of shape and roundness of sedimentary particles, *J. Sediment. Petrol.*, *11*, 64-72.

Kuenen, Ph. H. (1960), Experimental abrasion 4: Eolian action, *J. of Geol*., *68*, 472-449.

Laity, J. (2008), Deserts and Desert Environments, 306 pp., John Wiley and Sons, West Sussex, UK.

Lancaster, N. (1981), Grain Size Characteristics of Namib Desert Linear Dunes, *Sediment., 28*, 115-112.

Leovy, C., (2001), Weather and Climate on Mars, *Nature*, 412, 245-249, doi: 10.1038/35084192.

Lillesand, T. M., (2008), Remote sensing and image interpretation, 7th Ed., 768 pp., Wiley Global Education.

Lin, L., (1989), A Concordance Correlation Coefficient to Evaluate Reproducibility, *Biometrics*, *45*, 255-268.

Malin, M. C., et al. (2010), The Mars Science Laboratory (MSL) Mast-Mounted Cameras (Mastcams) Flight Instruments, presented at the Lunar and Planetary Science Conference, The Woodlands, TX.

McBride, E. F., and Picard, M. D. (1987), Downstrean changes in sand composition, roundness, and gravel size in short-headed, high-gradient stream, Northwest Italy, *J. Sediment. Petrol*, *57*, 1018-1026.

McEwan, I. K., Sheen, T. M., Cunningham, G. J., and Allen, A. R. (2001), Estimating the size composition of sediment surfaces through image analysis, *Proc. Inst. Civil Eng.: Water, Mar. Energy*, *142*, 189–195.

McGlynn, I. O., Fedo, C. M., and McSween, H. Y. (2011), Origin of basaltic soils at Gusev Crater, Mars, by aeolian modification of impact-generated sediment, *J. Geophys. Res.*, *116*, E00F22, doi: 10.1029/2010JE003712.

McKee, E. D. (1979), A study of global sand seas, U.S. Geological Survey, Professional Paper 1052, U.S. Government Printing Office.

Miller, G. M., and Wright, L. A. (2002), Geology of Death Valley National Park, 72 pp. Kendal Hunt, United States.

Minitti, M. E., et al. (2013), MAHLI at the Rocknest sand shadow: Science and science-enabling activities, *J. Geophys. Res.*, *118*, 1-23, doi: 10.1002/2013JE00442.

Powers, M.C. (1953), A new roundness scale for sedimentary particles, *J. Sediment. Petrol.*, *23*, 117-119.

Riley, N. A. (1941), Projection sphericity, *J. Sediment. Petrol.*, *11*, 94-97.

Roof, S., and Callagan, C. (2003), The Climate of Death Valley, California, *Bull. Am. Meteorol. Soc.*, *84*, 1725-1738, doi: 10.1175/BAMS-84-12-1725.

Rubin, D. M. (2004), A simple autocorrelation algorithm for determining grain size from digital images of sediment, *J. Sediment. Res.*, *74*, 160-165, doi: 10.1306/052203740160.

Sanders, G. B., and Larson, W. E. (2011), Integration of in-situ resource utilization into lunar/Mars exploration through field analogs, Adv. Space Res., 74, 20-19, doi: 10.1016/j.asr.2010.08.020

Sime, L. C., and Ferguson, R. I. (2003), Information on grain sizes in gravel-bed rivers by automated image analysis, *J. Sediment. Res*., *73*, 630-639.

Sneed, E. D., and Folk, R. L. (1958), Pebbles in the lower Colorado River, Texas a study of particle morphogenesis, *J. of Geol.*, 66, 114-150.

Squyres, S. W., et al. (2004), The Spirit Rover's Athena science investigation at Gusev Crater, Mars, Science, 305, doi: 10.1126/science.305079.

Sullivan, R., et al., (2005), Aeolian processes at the Mars Exploration Rover Meridiani Planum landing site, *Nature*, *436*.

Sullivan, R., Arvidson, R., Bell, J. F., Gellert, R., Golomback, M., Greeley, R., Herkenhoff, K., Johnson. J., Thompson, S., Whelley, P., and Wray, J. (2008), Wind-driven particle mobility on Mars: Insights from Mars Exploration Rover observations at "El Dorado" and surrounding Gusev Crater, *J. Geophys. Res.*, *113*, E06S07, doi: 10.1029/2008JE003101.

Swezey, C., (1998), The identification of eolian sands and sandstones, *Sciences de la terre et des planetes / Earth & Planetary Sciences*, 327, 513-518.

Szabo, T., Domokos, G., Grotzinger, J. P., and Jerolmack, D. J. (2015), Reconstructing the transport history of pebbles on Mars, *Nat. Commun.*, 6:8366, doi:10.1038/ncomms9366.
Thompson, R. A., Fridrich, C., Chan, C. F., Zellman, K. L., and Workman, J. B., (2014), Volcano-tectonic evolution of the Central Death Valley Volcanic Field – Insights derived

from the geologic map of the Death Valley Junction 30’ x 60’ Quadrangle, paper presented at American Geophysical Union Fall Meeting, Sand Francisco, California.

Tibbets, A. K. (2010), Petrogenesis of the Greenwater Range: Comparisons to the Crater Flat Volcanic Field and implications for hazard assessment, M.S. Thesis, Dept. of Geoscience, Univ. of Nevada Las Vegas, Las Vegas, Nevada.

Van der Plas, L., and Tobi, A. C. (1965), A chart for judging the reliability of point counting results, *Am. J. of Sci., 263,* 87-90.

Wentworth, C. K. (1919), A laboratory study of cobble abrasion, *J. of Geol.*, 27, 507-521.

Wentorth, C. K. (1922), A scale and class terms for clastic sediments, *J. of Geol., 30*, 377-392.

Williams, R. M. E., et al. (2013), Martian fluvial conglomerates at Gale Crater, *Science*, *340*, 1068-1072, doi: 10.1126/science.123731.

Yingst, R. A., Haldermann, A. F. C., Biederman, K. L., and Monhead, A. M. (2007), Quantitative morphology of rocks at the Mars Pathfinder landing site, *J. Geophys. Res.*, *112*, E06002, doi: 10.1029/2005JE00258.

Yingst, R. A., Crumpler, L, Farrand, W. H., Li, R., Cabrol, N. A., and Neakrase, L. D. (2008), Morphology and texture of particles along the spirit rover traverse from sol 450 to sol 745, *J. Geophys. Res.*, *113,* E12S41, doi: 10.1029/2008JE003179.

Yingst, R. A., et al. (2013), Characteristics of pebble- and cobble-sized clasts along the curiosity rover traverse from Bradbury Landing to Rocknest, *J. Geophys. Res.*, *118*, 1-20, doi:10.1002/2013JE004435.

Yingst, R. A., Kenneth, S. E., Kennedy, M. R., Krezoski, G. M., McBride, M. J., Miniti, M. E., Ravine, M. A., and Williams, R. M. E. (2016), MAHLI on Mars: Lessons learned operating a geoscience camera on a landed payload robotic arm, *Geosci. Instum. Method. Data. Syst*., *5*, 205-217, doi: 10.5194/gi-5-205-2016.

APPENDICES

Appendix A

Aeolian and fluvial sediment images.

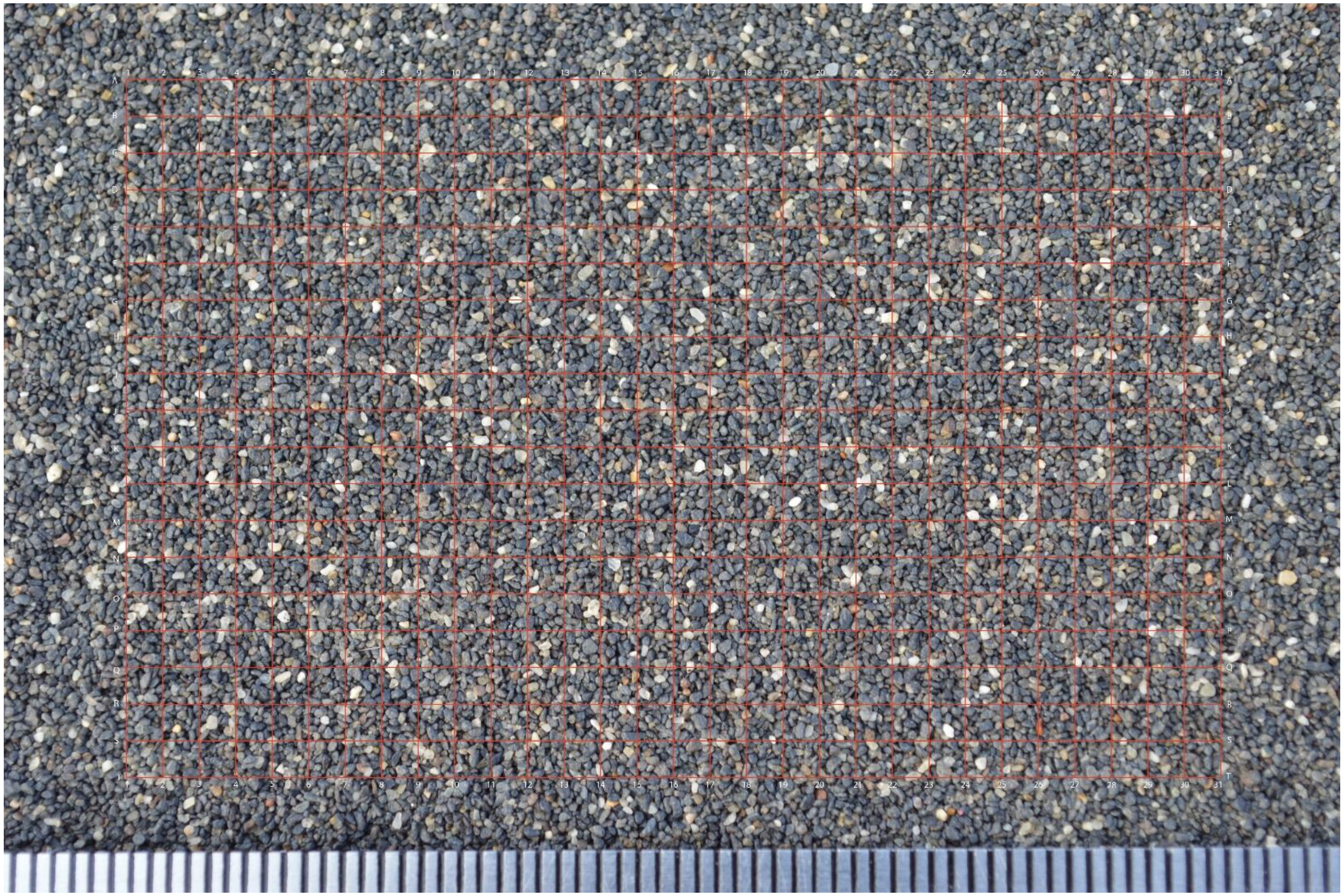

Figure A1: Image of aeolian sediment taken under even illumination at 11 μm/pixel image resolution.

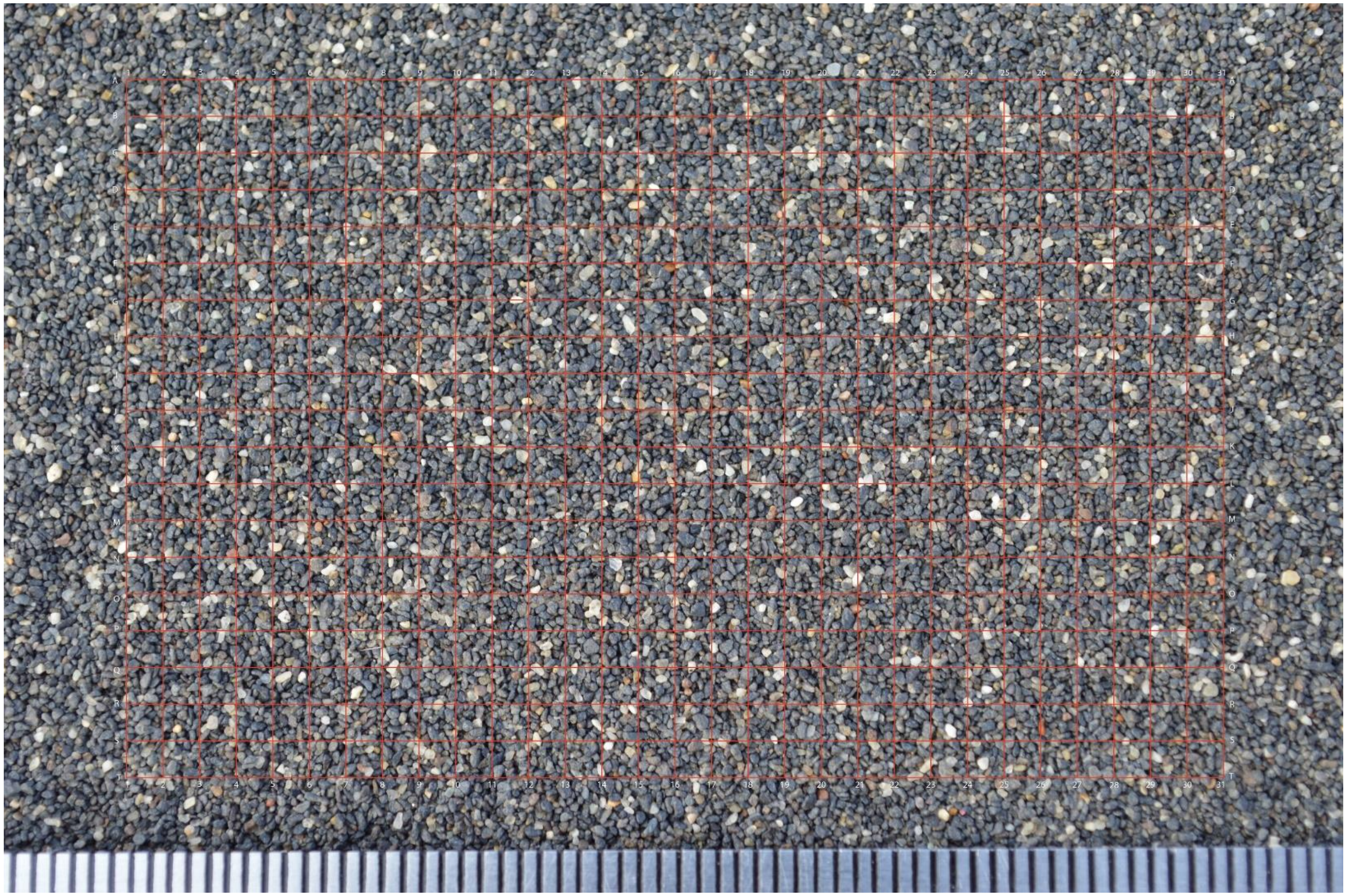

Figure A2: Image of aeolian sediment taken under even illumination and resampled to 20 μm/pixel image resolution.

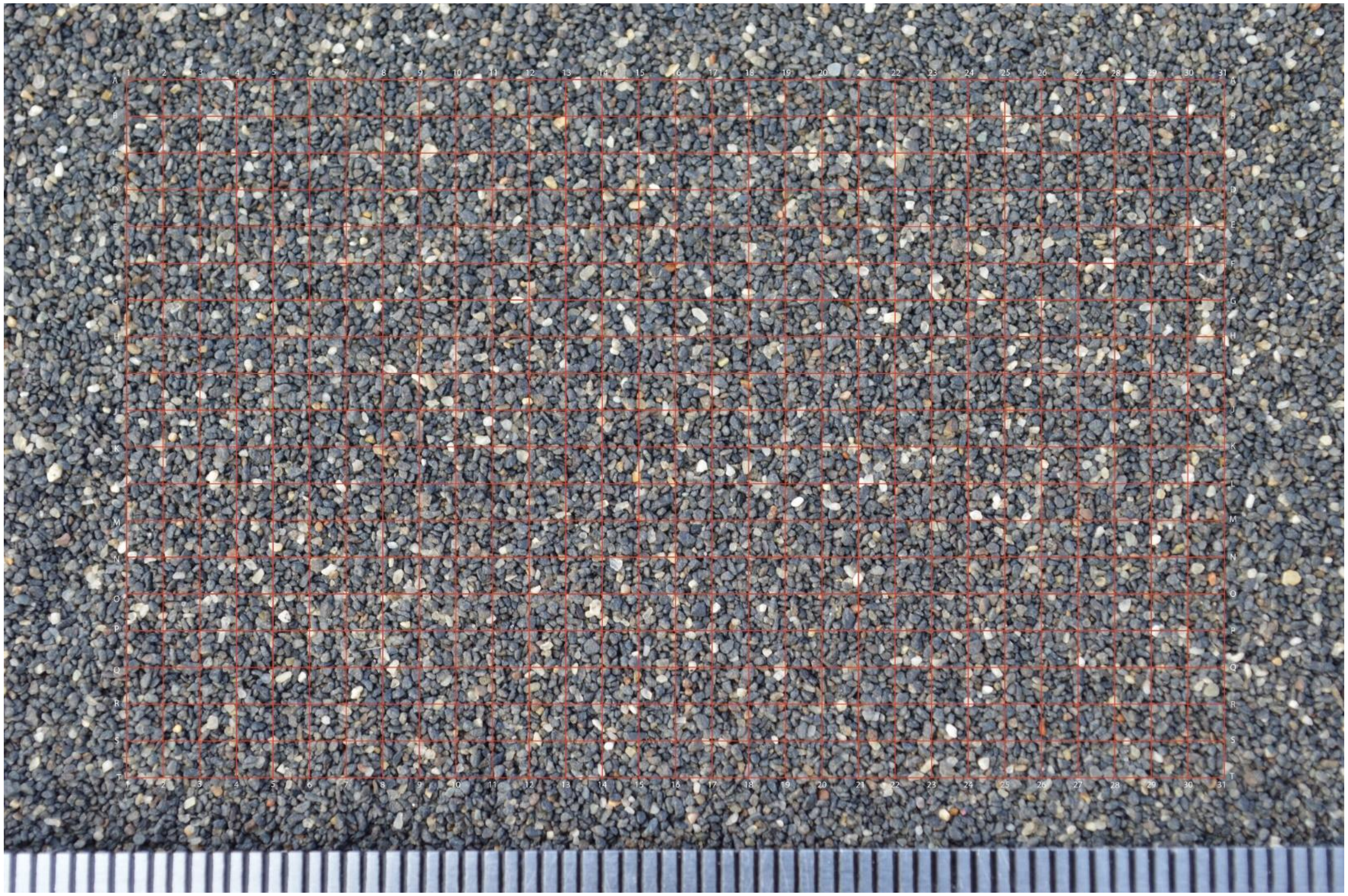

Figure A3: Image of aeolian sediment taken under even illumination and resampled to 30 μm/pixel image resolution.

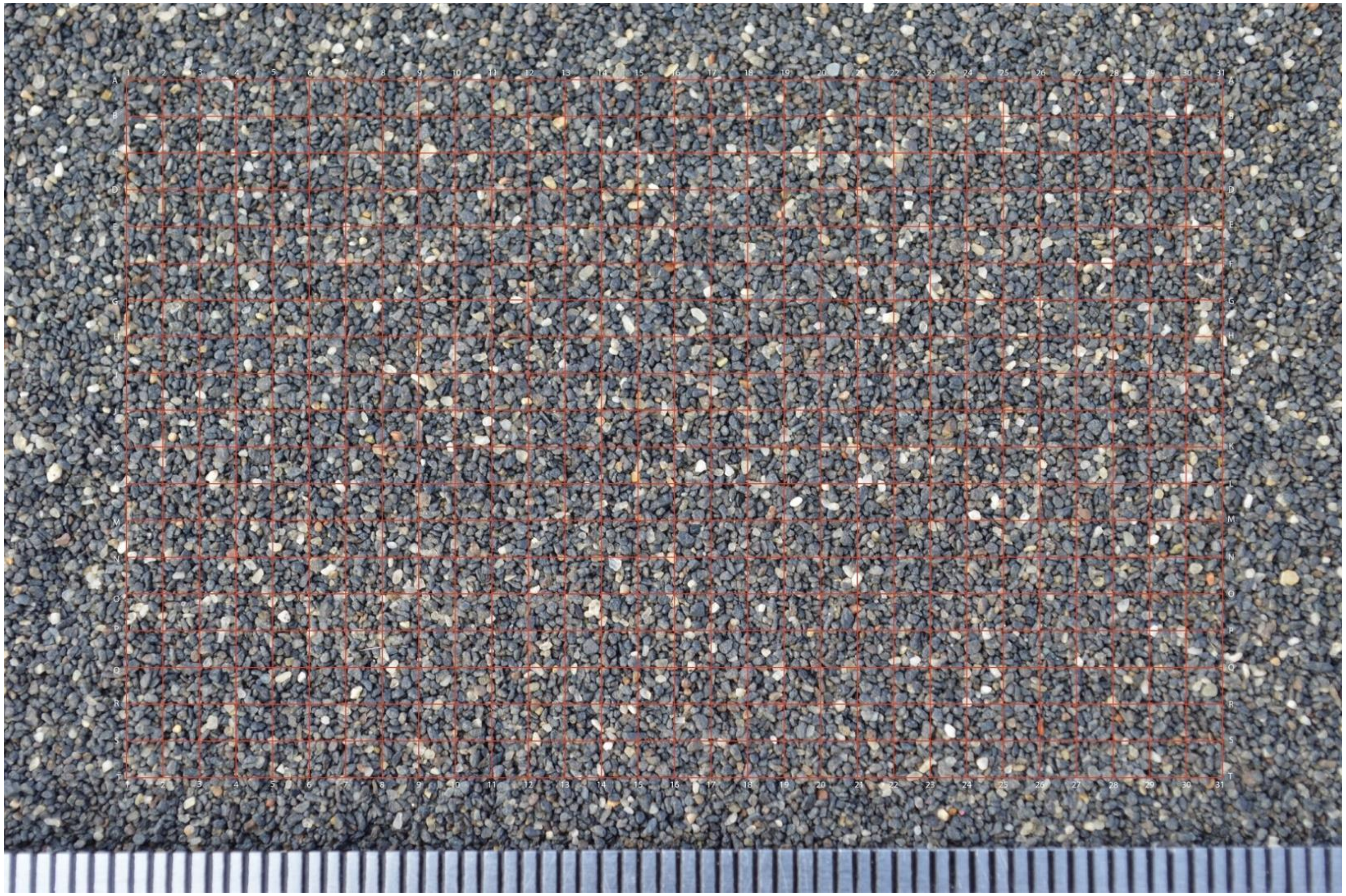

Figure A4: Image of aeolian sediment taken under even illumination and resampled to 40 μm/pixel image resolution.

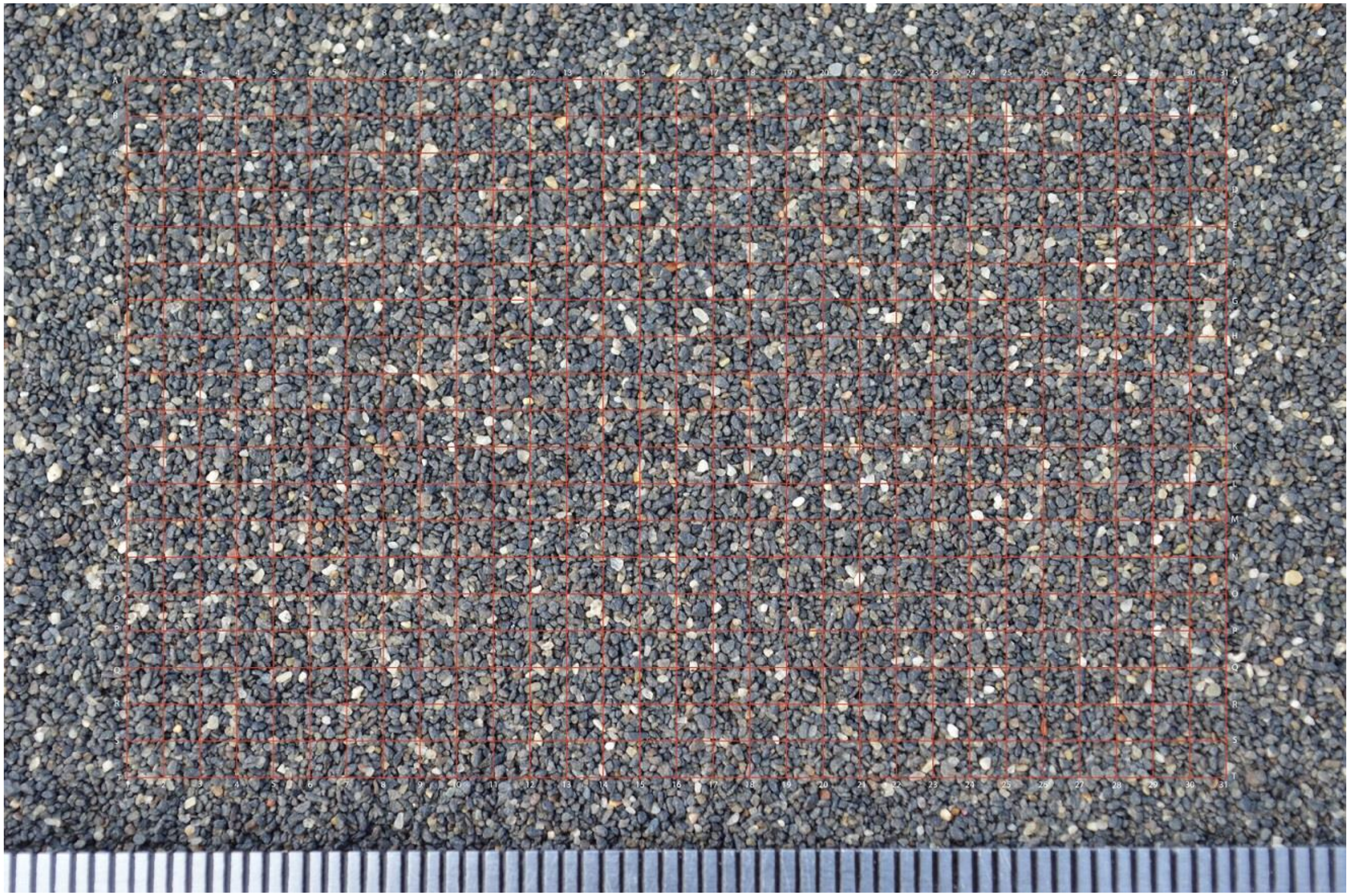

Figure A5: Image of aeolian sediment taken under even illumination and resampled to 50 μm/pixel image resolution.

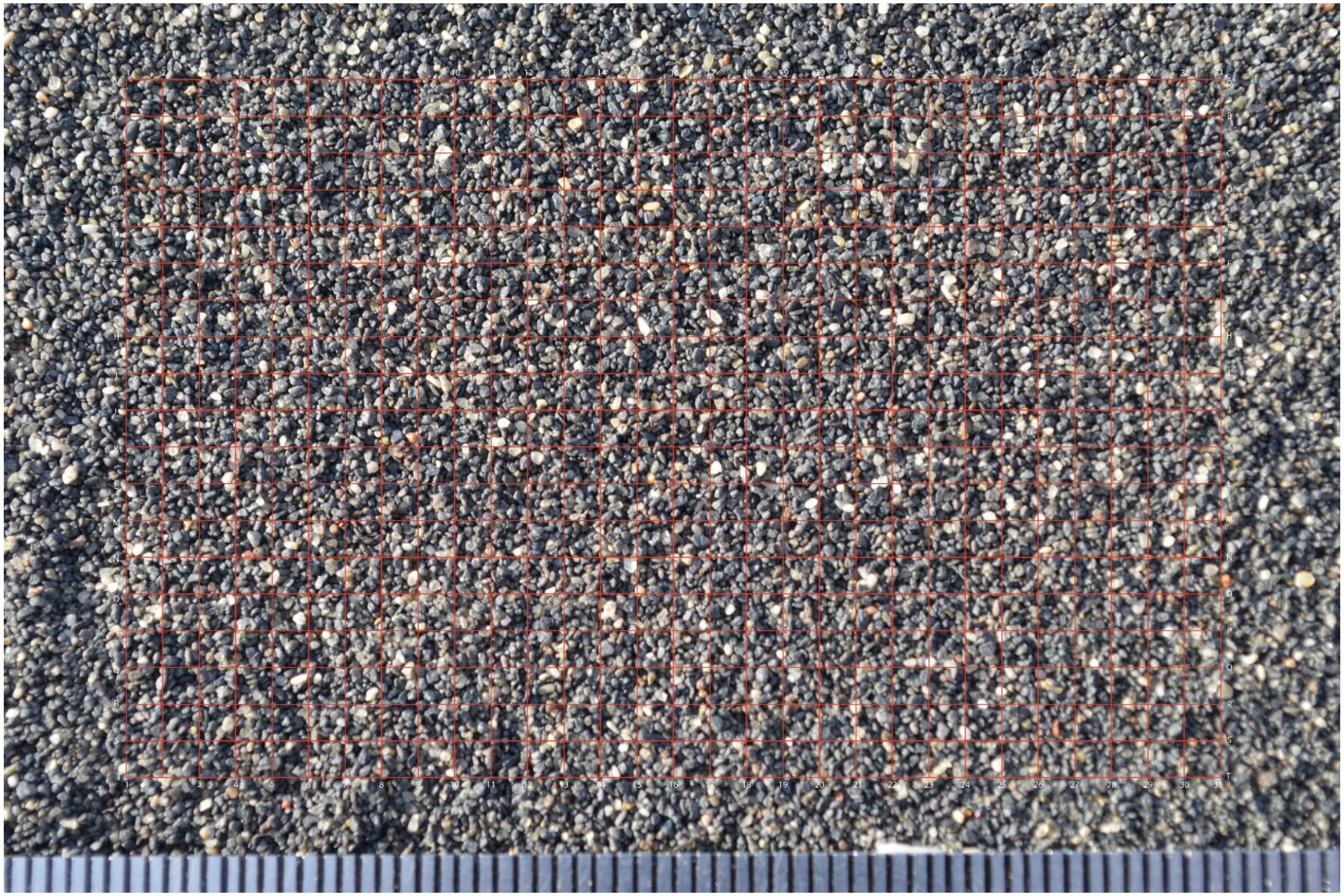

Figure A6: Image of aeolian sediment taken under 20° incident angle at 11 μm/pixel image resolution.

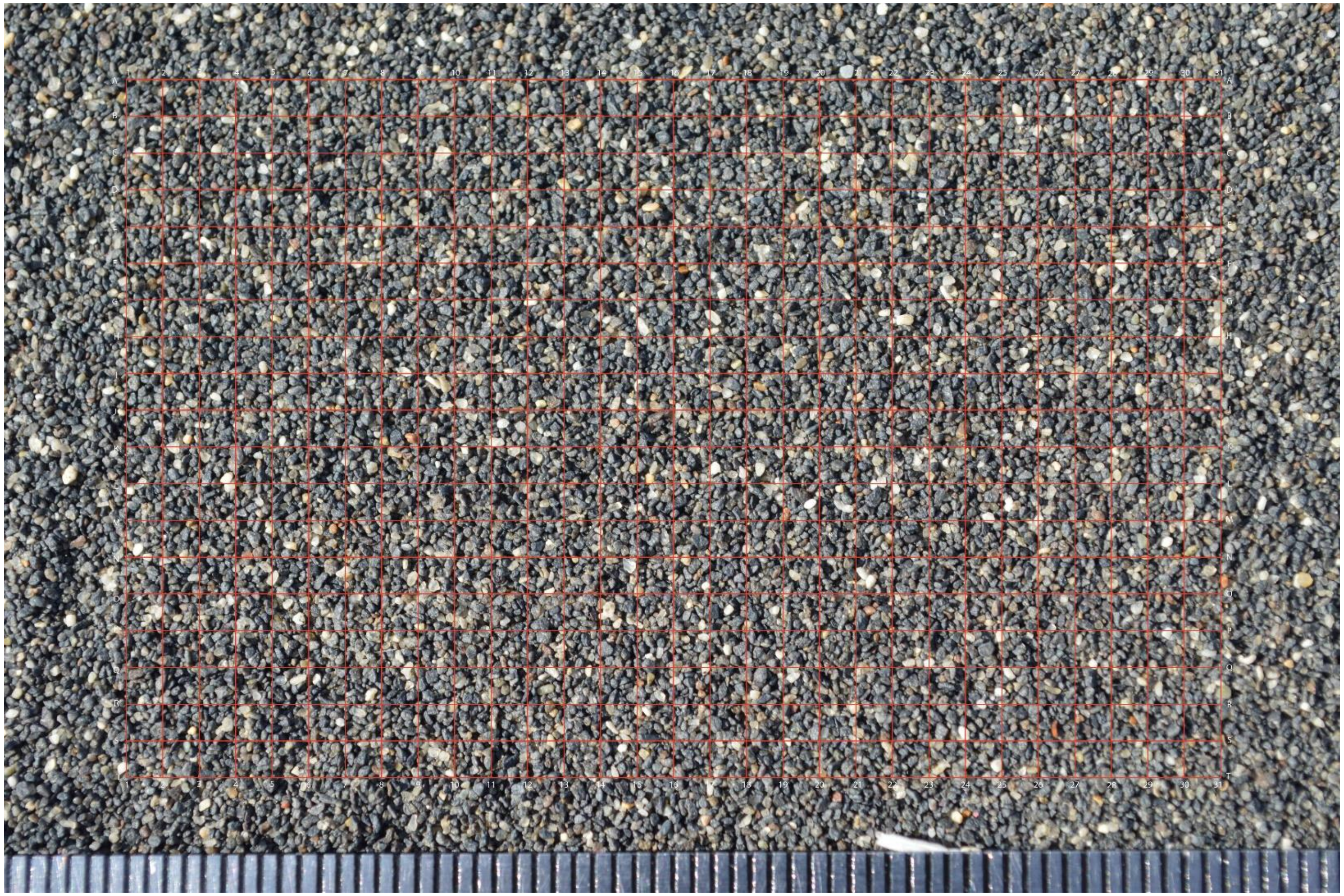

Figure A7: Image of aeolian sediment taken under 40° incident angle at 11 μm/pixel image resolution.

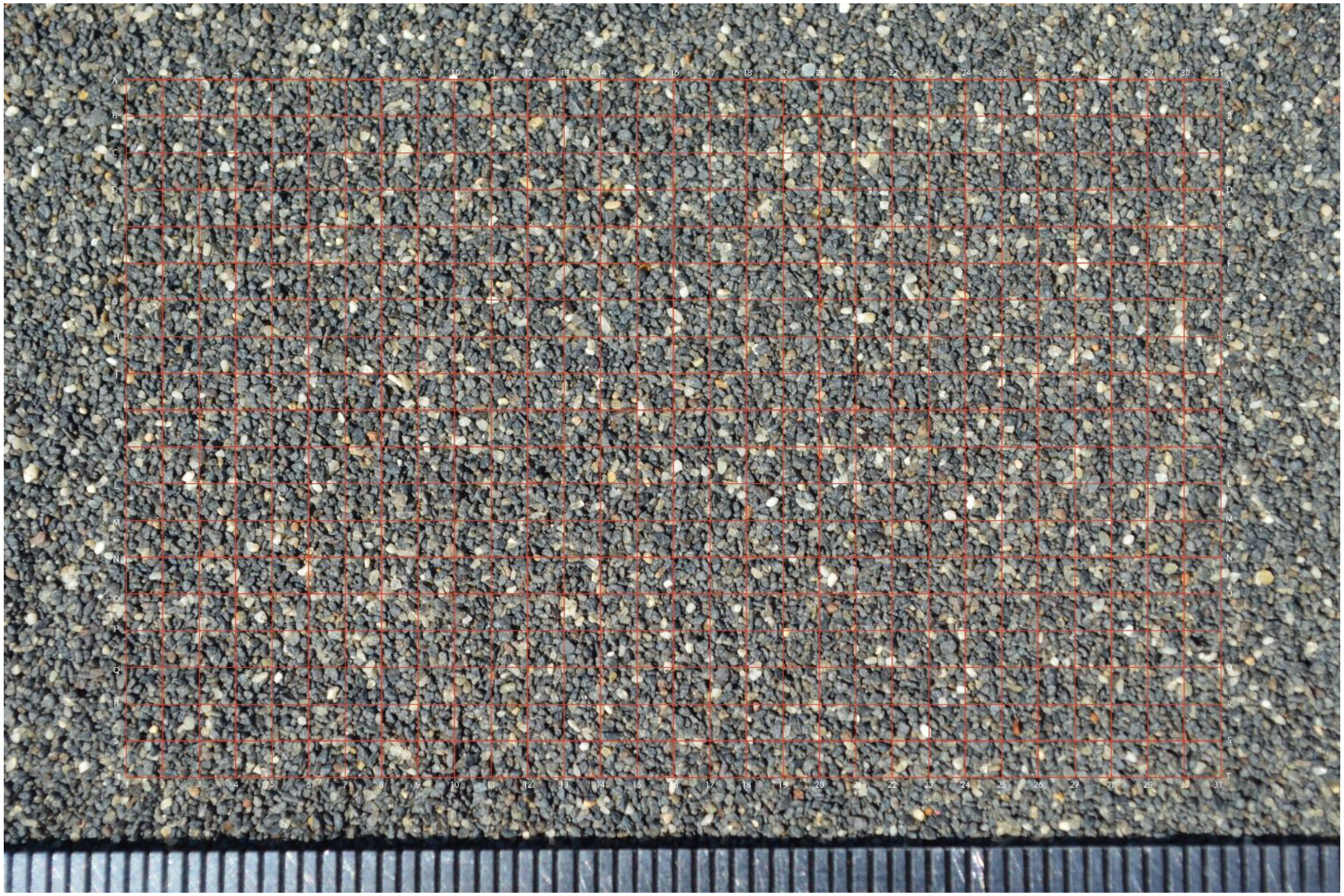

Figure A8: Image of aeolian sediment taken under 60° incident angle at 11 μm/pixel image resolution.

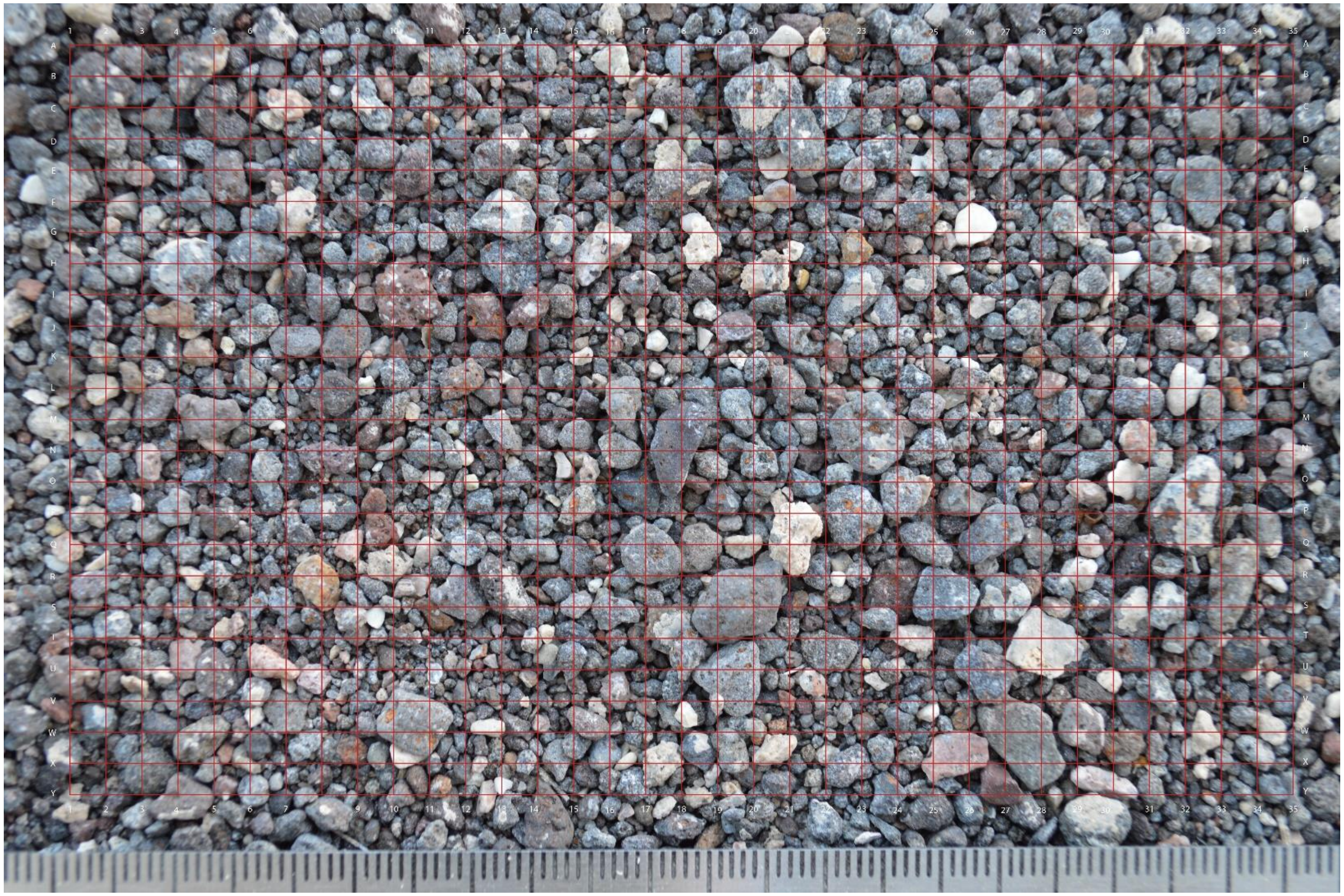

Figure A9: Image of fluvial sediment taken under even illumination at 19 µm/pixel image resolution.

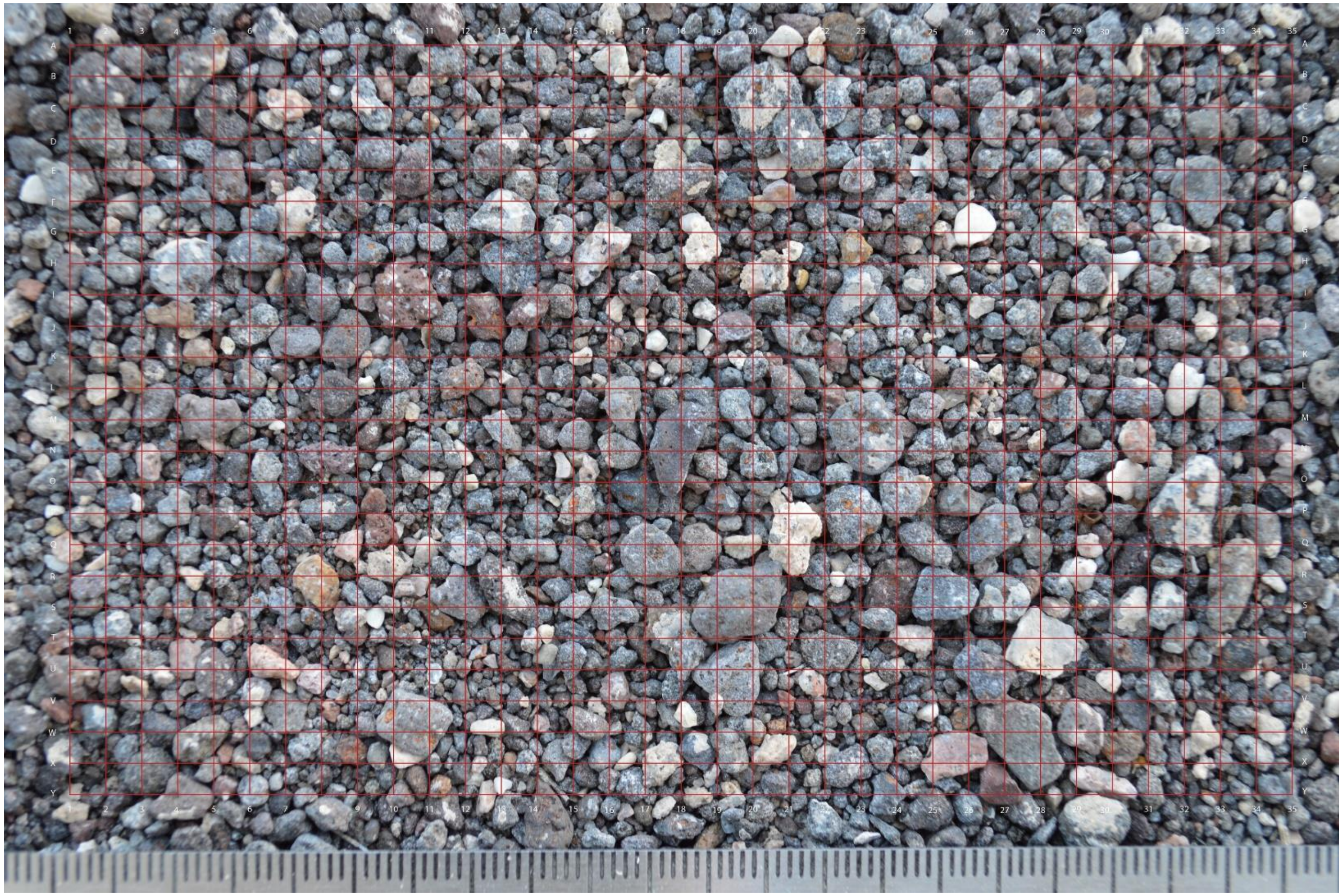

Figure A10: Image of fluvial sediment taken under even illumination and resampled to 40 μm/pixel image resolution.

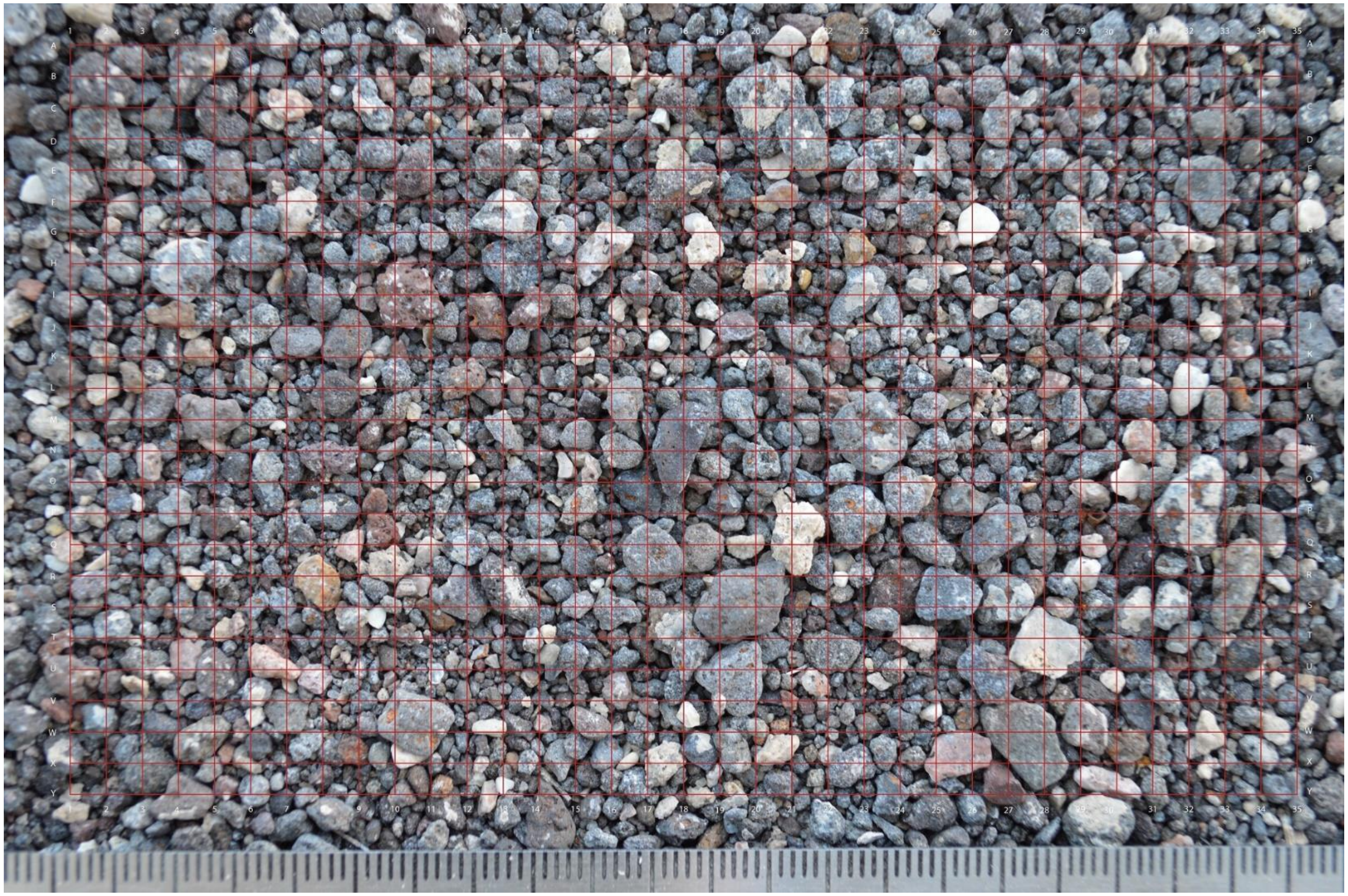

Figure A11: Image of fluvial sediment taken under even illumination and resampled to 60 μm/pixel image resolution.

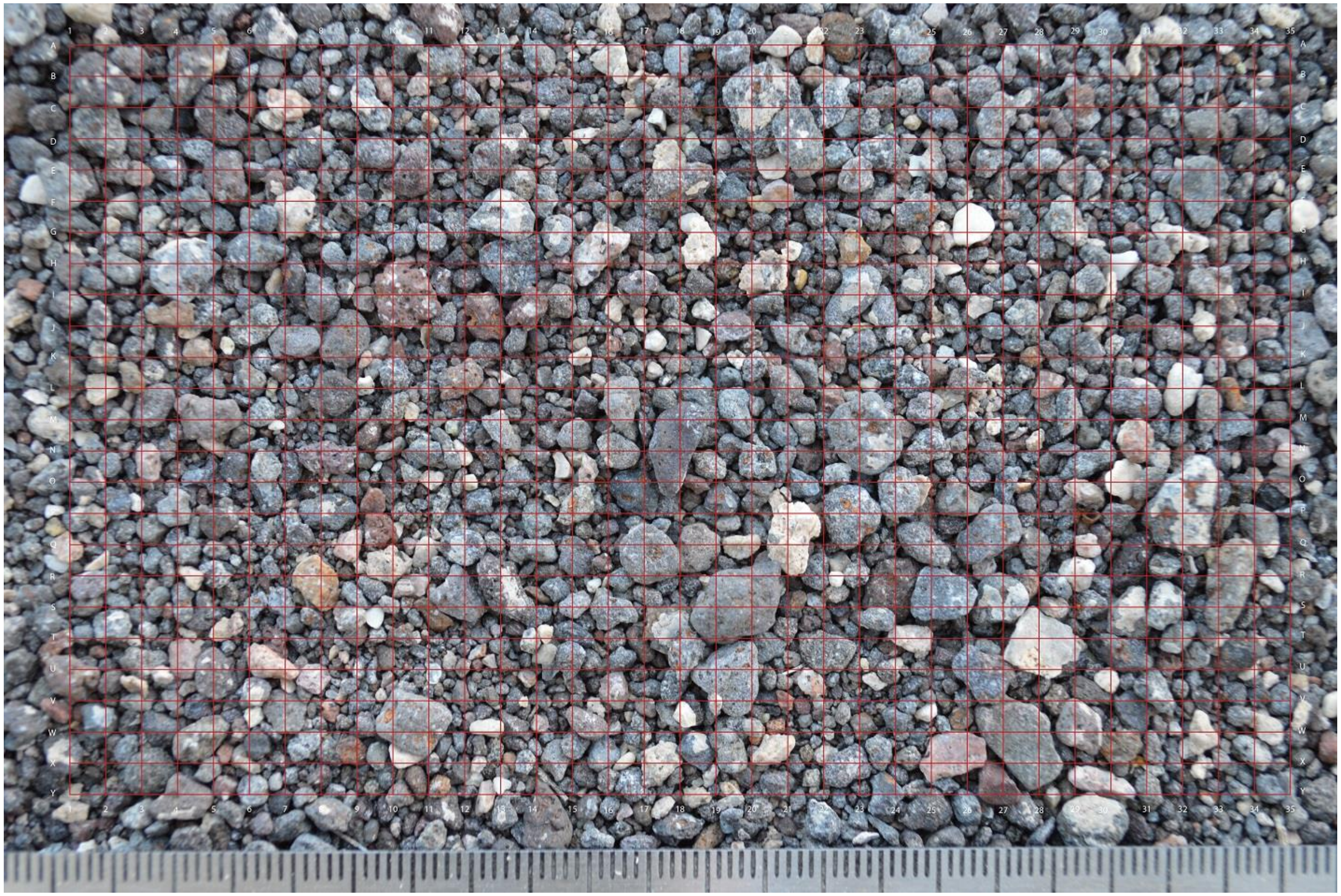

Figure A12: Image of fluvial sediment taken under even illumination and resampled to 80 μm/pixel image resolution.

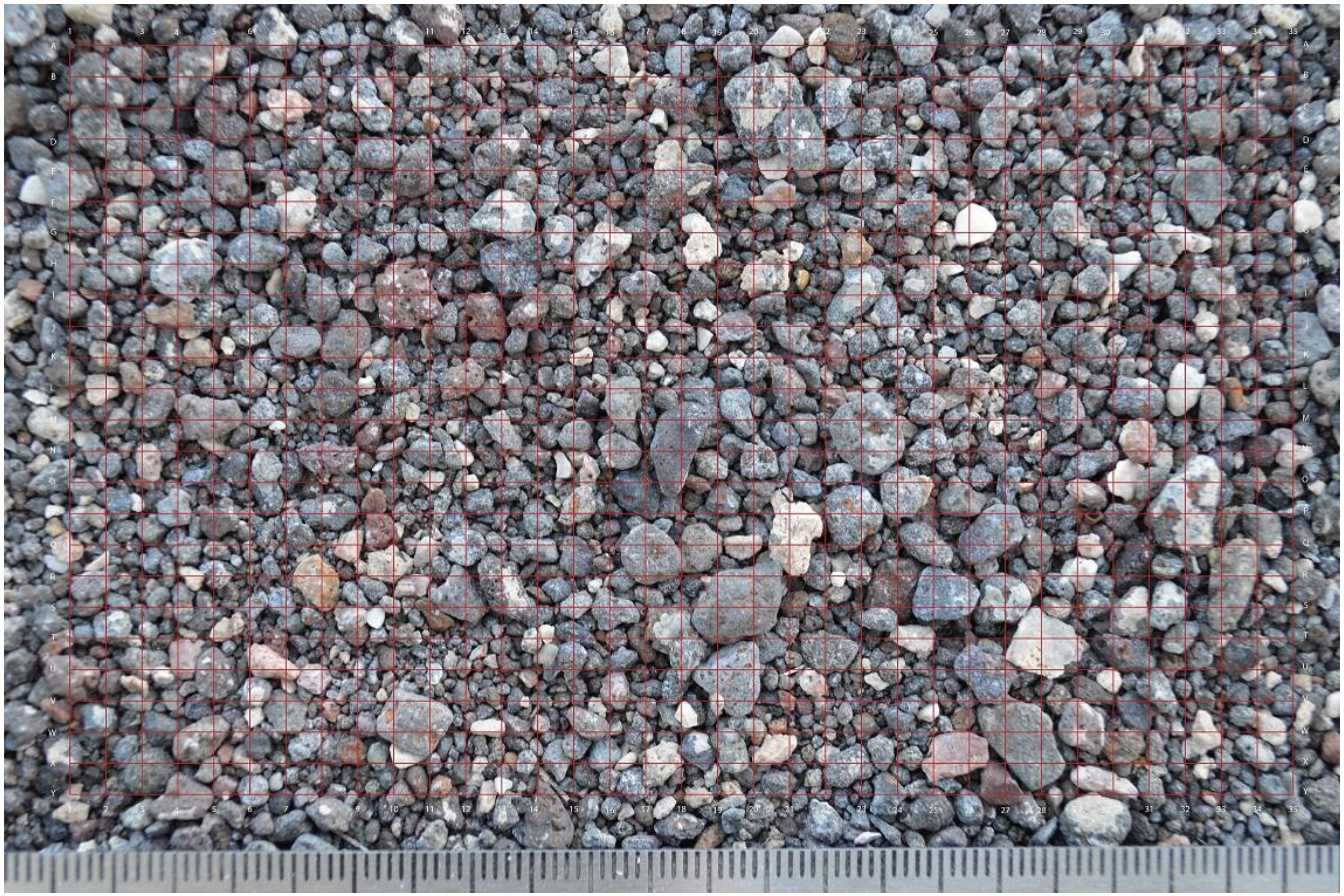

Figure A13: Image of fluvial sediment taken under even illumination and resampled to 100 μm/pixel image resolution

Appendix B

Examples of 2D grain-size measurements resulting in low agreement when repeated by a single user or reproduced by two users.

.

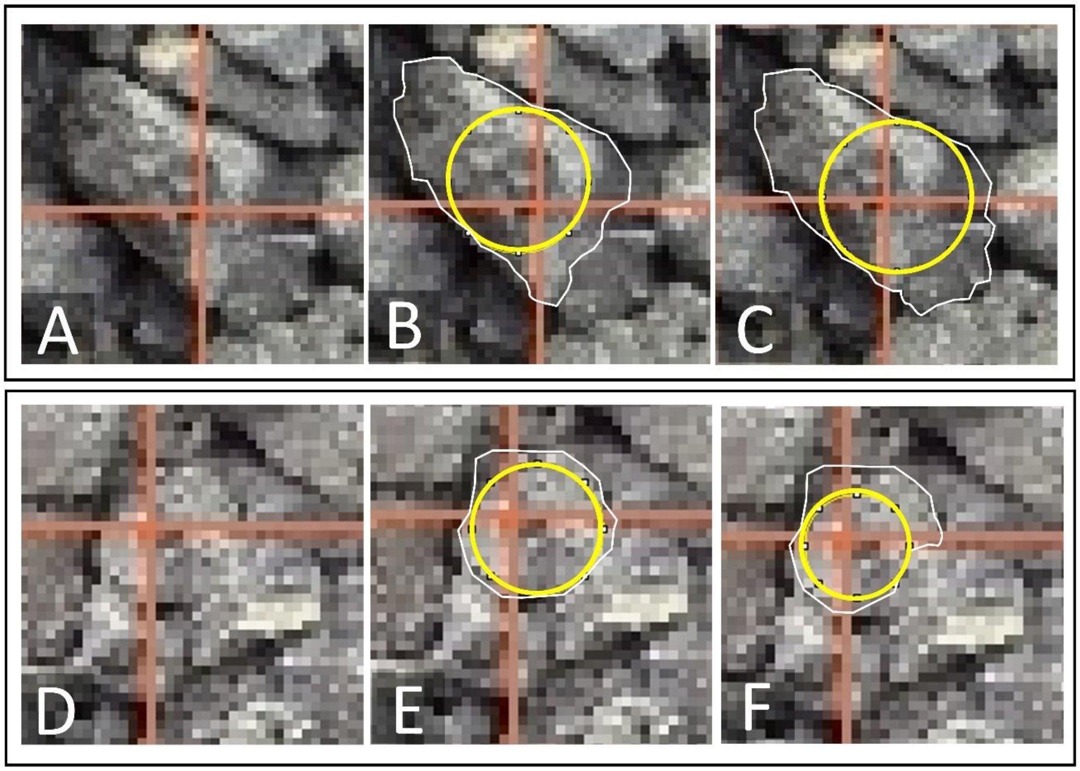

Figure B1: Two examples (top, bottom) of D_i measurements that have low measurement agreement when reproduced by two different users. Measurements differ because grain boundaries were interpreted differently by the two users. Yellow circles are estimated placements of user measurements. White grain outlines are possible grain boundaries interpreted by the user. (A) Grain that was measured differently by two users. (B) User 1 D_i measurement. (C) User 2 D_i measurement. (D) Grain that was measured differently by two users. (E) User 1 D_i measurement. (F) User 2 D_i measurement.

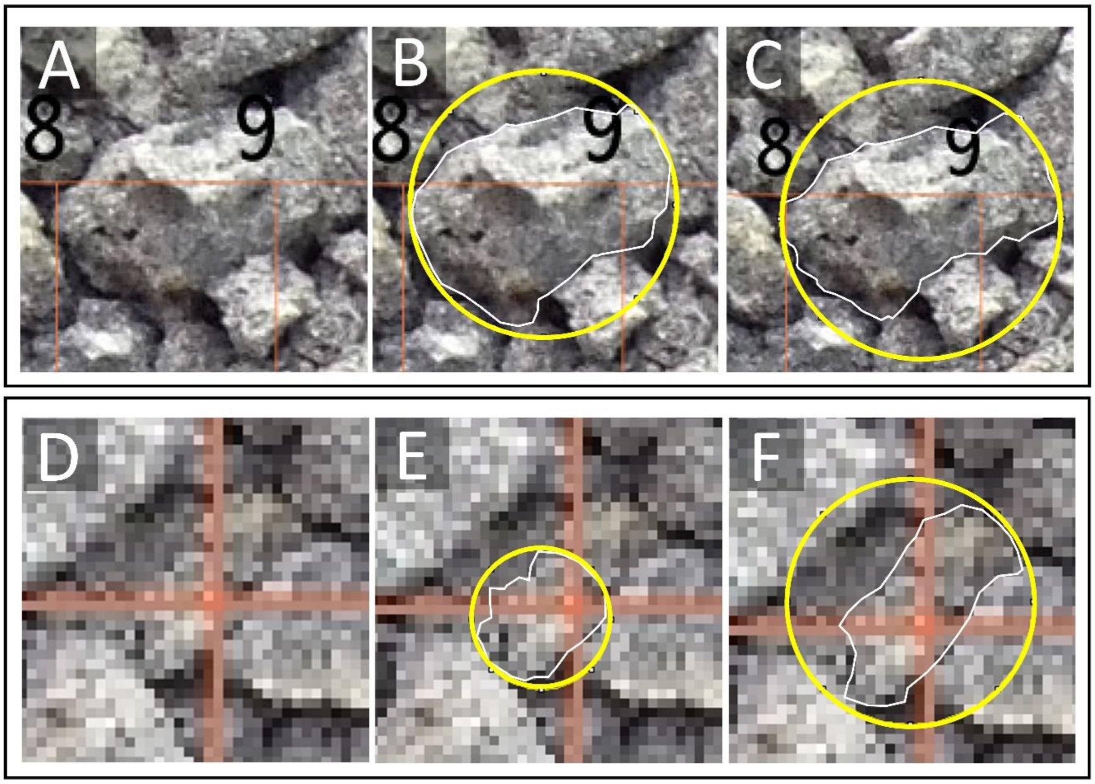

Figure B2: Two examples (top, bottom) of D_c measurements that have low measurement agreement when repeated by the same user. Measurements differ because grain boundaries were interpreted differently by the user when measured two separate times. Yellow circles are estimated placements of user measurements. White grain outlines are possible grain boundaries interpreted by user. (A) Grain that was measured differently when repeated by the same user. (B) User's initial D_c measurement. (c) User's repeated D_c measurement. (D) Grain that was measured differently when repeated by the same user. (E) User's initial D_c measurement. (F) User's repeated D_c measurement.

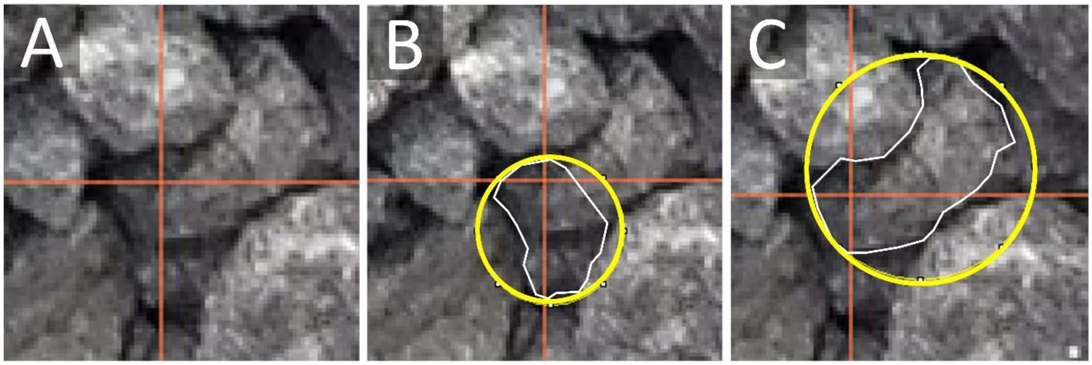

Figure B3: Example of grid node falling on the boundary of two touching grains where two different users measured different grains. Yellow circles are estimated placements of user measurements. White grain outlines are possible grain boundaries inferred by user. (A) Grid line falls on boundary of two grains. (B) User 1 Dc measurement. (C) User 2 Dc measurement.

Appendix C

Grain-size distributions from aeolian and fluvial sediment sieving, 2D D_i measurements, and 2D D_c measurements.

Table C1: Aeolian sediment sieve grain size distribution and 2D grain-size distributions calculated from the D_i and D_c grain measurements at 11 μm/pixel image resolution.

Sediment	Grain Size (phi)	Wt. (g)	Wt. (%)	Cumulative (%)
3D Sediment (Sieve)	0.00	0.00	0.00	0.00
	0.50	0.04	0.01	0.01
	1.00	3.99	1.20	1.22
	1.50	162.40	49.01	50.23
	2.00	149.61	45.15	95.38
	2.50	12.71	3.84	99.21
	3.00	1.92	0.58	99.79
	3.50	0.61	0.18	99.98
	4.00	0.08	0.02	100.00
	4.50	0.00	0.00	100.00
Image	Grain Size (phi)	Freq.	Freq. (%)	Cumulative (%)
11 μm/pixel image (Di measurement)	0.00	0	0.00	0.00
	0.50	1	0.25	0.25
	1.00	26	6.50	6.75
	1.50	133	33.25	40.00
	2.00	171	42.75	82.75
	2.50	45	11.25	94.00
	3.00	19	4.75	98.75
	3.50	5	1.25	100.00
	4.00	0	0.00	100.00
11 μm/pixel image (Dc measurement)	-0.50	0	0.00	0.00
	0.00	9	2.25	2.25
	0.50	77	19.25	21.50
	1.00	209	52.25	73.75
	1.50	79	19.75	93.50
	2.00	20	5.00	98.50
	2.50	5	1.25	99.75
	3.00	1	0.25	100.00
	3.50	0	0.00	100.00

Table C2: Fluvial sediment sieve grain-size distribution and 2D grain-size distributions calculated from the D_i and D_c grain measurements at 19 μm/pixel image resolution.

Sediment	Grain Size (phi)	Wt. (g)	Wt. (%)	Cumulative (%)
3D sediment (Sieve)	-3.50	0.00	0.00	0.00
	-3.00	15.70	1.23	1.23
	-2.50	24.91	1.96	3.19
	-2.00	72.36	5.68	8.87
	-1.50	150.14	11.79	20.66
	-1.00	282.70	22.20	42.86
	-0.50	324.49	25.48	68.33
	0.00	239.78	18.83	87.16
	0.50	97.46	7.65	94.81
	1.00	39.28	3.08	97.90
	1.50	14.64	1.15	99.05
	2.00	5.26	0.41	99.46
	2.50	2.54	0.20	99.66
	3.00	1.26	0.10	99.76
	3.50	0.96	0.08	99.83
	4.00	0.90	0.07	99.90
	4.50	0.82	0.06	99.97
	5.00	0.39	0.03	100.00
	5.50	0.00	0.00	100.00
Image	**Grain Size (phi)**	**Freq.**	**Freq. (%)**	**Cumulative (%)**
19 μm/pixel image (Di measurement)	-3.00	0	0.00	0.00
	-2.50	2	0.50	0.50
	-2.00	12	3.00	3.50
	-1.50	50	12.50	16.00
	-1.00	109	27.25	43.25
	-0.50	84	21.00	64.25
	0.00	77	19.25	83.50
	0.50	37	9.25	92.75
	1.00	18	4.50	97.25
	1.50	9	2.25	99.50
	2.00	2	0.50	100.00
	2.50	0	0.00	100.00
19 μm/pixel image (Dc measurement)	-3.50	0	0.00	0.00
	-3.00	4	1.00	1.00
	-2.50	19	4.75	5.75
	-2.00	64	16.00	21.75
	-1.50	125	31.25	53.00
	-1.00	86	21.50	74.50
	-0.50	64	16.00	90.50
	0.00	23	5.75	96.25
	0.50	11	2.75	99.00
	1.00	4	1.00	100.00
	1.50	0	0.00	100.00

Appendix D

Converted 2D grain-size distributions.

Table D1: Aeolian and fluvial 2D grain-size distributions converted using the Kellerhals and Bray (1971) conversion factor.

Image	Grain Size (phi)	Freq.	Freq. (%)	Cumulative (%)
Fluvial Sediment				
Converted 19 µm/pixel image (Di measurement)	-3.00	0.00	0.00	0.00
	-2.50	3.36	1.73	1.73
	-2.00	14.27	7.35	9.08
	-1.50	42.04	21.64	30.72
	-1.00	64.81	33.37	64.09
	-0.50	35.32	18.18	82.27
	0.00	22.89	11.78	94.05
	0.50	7.78	4.00	98.06
	1.00	2.68	1.38	99.44
	1.50	0.95	0.49	99.92
	2.00	0.15	0.08	100.00
	2.50	0.00	0.00	100.00
Aeolian Dune Sediment				
Converted 11 µm/pixel image (Di measurement)	0.00	0.00	0.00	0.00
	0.50	0.21	0.62	0.62
	1.00	3.86	11.39	12.00
	1.50	13.98	41.18	53.19
	2.00	12.64	37.22	90.41
	2.50	2.42	7.12	97.53
	3.00	0.71	2.08	99.61
	3.50	0.13	0.39	100.00
	4.00	0.00	0.00	100.00

Appendix E

Textural parameters.

Table E1: Textural parameters.

Udden-Wentworth Grain Size Classification			
Grain Size		Size Term	
Phi	mm		
-5	32	Pebbles	V. Coarse
-4	16	Pebbles	Coarse
-3	8	Pebbles	Medium
-2	4	Pebbles	Fine
-1	2	Pebbles	V. Fine
0	1	Sand	V. Coarse
1	0.5	Sand	Coarse
2	0.25	Sand	Medium
3	0.125	Sand	Fine
4	0.063	Sand	V. Fine
5	0.031	Silt	Coarse
6	0.016	Silt	Medium
7	0.008	Silt	Fine
8	0.004	Silt	V. Fine

Inclusive Graphic Standard Deviation	
Sorting	Description
< 0.35	Very Well Sorted
0.35 - 0.5	Well Sorted
0.5 - 0.71	Moderately Well Sorted
0.71 - 1.0	Moderately Sorted
1.0 - 2.0	Poorly Sorted
2.0 - 4.0	Very Poorly Sorted
> 4.0	Extremely Poorly Sorted

Inclusive Graphic Skewness	
Skewness	Description
1.0 - 0.3	Strongly Fine Skewed
0.3 - 0.1	Fine Skewed
0.0 - -0.1	Symmetrical
-0.1 - -0.3	Coarse Skewed
-0.3 - 1	Strongly Coarse Skewed

Riley Sphericity (2D) and Maximum Projection Sphericity (3D)	
Sphericity	Description
> 0.75	Very Equant
0.75 - 0.72	Equant
0.72 - 0.69	Subequant
0.60 - 0.66	Intermediate Shape
0.66 - 0.63	Subelongate
0.6 - 0.63	Elongate
< 0.6	Very Elongate

Appendix F

Grain-size distributions from image analysis and sieving.

Table F1: Aeolian dune and fluvial sediment grain-size distributions determined by sieving.

Grain Size (Φ)	Wt. (g)	Wt. (%)	Cumulative (%)
Aeolian Dune Sediment			
0.00	0.00	0.00	0.00
0.50	0.04	0.01	0.01
1.00	3.99	1.20	1.22
1.50	162.40	49.01	50.23
2.00	149.61	45.15	95.38
2.50	12.71	3.84	99.21
3.00	1.92	0.58	99.79
3.50	0.61	0.18	99.98
4.00	0.08	0.02	100.00
4.50	0.00	0.00	100.00
Fluvial Sediment			
-3.50	0.00	0.00	0.00
-3.00	15.70	1.23	1.23
-2.50	24.91	1.96	3.19
-2.00	72.36	5.68	8.87
-1.50	150.14	11.79	20.66
-1.00	282.70	22.20	42.86
-0.50	324.49	25.48	68.33
0.00	239.78	18.83	87.16
0.50	97.46	7.65	94.81
1.00	39.28	3.08	97.90
1.50	14.64	1.15	99.05
2.00	5.26	0.41	99.46
2.50	2.54	0.20	99.66
3.00	1.26	0.10	99.76
3.50	0.96	0.08	99.83
4.00	0.90	0.07	99.90
4.50	0.82	0.06	99.97
5.00	0.39	0.03	100.00
5.50	0.00	0.00	100.00

Table F2: Aeolian sediment grain-size distributions determined from images of 19, 20, 30, 40, and 50 μm/pixel resolution.

Image	Grain Size (Φ)	Freq.	Freq. (%)	Cumulative (%)
11 μm/pixel image	0.00	0	0.00	0.00
	0.50	1	0.25	0.25
	1.00	26	6.50	6.75
	1.50	133	33.25	40.00
	2.00	171	42.75	82.75
	2.50	45	11.25	94.00
	3.00	19	4.75	98.75
	3.50	5	1.25	100.00
	4.00	0	0.00	100.00
20 μm/pixel image	0.00	0	0.00	0.00
	0.50	1	0.25	0.25
	1.00	21	5.25	5.50
	1.50	130	32.50	38.00
	2.00	176	44.00	82.00
	2.50	55	13.75	95.75
	3.00	14	3.50	99.25
	3.50	3	0.75	100.00
	4.00	0	0.00	100.00
30 μm/pixel image	0.00	0	0.00	0.00
	0.50	1	0.25	0.25
	1.00	24	6.00	6.25
	1.50	148	37.00	43.25
	2.00	149	37.25	80.50
	2.50	63	15.75	96.25
	3.00	10	2.50	98.75
	3.50	5	1.25	100.00
	4.00	0	0.00	100.00
40 μm/pixel image	0.00	0	0.00	0.00
	0.50	1	0.25	0.25
	1.00	22	5.50	5.75
	1.50	160	40.00	45.75
	2.00	130	32.50	78.25
	2.50	74	18.50	96.75
	3.00	12	3.00	99.75
	3.50	1	0.25	100.00
	4.00	0	0.00	100.00
50 μm/pixel image	0.00	0	0.00	0.00
	0.50	1	0.25	0.25
	1.00	34	8.48	8.73
	1.50	97	24.19	32.92
	2.00	238	59.35	92.27
	2.50	24	5.99	98.25
	3.00	7	1.75	100.00
	3.50	0	0.00	100.00

Table F3: Aeolian sediment grain-size distributions determined from images taken under even illumination and at 20°, 40°, and 60° incident solar angles.

Image	Grain Size (phi)	Freq.	Freq. (%)	Cumulative (%)
Even illumination Image	0.00	0	0.00	0.00
	0.50	1	0.25	0.25
	1.00	26	6.50	6.75
	1.50	133	33.25	40.00
	2.00	170	42.50	82.50
	2.50	46	11.50	94.00
	3.00	19	4.75	98.75
	3.50	5	1.25	100.00
	4.00	0	0.00	100.00
20° Solar Angle Image	0.00	0	0.00	0.00
	0.50	1	0.25	0.25
	1.00	31	7.75	8.00
	1.50	153	38.25	46.25
	2.00	144	36.00	82.25
	2.50	52	13.00	95.25
	3.00	18	4.50	99.75
	3.50	1	0.25	100.00
	4.00	0	0.00	100.00
40° Solar Angle Image	0.00	0	0.00	0.00
	0.50	0	0.00	0.00
	1.00	21	5.25	5.25
	1.50	149	37.25	42.50
	2.00	169	42.25	84.75
	2.50	43	10.75	95.50
	3.00	16	4.00	99.50
	3.50	2	0.50	100.00
	4.00	0	0.00	100.00
60° Solar Angle Image	0.00	0	0.00	0.00
	0.50	0	0.00	0.00
	1.00	27	6.75	6.75
	1.50	125	31.25	38.00
	2.00	165	41.25	79.25
	2.50	56	14.00	93.25
	3.00	21	5.25	98.50
	3.50	5	1.25	99.75
	4.00	1	0.25	100.00
	4.50	0	0.00	100.00

Table F4: Fluvial sediment grain-size distributions determined from images of 19, 40, 60, 80, and 100 µm/pixel image resolution.

Image	Grain Size (phi)	Freq.	Freq. (%)	Cumulative (%)
19 µm/pixel image	-3.00	0	0.00	0.00
	-2.50	2	0.50	0.50
	-2.00	12	3.00	3.50
	-1.50	50	12.50	16.00
	-1.00	109	27.25	43.25
	-0.50	84	21.00	64.25
	0.00	77	19.25	83.50
	0.50	37	9.25	92.75
	1.00	18	4.50	97.25
	1.50	9	2.25	99.50
	2.00	2	0.50	100.00
	2.50	0	0.00	100.00
40 µm/pixel image	-3.00	0	0.00	0.00
	-2.50	1	0.25	0.25
	-2.00	13	3.25	3.50
	-1.50	50	12.50	16.00
	-1.00	110	27.50	43.50
	-0.50	80	20.00	63.50
	0.00	72	18.00	81.50
	0.50	42	10.50	92.00
	1.00	19	4.75	96.75
	1.50	13	3.25	100.00
	2.00	0	0.00	100.00
60 µm/pixel image	-3.00	0	0.00	0.00
	-2.50	1	0.25	0.25
	-2.00	14	3.50	3.75
	-1.50	41	10.25	14.00
	-1.00	101	25.25	39.25
	-0.50	83	20.75	60.00
	0.00	80	20.00	80.00
	0.50	49	12.25	92.25
	1.00	22	5.50	97.75
	1.50	9	2.25	100.00
	2.00	0	0.00	100.00
80 µm/pixel image	-3.00	0	0.00	0.00
	-2.50	2	0.50	0.50
	-2.00	12	3.00	3.50
	-1.50	46	11.50	15.00
	-1.00	108	27.00	42.00
	-0.50	84	21.00	63.00
	0.00	74	18.50	81.50
	0.50	50	12.50	94.00
	1.00	16	4.00	98.00
	1.50	8	2.00	100.00
	2.00	0	0.00	100.00
100 µm/pixel image	-3.00	0	0.00	0.00
	-2.50	1	0.25	0.25
	-2.00	13	3.25	3.50
	-1.50	43	10.75	14.25
	-1.00	105	26.25	40.50
	-0.50	78	19.50	60.00
	0.00	98	24.50	84.50
	0.50	33	8.25	92.75
	1.00	29	7.25	100.00
	1.50	0	0.00	100.00

Appendix G

Grain-size and sphericity summary statistics for the aeolian and fluvial sediments analyzed in 2D and 3D.

Table G1: Aeolian sediment grain-size statistics and sphericity percentiles for the actual sediment and images analyzed at 11, 20, 30, 40, and 50 μm/pixel image resolutions.

Statistic		3D Sediment	11 μm/pixel image	20 μm/pixel image	30 μm/pixel image	40 μm/pixel image	50 μm/pixel image
Folk and Ward Method (Φ)	Mean	1.504	1.601	1.620	1.607	1.611	1.573
	Mode	1.247	1.747	1.747	1.247	1.247	1.747
	Sorting	0.326	0.490	0.454	0.477	0.482	0.413
	Skewness	0.520	0.046	0.026	0.084	0.155	-0.228
Folk and Ward Method (Description)	Mean	Medium Sand	Medium Sand	Medium Sand	Medium Sand	Medium Sand	Medium Sand
	Mode	Medium Sand	Medium Sand	Medium Sand	Medium Sand	Medium Sand	Medium Sand
	Sorting	Very Well Sorted	Well Sorted	Well Sorted	Well Sorted	Well Sorted	Well Sorted
	Skewness	Symmetrical	Symmetrical	Symmetrical	Symmetrical	Fine Skewed	Coarse Skewed
Sphericity Percentiles (sphericity value)	10%	-	0.655	0.632	0.632	0.632	0.632
	25%	-	0.701	0.693	0.686	0.679	0.683
	50%	-	0.767	0.756	0.750	0.750	0.750
	75%	-	0.816	0.816	0.800	0.802	0.798
	90%	-	0.853	0.853	0.837	0.837	0.837
	IQR	-	0.115	0.123	0.114	0.123	0.115
Sphericity Percentiles (Description)	10%	-	Subelongate	Subelongate	Subelongate	Subelongate	Subelongate
	25%	-	Subequant	Subequant	Intermediate Shape	Subelongate	Intermediate Shape
	50%	-	Very Equant	Very Equant	Very Equant	Very Equant	Very Equant
	75%	-	Very Equant	Very Equant	Very Equant	Very Equant	Very Equant
	90%	-	Very Equant	Very Equant	Very Equant	Very Equant	Very Equant

Table G2: Aeolian sediment grain-size statistics and sphericity percentiles for images taken under even illumination and 20°, 40°, and 60° incident solar angles.

Statistic		Even Illumination Image	20° Solar Angle Image	40° Solar Angle Image	60° Solar Angle Image
Folk and Ward Method (Φ)	Mean	1.601	1.571	1.573	1.649
	Mode	1.747	1.247	1.747	1.747
	Sorting	0.490	0.492	0.436	0.523
	Skewness	0.046	0.091	0.068	0.078
Folk and Ward Method (Description)	Mean	Medium Sand	Medium Sand	Medium Sand	Medium Sand
	Mode	Medium Sand	Medium Sand	Medium Sand	Medium Sand
	Sorting	Well Sorted	Well Sorted	Well Sorted	Moderately Well Sorted
	Skewness	Symmetrical	Symmetrical	Symmetrical	Symmetrical
Sphericity Percentiles (sphericity value)	10%	0.655	0.660	0.657	0.639
	25%	0.701	0.722	0.709	0.700
	50%	0.767	0.772	0.770	0.752
	75%	0.816	0.824	0.816	0.801
	90%	0.853	0.860	0.850	0.840
	IQR	0.115	0.102	0.107	0.101
Sphericity Percentiles (Description)	10%	Subelongate	Subelongate	Subelongate	Subelongate
	25%	Subequant	Equant	Subequant	Subequant
	50%	Very Equant	Very Equant	Very Equant	Very Equant
	75%	Very Equant	Very Equant	Very Equant	Very Equant
	90%	Very Equant	Very Equant	Very Equant	Very Equant

Table G3: Fluvial sediment grain-size statistics and sphericity percentiles for the actual sediment and images analyzed 11, 20, 30, 40, and 50 µm/pixel.

Statistic		3D Sediment	19 µm/pixel image (<0.0 phi)	19 µm/pixel image	40 µm/pixel image	60 µm/pixel image	80 µm/pixel image	100 µm/pixel image
Folk and Ward Method (Φ)	Mean	-0.875	-	-0.764	-0.736	-0.673	-0.724	-0.737
	Mode 1	-0.743	-	-1.243	-1.243	-1.243	-1.243	-1.243
	Mode 2	-	-	-	-	-0.243	-	-0.243
	Sorting	0.834	-	0.785	0.815	0.809	0.778	0.752
	Skewness	-0.035	-	0.159	0.193	0.108	0.134	0.055
Folk and Ward Method (Description)	Mean	V. Coarse Sand	-	V. Coarse Sand	V. Coarse Sand	V. Coarse Sand	V. Coarse Sand	V. Coarse Sand
	Mode 1	V. Coarse Sand	-	V. Fine Pebbles	Medium Sand	Medium Sand	Medium Sand	Medium Sand
	Mode 2	-	-	-	-	V. Coarse Sand	-	V. Coarse Sand
	Sorting	Moderately Sorted	-	Moderately Sorted	Moderately Sorted	Moderately Sorted	Moderately Sorted	Moderately Sorted
	Skewness	Symmetrical	-	Fine Skewed	Fine Skewed	Fine Skewed	Fine Skewed	Symmetrical
Sphericity Percentiles (sphericity value)	10%	0.586	0.697	0.677	0.682	0.674	0.671	0.667
	25%	0.656	0.764	0.746	0.748	0.74	0.744	0.731
	50%	0.721	0.808	0.801	0.795	0.797	0.796	0.788
	75%	0.798	0.846	0.841	0.841	0.839	0.84	0.83
	90%	0.858	0.874	0.871	0.871	0.871	0.871	0.866
	IQR	0.142	0.082	0.095	0.093	0.099	0.096	0.099
Sphericity Percentiles (Description)	10%	Very Elongate	Subequant	Intermediate Shape	Intermediate Shape	Intermediate Shape	Intermediate Shape	Intermediate Shape
	25%	Subelongate	Very Equant	Equant	Equant	Equant	Equant	Equant
	50%	Equant	Very Equant	Very Equant	Very Equant	Very Equant	Very Equant	Very Equant
	75%	Very Equant	Very Equant	Very Equant	Very Equant	Very Equant	Very Equant	Very Equant
	90%	Very Equant	Very Equant	Very Equant	Very Equant	Very Equant	Very Equant	Very Equant

Appendix H

Roundness Histograms.

Table H1: Roundness histograms for the 3D aeolian and fluvial sediment.

Roundness	Freq.	Freq. %
Aeolian Sediment		
1	4	1.01
2	39	9.85
3	148	37.37
4	177	44.70
5	28	7.07
6	0	0.00
Fluvial Sediment		
1	0	0.00
2	0	0.00
3	18	4.52
4	286	71.86
5	91	22.86
6	3	0.75

Table H2: Aeolian sediment roundness histogram from images analyzed at 11, 20, 30, 40, and 50 µm/pixel.

Image	Roundness	Freq.	Freq. %
11 µm/pixel image	1	0	0.00
	2	1	0.25
	3	53	13.25
	4	213	53.25
	5	109	27.25
	6	24	6.00
20 µm/pixel image	1	0	0.00
	2	0	0.00
	3	51	12.75
	4	226	56.50
	5	104	26.00
	6	19	4.75
30 µm/pixel image	1	0	0.00
	2	7	1.75
	3	120	30.00
	4	182	45.50
	5	88	22.00
	6	3	0.75
40 µm/pixel image	1	0	0.00
	2	10	2.50
	3	121	30.25
	4	189	47.25
	5	74	18.50
	6	6	1.50
50 µm/pixel image	1	2	0.50
	2	6	1.50
	3	109	27.18
	4	173	43.14
	5	81	20.20
	6	30	7.48

Table H3: Aeolian sediment roundness histograms from images taken under even illumination and at 20°, 40°, and 60° incident solar angles.

Sediment/ Image	Roundness	Freq.	Freq. %
Even Illumination image	1	0	0.00
	2	1	0.25
	3	53	13.25
	4	213	53.25
	5	109	27.25
	6	24	6.00
20° Solar angle image	1	0	0.00
	2	1	0.25
	3	71	17.75
	4	212	53.00
	5	88	22.00
	6	28	7.00
40° Solar angle image	1	0	0.00
	2	5	1.25
	3	95	23.75
	4	199	49.75
	5	79	19.75
	6	22	5.50
60° Solar angle image	1	0	0.00
	2	10	2.50
	3	111	27.75
	4	172	43.00
	5	78	19.50
	6	29	7.25

Table H4: Fluvial sediment roundness histograms from sediment images analyzed at 19, 40, 60, 80, and 100 µm/pixel.

Image	Roundness	Freq.	Freq. %
19 µm/pixel image	1	2	0.50
	2	18	4.50
	3	81	20.25
	4	210	52.50
	5	86	21.50
	6	3	0.75
40 µm/pixel image	1	1	0.25
	2	9	2.25
	3	82	20.50
	4	214	53.50
	5	87	21.75
	6	7	1.75
60 µm/pixel image	1	0	0.00
	2	5	1.25
	3	72	18.00
	4	237	59.25
	5	80	20.00
	6	6	1.50
80 µm/pixel image	1	3	0.75
	2	20	5.00
	3	105	26.25
	4	164	41.00
	5	90	22.50
	6	18	4.50
100 µm/pixel image	1	7	1.75
	2	31	7.75
	3	147	36.75
	4	171	42.75
	5	43	10.75
	6	1	0.25

Appendix I

Relationships between textural parameters.

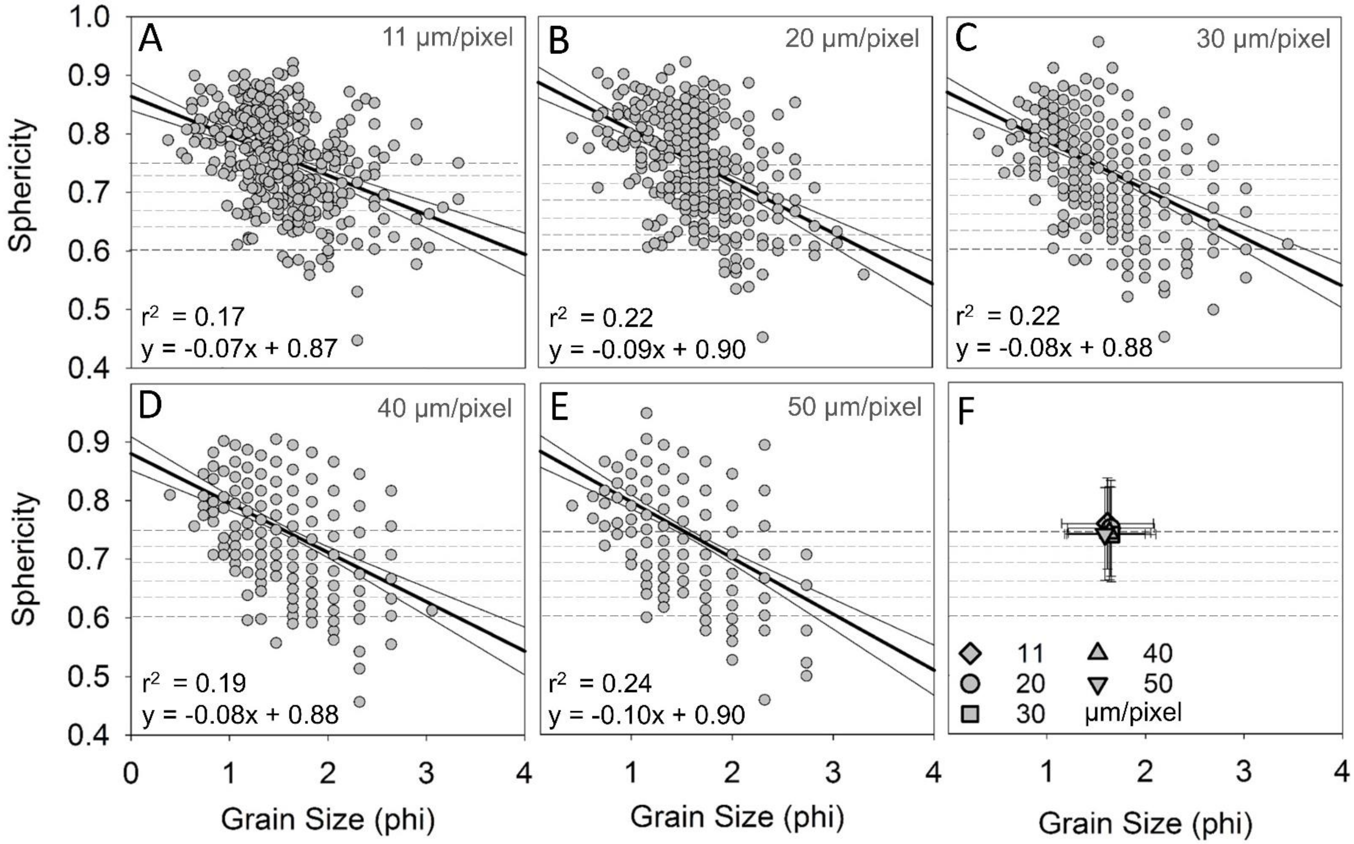

Figure I1: Aeolian sediment relationship between sphericity and grain size determined from images of different resolutions. Linear regressions (bold solid line) and confidence intervals (thin solid lines) are significant at the 95% confidence level. Dashed lines represent divisions between descriptive sphericities. (A) 11 µm/pixel. (B) 20 µm/pixel. (C) 30 µm/pixel. (D) 40 µm/pixel. (E) 50 µm/pixel. (F) Average sphericity and grain size for all image resoluitons analyzed. Bars equal one standard deviation.

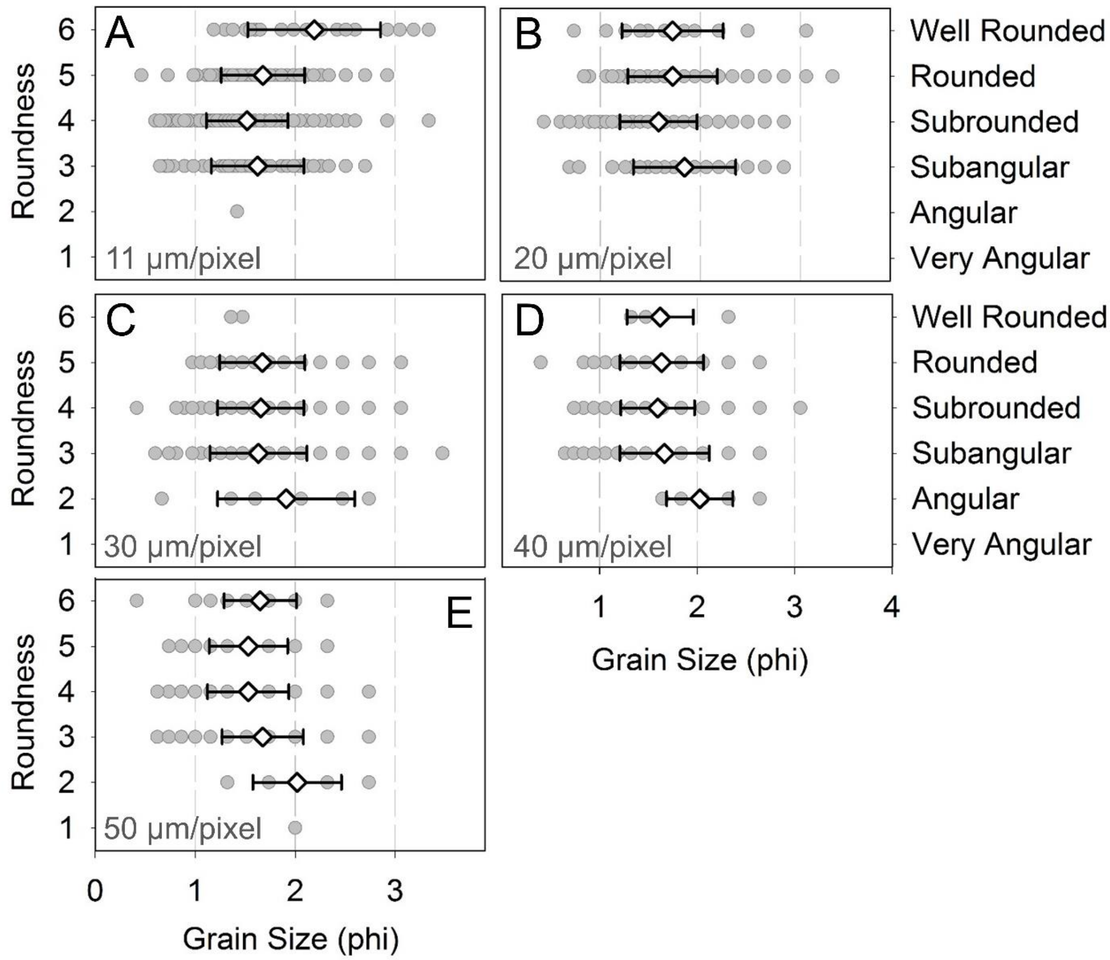

Figure I2: Aeolian sediment relationship between roundness and grain size determined from images at different resolutions. Diamonds represent averages. Bars equalstandard deviation. (A) 11 µm/pixel. (B) 20 µm/pixel. (C) 30 µm/pixel. (D) 40 µm/pixel. (E) 50 µm/pixel.

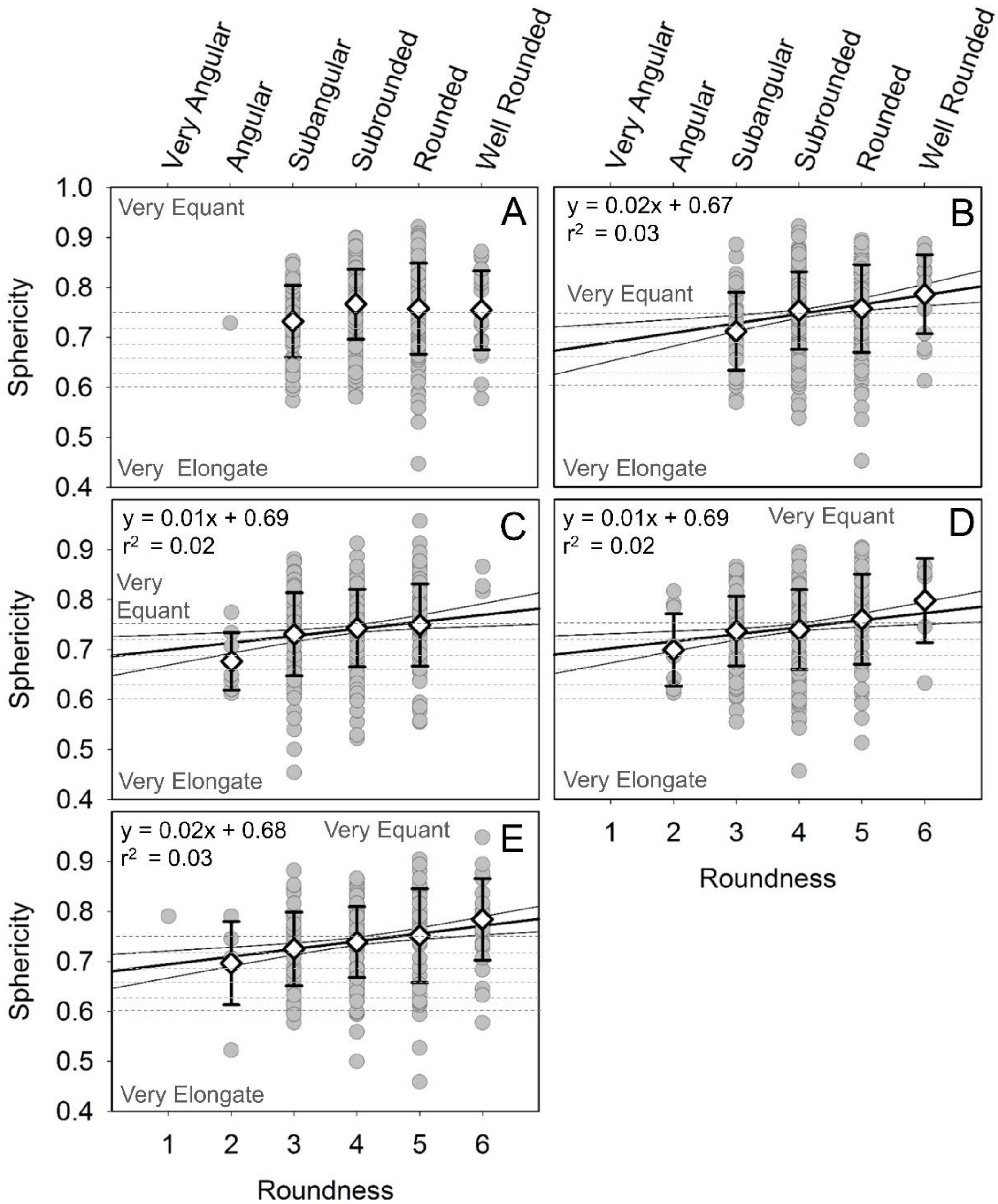

Figure i3: Aeolian seidment relationship between sphericity and roundness determined from images of different resoluiton. Only linear regressions (bold solid line) and confidence intervals (thin solid lines) significant at the 95% confidence level are shown. Dashed lines represent divisions between descriptive sphericities. (A) 11 μm/pixel. (B) 20 μm/pixel. (C) 30 μm/pixel. (D) 40 μm/pixel. (E) 50 μm/pixel.

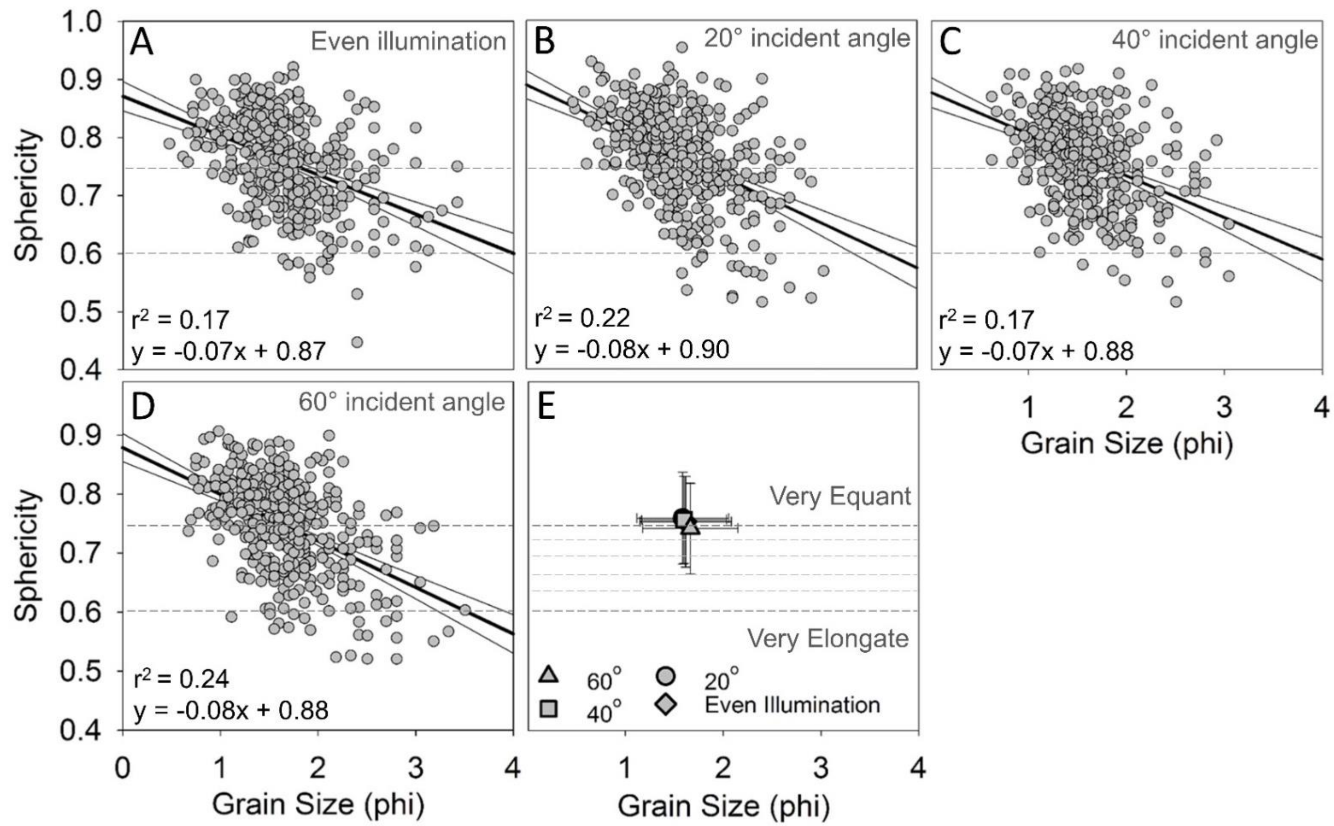

Figure I4: Aeolian sediment relationship between grain size and sphericity determined from images of taken under different illumination conditions. Only linear regressions (bold solid line) and confidence intervals (thin solid lines) significant at the 95% confidence level are shown. Dashed lines represent divisions between descriptive sphericities (A) Even illumination. (B) 20° incident solar angle. (C) 40° incident solar angle. (D) 60° incident solar angle. (F) Average sphericity and grain size. Bars equal one standard deviation.

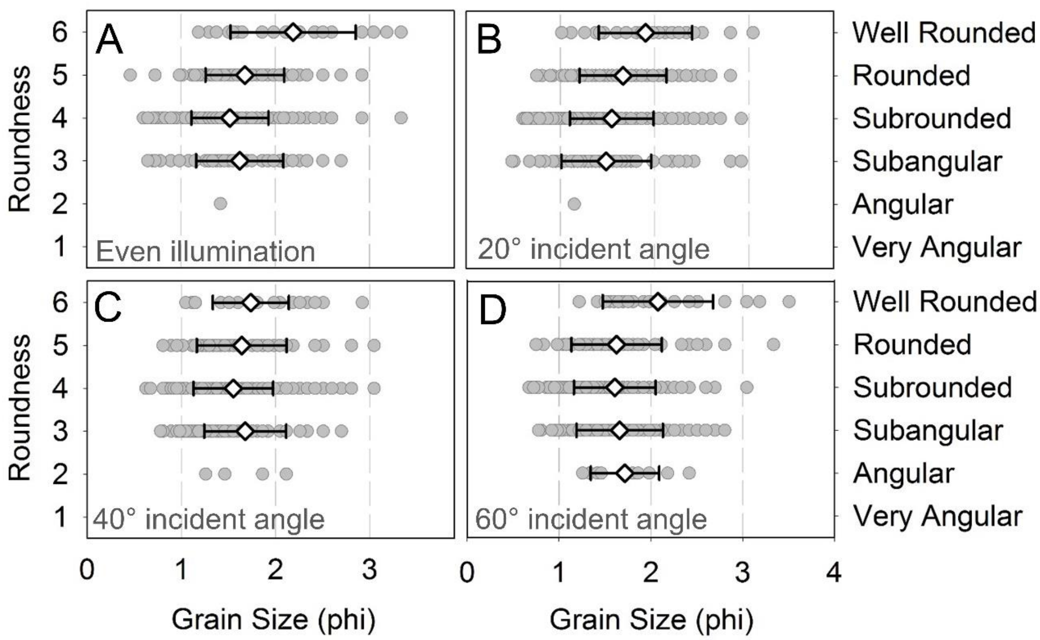

Figure I5: Aeolian sediment relationship between sphericity and grain size for images taken under different illumination conditions. Diamonds represent averages. Bars equal one standard deviation. (A) Even illumination and (B) 20° incident solar angle. (C) 40° incident solar angle. (D) 60° incident solar angle.

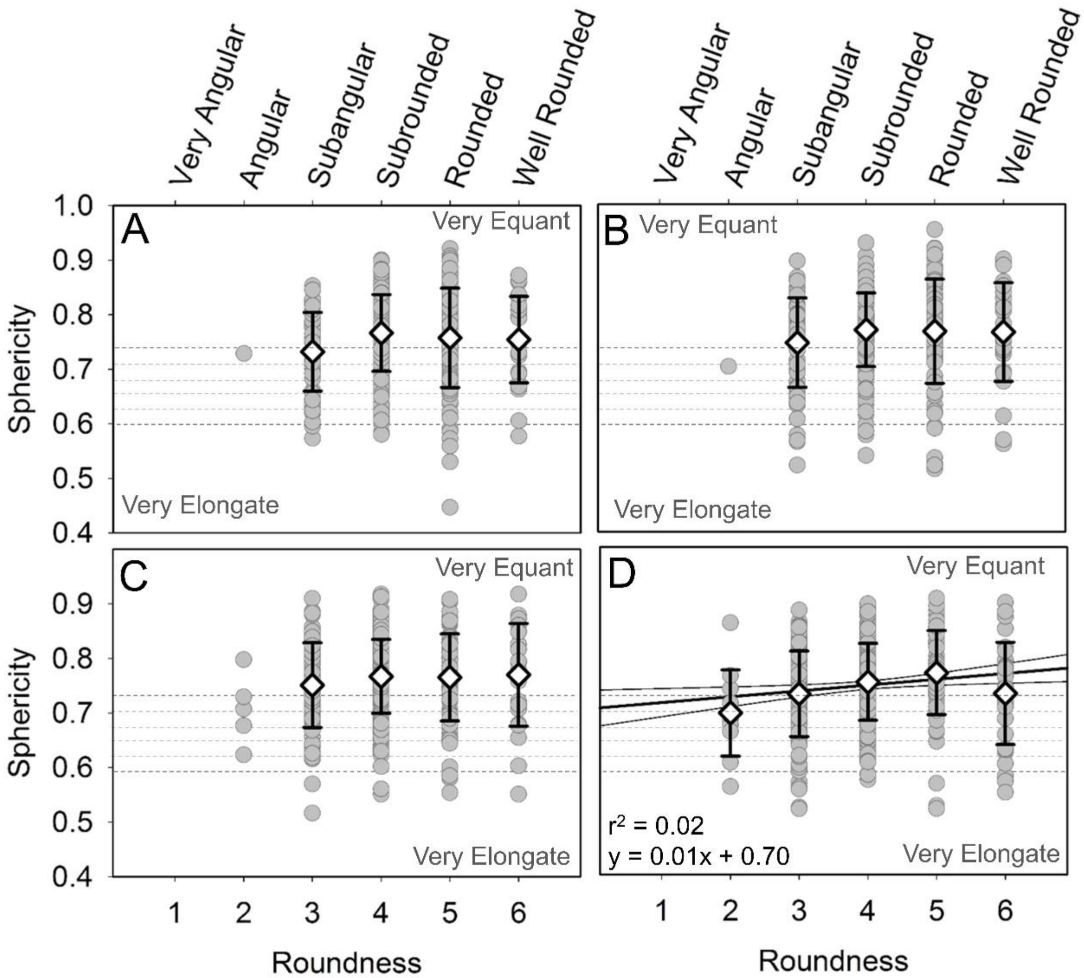

Figure I6: Aeolian sediment relationship between sphericity and roundness for images taken under different illumination conditions. Diamonds represent average sphericity. Bars equal one standard deviation. Only linear regressions (bold solid line) and confidence intervals (thin solid lines) significant at the 95% confidence level are shown. Dashed lines represent divisions between descriptive sphericities (A) Even illumination. (B) 20° incident solar angle. (C) 30° incident solar angle. (D) 60° incident solar angle.

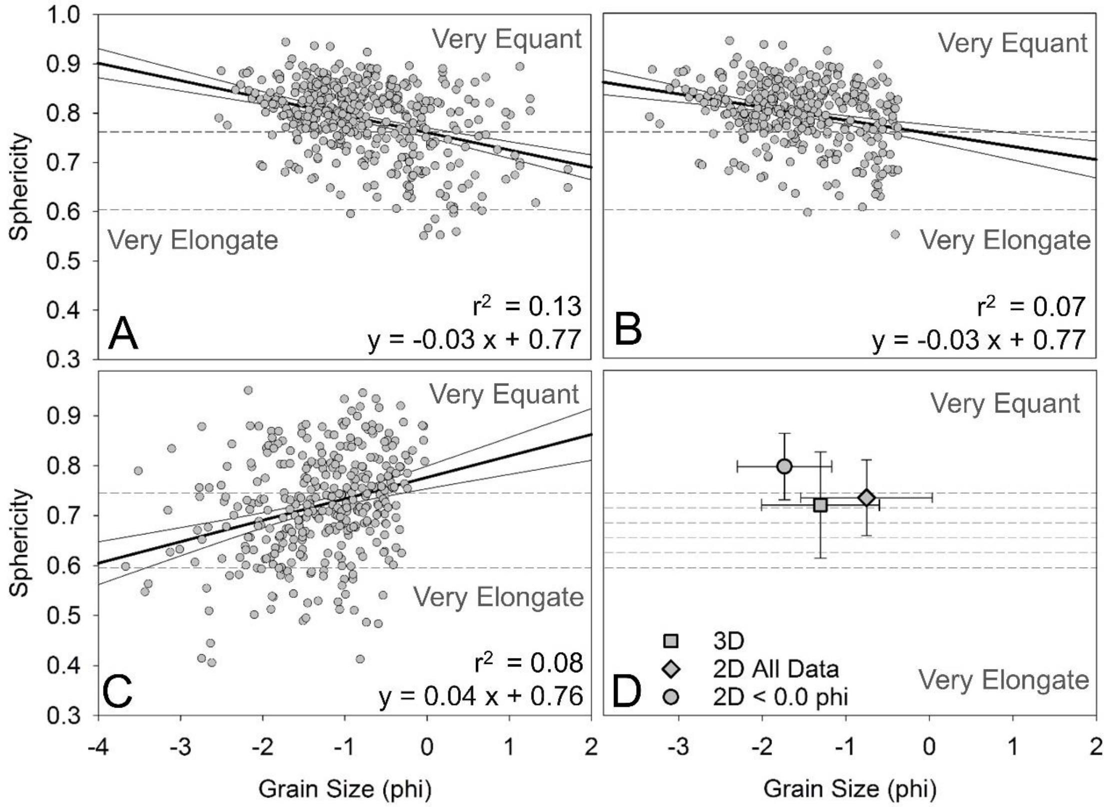

Figure I7: Fluvial sediment relationship between sphericity and grain size for the actual sediment and image analysis at 19 µm/pixel. Only linear regressions (bold solid line) and confidence intervals (thin solid lines) significant at the 95% confidence level are shown. Dashed lines represent divisions between descriptive sphericities (A) Actual fluvial sediment. (B) Imaged fluvial sediment including all grain sizes. (C) Imaged fluvial sediment with grain sizes < 0.0 phi. (D) Average sphericity and grain size. Bars equal one standard deviation.

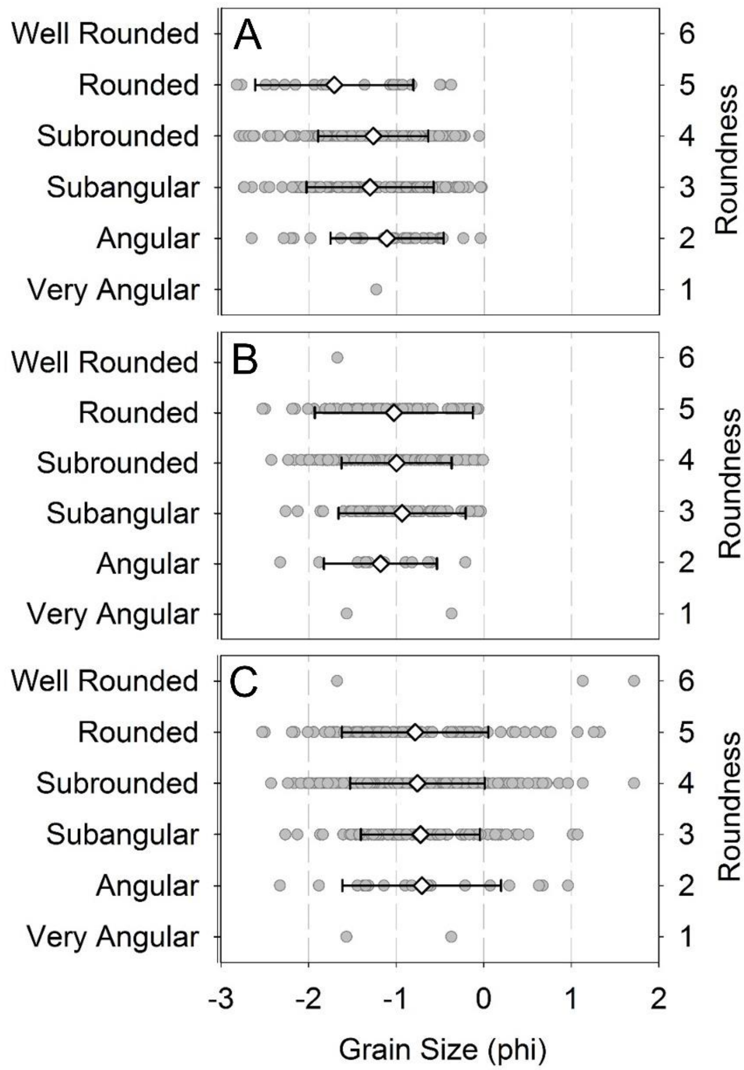

Figure I8: Fluvial sediment relationship between sphericity and grain size for the actual sediment and the 19 μm/pixel image. Diamonds represent averages. Bars equal one standard deviation. (A) Actual sediment. (B) Imaged sediment with grain sizes <0.0 phi. (C) Imaged sediment all grain sizes.

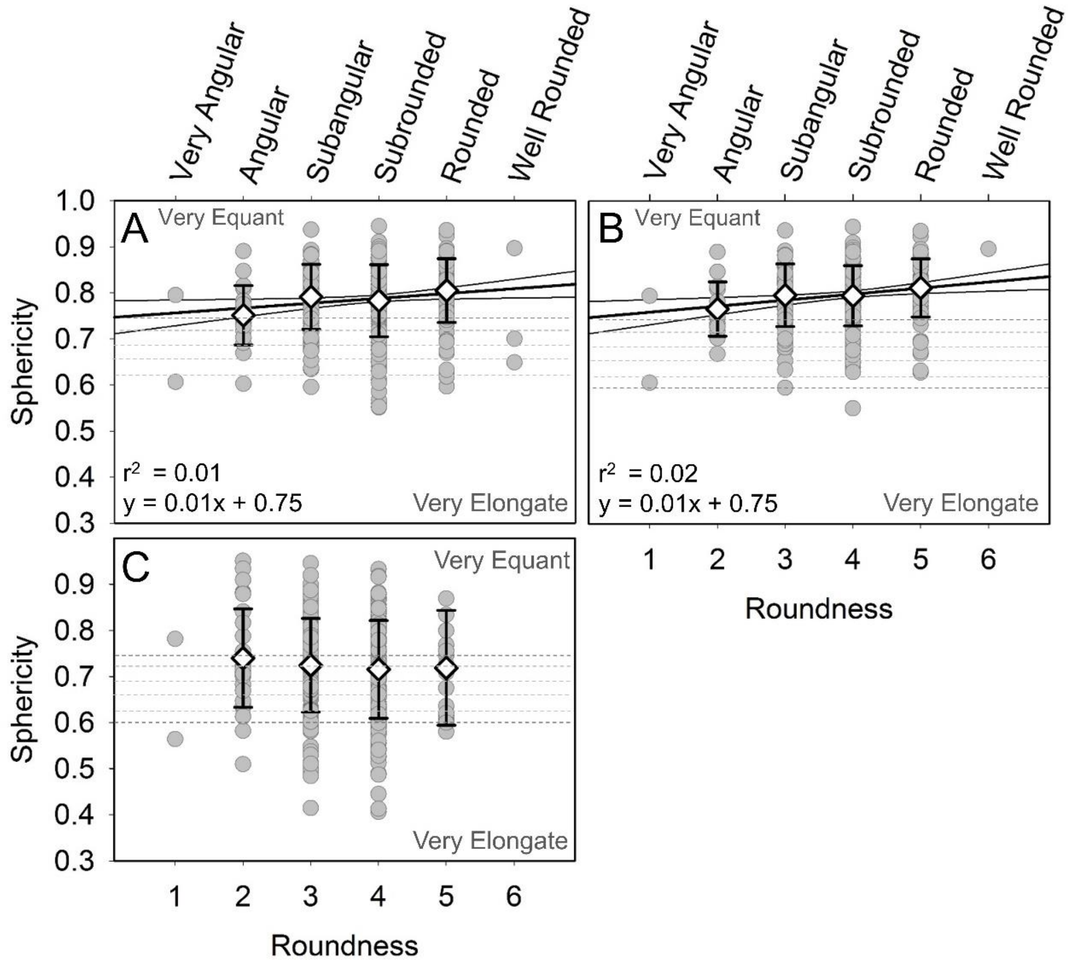

Figure I9: Fluvial sediment relationship between sphericity and roundness determined from the actual and imaged sediment at 19 µm/pixel. Diamonds represent averages. Bars equal one standard deviation. Dashed lines represent divisions between descriptive sphericities (A) Imaged sediment including all grain sizes. (B) Imaged sediment with only grain sizes < 0.0 phi. (C) Actual sediment.

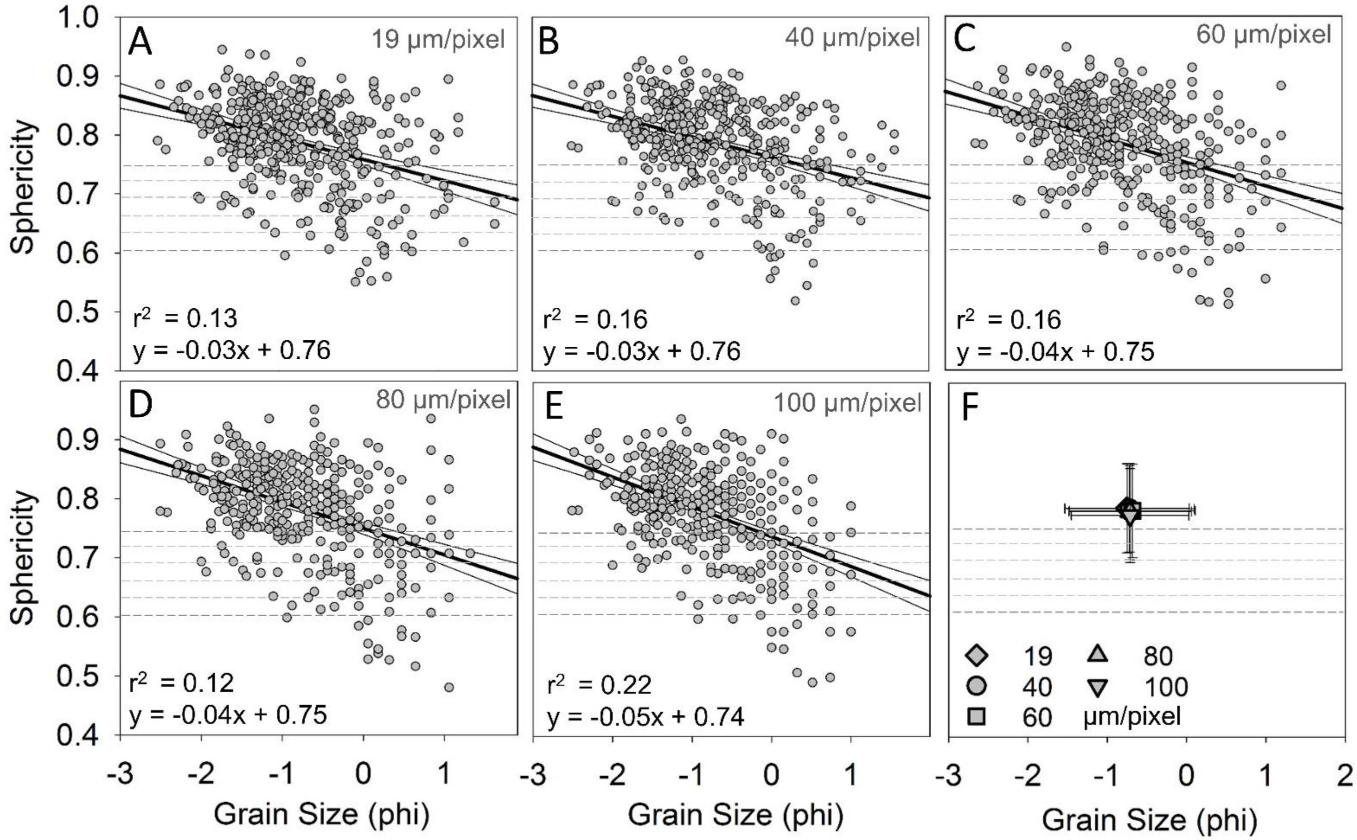

Figure I10: Fluvial sediment relationship between sphericity and grain size determined from images of different reosluitons. Linear regressions (bold solid line) and confidence intervals (thin solid lines) are significant at the 95% confidence level. Dashed lines represent divisions between descriptive sphericities (A) 19 μm/pixel. (B) 40 μm/pixel. (C) 60 μm/pixel. (D) 80 μm/pixel. (E) 100 μm/pixel. (F) Average sphericity and grain size. Bars are one standard deviation.

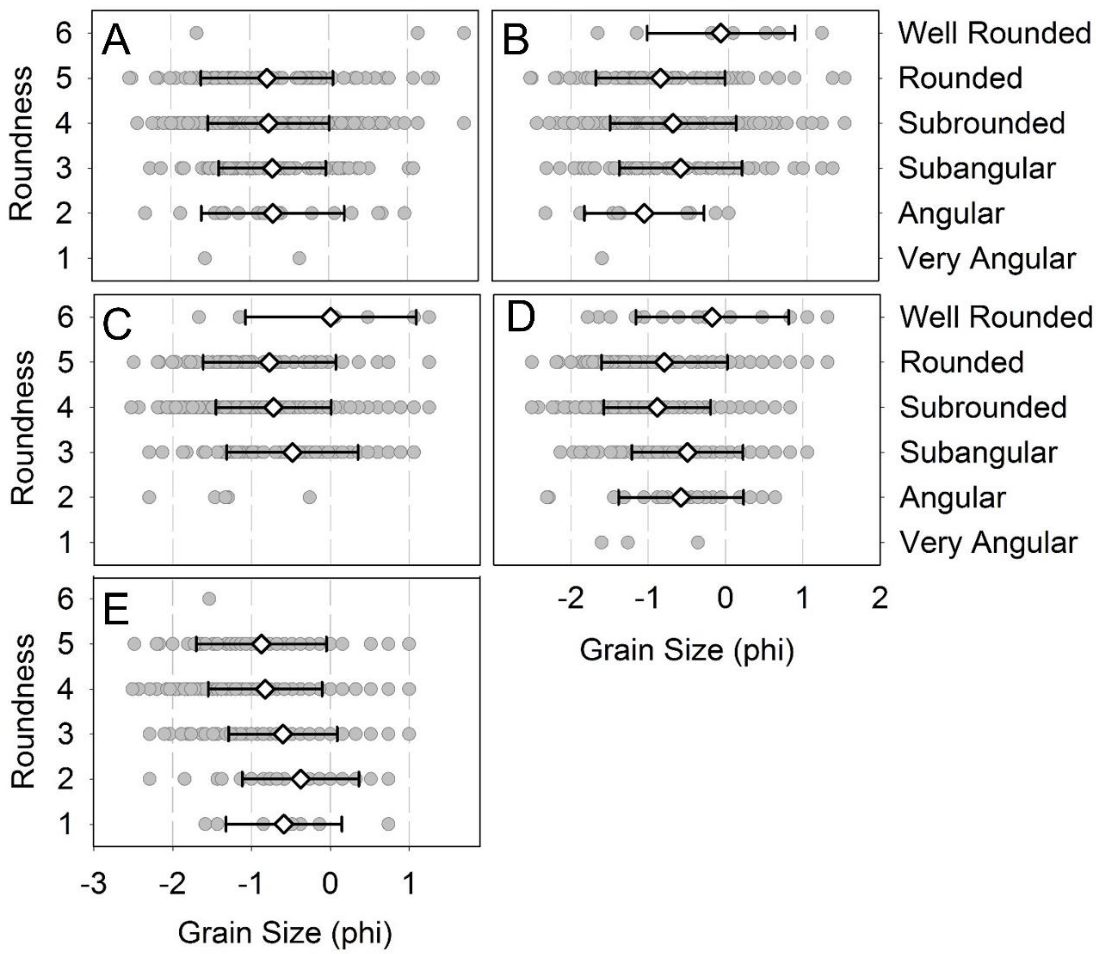

Figure I11: Fluvial sediment relationship between roundness and grain size determined from images at different resolutions. Diamonds are averages. Bars are one standard deviation. (A) 19 μm/pixel. (B) 40 μm/pixel. (C) 60 μm/pixel. (D) 80 μm/pixel. (E) 100 μm/pixel.

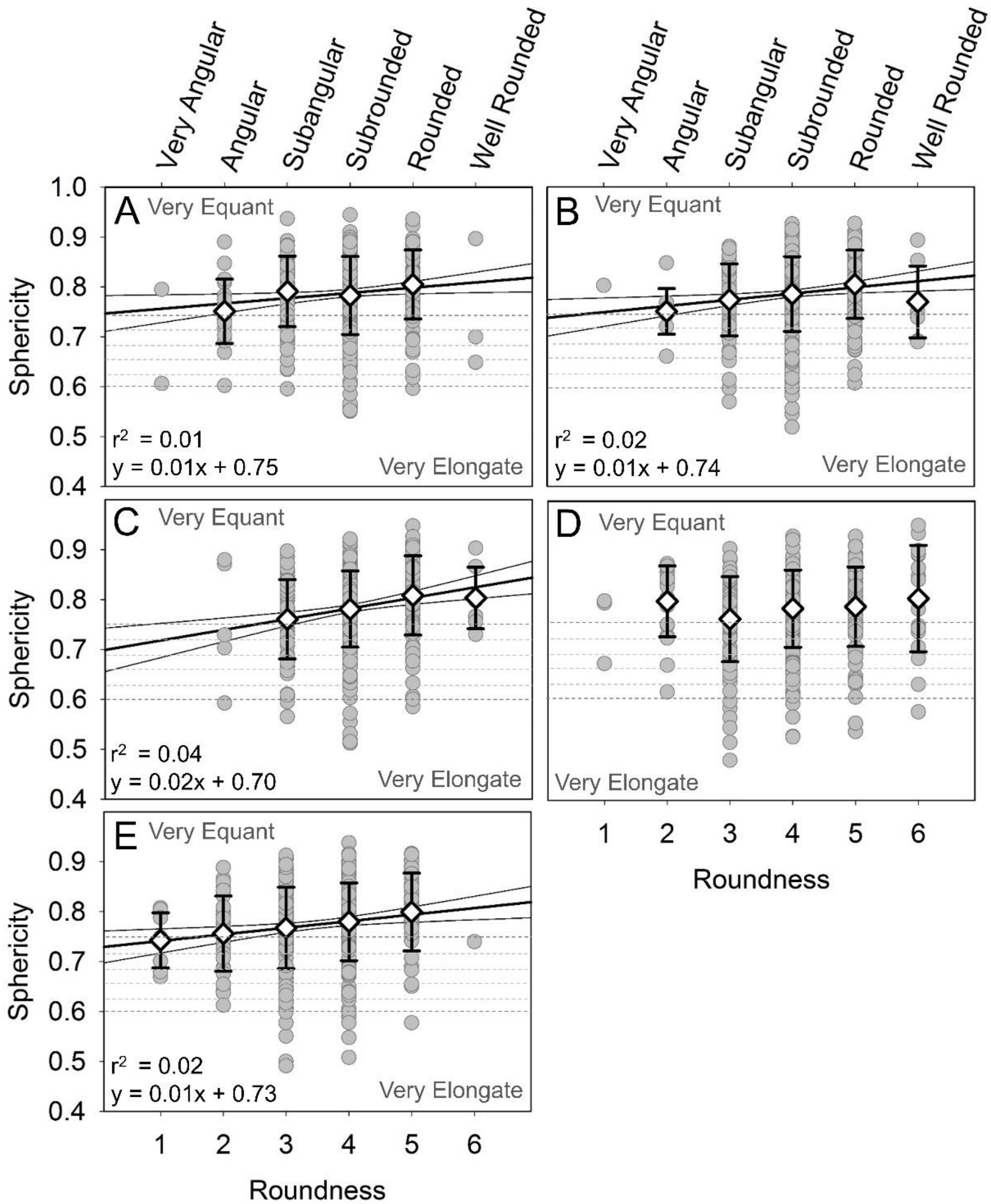

Figure I12: Fluvial sediment relationship between sphericity and roundness determined from images of different resoluitons. Only linear regressions (bold solid line) and confidence intervals (thin solid lines) significant at the 95% confidence level are shown. Dashed lines represent divisions between descriptive sphericities. (A) 19 μm/pixel. (B) 40 μm/pixel. (C) 60 μm/pixel. (D) 80 μm/pixel. (E) 100 μm/pixel**.**

Appendix J

Summary statistics for textural relationships

Table J1: Aeolian sediment summary statistics for sphericity and grain size at each roundness value for images analyzed at 11, 20, 30, 40, and 50 µm/pixel.

Image	Roundness	Sphericity			Grain Size (phi).		
		Average	Description	Standard Deviation	Average	Description	Standard Deviation
11 µm/pixel	Overall	0.759	Very Equant	0.078	1.616	Medium Sand	0.466
	1	-	-	-	-	-	-
	2	-	-	-	-	-	-
	3	0.732	Equant	0.072	1.624	Medium Sand	0.463
	4	0.767	Very Equant	0.07	1.518	Medium Sand	0.408
	5	0.758	Very Equant	0.0911	1.678	Medium Sand	0.418
	6	0.754	Very Equant	0.0792	2.190	Fine Sand	0.665
20 µm/pixel	Overall	0.751	Very Equant	0.082	1.653	Medium Sand	0.441
	1	-	-	-	-	-	-
	2	-	-	-	-	-	-
	3	0.716	Subequant	0.0781	1.842	Medium Sand	0.512
	4	0.753	Very Equant	0.0777	1.581	Medium Sand	0.387
	5	0.757	Very Equant	0.0877	1.723	Medium Sand	0.448
	6	0.786	Very Equant	0.079	1.722	Medium Sand	0.506
30 µm/pixel	Overall	0.740	Equant	0.081	1.653	Medium Sand	0.452
	1	-	-	-	-	-	-
	2	0.677	Intermediate Shape	0.0578	1.910	Medium Sand	0.685
	3	0.731	Equant	0.0832	1.632	Medium Sand	0.484
	4	0.743	Equant	0.0775	1.656	Medium Sand	0.431
	5	0.749	Equant	0.0823	1.671	Medium Sand	0.426
	6	-	-	-	1.435	Medium Sand	0.054
40 µm/pixel	Overall	0.743	Equant	0.080	1.635	Medium Sand	0.417
	1	-	-	-	-	-	-
	2	0.699	Subequant	0.0724	2.027	Fine Sand	0.340
	3	0.737	Equant	0.0697	1.666	Medium Sand	0.458
	4	0.740	Equant	0.08	1.597	Medium Sand	0.378
	5	0.761	Very Equant	0.0902	1.637	Medium Sand	0.427
	6	0.798	Very Equant	0.0839	1.621	Medium Sand	0.340
50 µm/pixel	Overall	0.741	Equant	0.079	1.588	Medium Sand	0.408
	1	-	-	-	-	-	-
	2	0.697	Subequant	0.0836	2.020	Fine Sand	0.442
	3	0.725	Equant	0.0737	1.676	Medium Sand	0.407
	4	0.739	Equant	0.0709	1.530	Medium Sand	0.407
	5	0.752	Very Equant	0.0937	1.531	Medium Sand	0.392
	6	0.784	Very Equant	0.0815	1.650	Medium Sand	0.363

Table J2: Aeolian sediment summary statistics for sphericity and grain size and statistics at each roundness value for images taken under even illumination and 20°, 40°, and 60° incident solar angle.

Image	Roundness	Sphericity			Grain Size		
		Average	Description	Standard Deviation	Average	Description	Standard Deviation
Even Illumination	Overall	0.759	Very Equant	0.078	1.616	Medium Sand	0.466
	1	-	-	-	-	-	-
	2	-	-	-	-	-	-
	3	0.732	Equant	0.072	1.624	Medium Sand	0.463
	4	0.767	Very Equant	0.070	1.519	Medium Sand	0.409
	5	0.758	Very Equant	0.091	1.678	Medium Sand	0.418
	6	0.754	Very Equant	0.079	2.190	Fine Sand	0.665
20° Solar Angle Image	Overall	0.765	Very Equant	0.079	1.586		0.470
	1	-	-	-	-	-	-
	2	-	-	-	-	-	-
	3	0.747	Equant	0.082	1.487	Medium Sand	0.476
	4	0.770	Very Equant	0.068	1.546	Medium Sand	0.445
	5	0.768	Very Equant	0.096	1.666	Medium Sand	0.462
	6	0.766	Very Equant	0.090	1.904	Medium Sand	0.496
40° Solar Angle Image	Overall	0.762	Very Equant	0.075	1.601	Medium Sand	0.435
	1	-	-	-	-	-	-
	2	0.707	Subequant	0.058	1.575	Medium Sand	0.128
	3	0.751	Very Equant	0.078	1.677	Medium Sand	0.435
	4	0.767	Very Equant	0.068	1.551	Medium Sand	0.423
	5	0.765	Very Equant	0.080	1.640	Medium Sand	0.477
	6	0.770	Very Equant	0.094	1.737	Medium Sand	0.404
60° Solar Angle Image	Overall	0.747	Equant	0.078	1.664	Medium Sand	0.487
	1	-	-	-	-	-	-
	2	0.696	Subequant	0.079	1.719	Medium Sand	0.372
	3	0.731	Equant	0.078	1.661	Medium Sand	0.471
	4	0.753	Very Equant	0.071	1.609	Medium Sand	0.445
	5	0.770	Very Equant	0.077	1.628	Medium Sand	0.492
	6	0.732	Equant	0.094	2.078	Medium Sand	0.600

Table J3: Fluvial sediment summary statistics for sphericity and grain size at each roundness value for images analyzed at 19, 40, 60, 80, and 1000 µm/pixel.

Sediment/ Image	Roundness	Sphericity			Grain Size		
		Average	Description	Standard Deviation	Average	Description	Standard Deviation
3D Sediment	Overall	0.721	Equant	0.106	-1.303	V. Fine Pebbles	0.705
	1	-	-	-	-	-	-
	2	0.740	Equant	0.107	-1.111	V. Fine Pebbles	0.646
	3	0.724	Equant	0.102	-1.305	V. Fine Pebbles	0.725
	4	0.715	Subequant	0.106	-1.269	V. Fine Pebbles	0.629
	5	0.719	Subequant	0.125	-1.713	V. Fine Pebbles	0.902
	6	-		-	-	-	-
19 µm/pixel image	Overall	0.735	Equant	0.076	-0.751	V. Coarse Sand	0.786
	1	-	-	-	-	-	-
	2	0.751	Very Equant	0.0458	-0.708	V. Coarse Sand	0.906
	3	0.791	Very Equant	0.0719	-0.723	V. Coarse Sand	0.679
	4	0.783	Very Equant	0.0749	-0.759	V. Coarse Sand	0.766
	5	0.805	Very Equant	0.0683	-0.782	V. Coarse Sand	0.836
	6	-	-	-	-	-	-
19 µm/pixel image (< 0.0 phi)	Overall	0.798	Very Equant	0.066	-1.004	V. Fine Pebbles	0.565
	1	-		-	-	-	-
	2	0.766	Very Equant	0.589	-1.182	V. Fine Pebbles	0.646
	3	0.796	Very Equant	0.068	-0.936	V. Coarse Sand	0.725
	4	0.795	Very Equant	0.654	-0.999	V. Coarse Sand	0.629
	5	0.812	Very Equant	0.632	-1.029	V. Fine Pebbles	0.902
	6	-		-	-	-	-
40 µm/pixel image	Overall	0.786	Very Equant	0.073	-0.717	V. Coarse Sand	0.813
	1	-	-	-	-	-	-
	2	0.751	Very Equant	0.046	-1.069	V. Fine Pebbles	0.759
	3	0.774	Very Equant	0.0794	-0.598	V. Coarse Sand	0.796
	4	0.786	Very Equant	0.0765	-0.701	V. Coarse Sand	0.798
	5	0.805	Very Equant	0.0794	-0.864	V. Coarse Sand	0.819
	6	0.770	Very Equant	0.0617	-0.097	V. Coarse Sand	0.936
60 µm/pixel image	Overall	0.783	Very Equant	0.079	-0.683	V. Coarse Sand	0.792
	1	-	-	-	-	-	-
	2	-	-	-	-	-	-
	3	0.761	Very Equant	0.079	-0.484	V. Coarse Sand	0.833
	4	0.781	Very Equant	0.076	-0.722	V. Coarse Sand	0.730
	5	0.808	Very Equant	0.079	-0.774	V. Coarse Sand	0.842
	6	0.803	Very Equant	0.062	0.004	V. Coarse Sand	1.082
80 µm/pixel image	Overall	0.782	Very Equant	0.082	-0.714	V. Coarse Sand	0.773
	1	-	-	-	-	-	-
	2	0.799	Very Equant	0.071	-0.576	V. Coarse Sand	0.809
	3	0.764	Very Equant	0.085	-0.493	V. Coarse Sand	0.719
	4	0.785	Very Equant	0.078	-0.884	V. Coarse Sand	0.691
	5	0.788	Very Equant	0.080	-0.791	V. Coarse Sand	0.814
	6	0.805	Very Equant	0.107	-0.172	V. Coarse Sand	0.988
100 µm/pixel image	Overall	0.775	Very Equant	0.080	-0.713	V. Coarse Sand	0.740
	1	0.743	Equant	0.0551	-0.590	V. Coarse Sand	0.736
	2	0.756	Very Equant	0.0752	-0.378	V. Coarse Sand	0.740
	3	0.768	Very Equant	0.0817	-0.603	V. Coarse Sand	0.689
	4	0.780	Very Equant	0.0778	-0.827	V. Coarse Sand	0.723
	5	0.799	Very Equant	0.0779	-0.875	V. Coarse Sand	0.826
	6	-	-	-	-	-	-

VITA

Mary Agnes Eibl was born in May of 1990. As a child, her family moved from Delaware to Franklin, Tennessee where she spent her childhood. She graduated from Franklin High School in 2008, and enrolled in college at the University of Tennessee at Chattanooga. Mary received a dual-major B.S. in Geology and Environmental Science in 2012. During her senior year of college she participated in an internship at Oak Ridge National Laboratory where she continued to intern after graduating with her B.S. In, 2014, she enrolled in graduate school at the University of Tennessee, Knoxville. Mary graduated with her M.S. in Geology from the University of Tennessee in August of 2016.